



**HAL**  
open science

## Crowd of Microswimmers

Edouardo Al Alam

► **To cite this version:**

Edouardo Al Alam. Crowd of Microswimmers. Condensed Matter [cond-mat]. Université Grenoble Alpes [2020-..], 2022. English. NNT : 2022GRALY050 . tel-03894880

**HAL Id: tel-03894880**

**<https://theses.hal.science/tel-03894880>**

Submitted on 12 Dec 2022

**HAL** is a multi-disciplinary open access archive for the deposit and dissemination of scientific research documents, whether they are published or not. The documents may come from teaching and research institutions in France or abroad, or from public or private research centers.

L'archive ouverte pluridisciplinaire **HAL**, est destinée au dépôt et à la diffusion de documents scientifiques de niveau recherche, publiés ou non, émanant des établissements d'enseignement et de recherche français ou étrangers, des laboratoires publics ou privés.

THÈSE

Pour obtenir le grade de

**DOCTEUR DE L'UNIVERSITÉ GRENOBLE ALPES**

École doctorale : PHYS - Physique

Spécialité : Physique de la Matière Condensée et du Rayonnement

Unité de recherche : Laboratoire Interdisciplinaire de Physique

**Foule de Micronageurs**

**Crowd of Microswimmers**

Présentée par :

**Edouardo AL ALAM**

Direction de thèse :

**Salima RAFAI**  
Université Grenoble Alpes

Directrice de thèse

**Philippe PEYLA**  
Université Grenoble Alpes

Co-directeur de thèse

Rapporteurs :

**FLORENCE ELIAS**  
Professeur des Universités, UNIVERSITE DE PARIS-CITE  
**XAVIER NOBLIN**  
Chargé de recherche HDR, CNRS DELEGATION COTE D'AZUR

Thèse soutenue publiquement le **14 novembre 2022**, devant le jury composé de :

<b>FLORENCE ELIAS</b> Professeur des Universités, UNIVERSITE DE PARIS-CITE	Rapporteure
<b>XAVIER NOBLIN</b> Chargé de recherche HDR, CNRS DELEGATION COTE D'AZUR	Rapporteur
<b>HUGUES BODIGUEL</b> Professeur des Universités, GRENOBLE INP	Président
<b>BERTRAND MAURY</b> Professeur des Universités, UNIVERSITE PARIS- SACLAY	Examineur





## Acknowledgments

It is in meditating on writing these lines that a person realizes he is far from walking the path of life alone. This journey I embarked on, I wasn't alone, this path I walked, I had company, this project I worked on, I had mentors. It comes as no doubt, that this work, accomplished during what is arguably the most difficult period in recent decade, would not be possible if one is not surrounded by good company.

If one follows customs, one must begin by thanking the members of the jury, given the fact that these people accepted to take time from their busy schedules to participate to long presentation and debate. A thank you to professor Florence Elias and Professor Xavier Noblin for the positive feedback and comments while reading and evaluating my work. It is always a big satisfaction to realize that the result of hard work and dedication is rewarded. Of course I would like also to thank Bertrand Maury for his unique insight on the active matter world, in particular the problem of evacuation that this work tackles. And I can't forget the president of the jury Hugues Bodiguel who was a part of my CSI and witnessed the evolution of the work.

A thank you to my director, Salima Rafai, for her belief in me, even though the path was not smooth, but your remarks and support are the corner stone of this work. Your advice and expertise helped me navigate the academic world and shaped my experience. This experimental work wouldn't be possible without your guidance. I extend my gratefulness to Philippe Peyla, his analytical spirit was an essential part in developing a critical point of view by which I was able to look at my results. The discussions we had played an important aspect in the understanding and the moving forward of the project. It is worth mentioning that this work is financed by the CNRS 80Prime program.

This work would not be possible, and I say this with the highest level of certainty, without the constant support of my *fiancée*, Dandara VELASCO. Thank you for being so patient and bearing with me over these last couple of years while I was trying to figure this out, together we walked through those tribes and tribulations and came out strong. Of course, I cannot forget my family, that despite the long distances separating us, was able to lift me up, especially my father from whom I find inspiration and model of resilience, and my mother, for without her love, warmth and prayers this period would have been much harder. A thank you to my brother,

---

to our bond that grew stronger, to our laughs and philosophical conversations that entertained me. To my uncle Charbel and his wife Claire, who considered me as one of their children. To my aunt Zahia, who helped me navigate the uncharted waters of a foreign country once I arrived to France. These pages are not enough to express the extent of my gratitude to the closest people, for ones back is always covered as long as one has a supportive family.

Of course, one should not forget ones friends, specially those who are formed in midst of hardships. Hence, a special thank you goes to all those who our paths crossed at LIPhy (Laboratoire Interdisciplinaire de Physique). The lunch time we shared and the outside activities we had helped alleviate the burden that a thesis can induce. Although the pandemic did not make social interactions any easier, but we have managed to find ways to keep activities going. A thank you to Carlos and Pamela for the dinners we shared and the discussions we had. I wish you all the best. To Ilya and Oksana, with whom we traveled and get to know well, may all your endeavors are met with huge success. To Nicolas and Heloïsa, the time we shared was brief but meaningful, until we meet again whether in Brazil or Europe, may all your dreams come true.

To Ludovic Keiser, we shared office for a brief amount of time (roughly a year) but it was during one of the most critical years of the thesis. Our discussions about science and politics were of great insight, your perseverance gives me motivation. I wish you all the good in the world my friend, and a long and happy life surrounded by your family.

I must admit that it is indeed a very difficult task to remember every person that I crossed that contributed directly or indirectly to the accomplishment of the following work. Therefore, I address a general gratitude to those unknown soldiers.

I have nothing more to add except to wish anyone who, while reading the manuscript from beginning to end, decides that it is indeed an interesting work, and equally anyone who does not and disagrees with me, anyone who's curiosity pushes him to read the work in its integrity, and equally anyone for whom skimming was enough, a truly sincere "Live well"!

---

Quelle est la valeur de la recherche scientifique? Chacun sait que de nos jours, plus que jamais, tout homme ou toute femme qui désire apporter une contribution originale à l'avancement de la science doit se spécialiser: c'est-à-dire intensifier son propre effort en vue d'apprendre tout ce que l'on connaît dans un certain domaine étroit et ensuite essayer d'augmenter l'ensemble de ces connaissances par son propre travail, par des études, des expériences et de la réflexion.

... En troisième lieu, je tiens pour extrêmement douteux que le bonheur de la race humaine ait été augmenté par les développements techniques et industriels qui ont suivi l'éveil et le progrès rapide des sciences de la nature. Je ne puis ici entrer dans des détails et je ne veux pas parler du développement futur : l'infection de la surface terrestre par la radioactivité artificielle, avec les conséquences terrifiantes que cela entraînerait pour notre race, telles qu'Aldous Huxley les dépeint dans son roman récent, à la fois si intéressant et si horrible (*Ape and Essence*). Mais considérez seulement la « merveilleuse réduction de grandeur » du monde rendue possible par les fantastiques moyens modernes de transport. Toutes les distances ont été réduites à presque rien, lorsqu'on les mesure non plus en milles, mais en heures du moyen de transport le plus rapide : Mais lorsqu'on les mesure par le coût du moyen de transport même le moins coûteux, elles ont doublé ou même triplé au cours des dix ou vingt dernières années. Le résultat est que beaucoup de familles et de groupes d'amis intimes ont été dispersés à la surface du globe comme jamais encore cela ne s'était produit dans le passé. Dans bien des cas ceux qui sont ainsi éloignés les uns des autres ne sont pas assez riches pour pouvoir se retrouver, dans d'autres cas ils ne peuvent le faire que moyennant de terribles sacrifices et ce n'est que pour un intervalle de temps très court, qui se termine dans des adieux déchirants. Cela contribue-t-il au bonheur de l'homme ? Il ne s'agit là que d'exemples frappants ; on pourrait faire des développements sur ce thème pendant des heures.

Mais tournons-nous vers des aspects moins obscurs de l'activité humaine. Vous pourriez me demander — vous êtes obligés de me demander maintenant : quelle est donc, selon vous, la valeur des sciences de la nature ? Je réponds : leur objet, leur but et leur valeur sont les mêmes que ceux de n'importe quelle autre branche du savoir humain. Bien plus, il faut dire qu'aucune d'elles, prise seule, n'a d'objet ou de valeur ; seule l'union de toutes les sciences a un but et une valeur. Et on peut en donner une description très simple : c'est d'obéir au commandement de la divinité de Delphes, connais-toi toi-même. Ou, pour l'exprimer dans le discours bref et impressionnant de Plotin (*Ennéades*. VI, 4, 14) : « Peut-être étions-nous déjà là avant que cette création ne vînt à l'existence, êtres humains d'un autre type, ou même quelques espèces de dieux, âmes et esprits purs unis avec la totalité de l'univers, parties du monde intelligible, non séparées et retranchées mais unies au tout. »

Erwin Schrödinger - *Physique quantique et  
représentation du monde* - 1935.

---

---

# Contents

<b>1</b>	<b>Introduction</b>	<b>1</b>
1.1	Crowds from physics point of view . . . . .	2
1.2	The Evacuation Paradox . . . . .	2
1.2.1	In Numerical Analysis . . . . .	3
1.2.2	In Experiments . . . . .	9
1.2.3	Effect of opening angle . . . . .	17
1.3	Micro-swimmers . . . . .	21
1.4	Outline . . . . .	23
<b>2</b>	<b>Materials &amp; Methods</b>	<b>25</b>
2.1	Standard Micro-fabrication . . . . .	26
2.2	Microscopy & Acquisition . . . . .	28
2.3	Particle Tracking Velocimetry (PTV) . . . . .	28
2.4	Density Measurements & Calibration . . . . .	29
2.5	<i>Chlamydomonas Reinhardtii</i> . . . . .	32
2.5.1	Cell Culture . . . . .	33
2.5.2	Response to Light . . . . .	34
2.5.3	Effect of viscosity on swimming velocity . . . . .	36
2.6	A typical Experiment . . . . .	39
<b>3</b>	<b>Statistical Tools to analyse Crowds of Microswimmers</b>	<b>43</b>
3.1	Velocity Calculation . . . . .	44
3.2	Crowd Formation . . . . .	45
3.3	Evacuation Statistics from the Waiting time perspective . . . . .	46
3.3.1	Cumulative Number of Escapees . . . . .	47
3.3.2	Time-lapse $\Delta t$ . . . . .	49
3.3.3	Dependent probabilities due to CR-CR interactions. . . . .	50
3.3.4	Survival function . . . . .	51
3.3.5	The Clauset-Shalizi-Newman fitting Method . . . . .	51
3.4	Evacuation Statistics from the Avalanche Size perspective . . . . .	53
3.4.1	Avalanche size . . . . .	54
3.4.2	Jamming time . . . . .	54



---

<b>4</b>	<b>Jamming transition, the <math>D</math>-<math>V</math> phase diagram</b>	<b>57</b>
4.1	Reference Case $D = 67 \mu\text{m}$	58
4.1.1	Cumulative Number of Escapees	58
4.1.2	Stokes Time rescaling	59
4.1.3	Survival Function	61
4.2	Extreme Case $D = 10 \mu\text{m}$	62
4.2.1	Cumulative Number of Escapees	62
4.2.2	Survival Function	63
4.2.3	Coefficient $\alpha$	65
4.3	$D$ - $V$ phase diagram	66
4.3.1	Avalanche size & Critical Diameter $D_c$	66
4.3.2	Active Jamming probability	68
4.3.3	Location of Active Jamming transition	69
4.4	Discussion and Conclusion	70
<b>5</b>	<b>Effect of Geometry, an attempt to unravel the Jamming phenomenology</b>	<b>73</b>
5.1	Experimental set-up: varying the opening angle.	74
5.2	The exponential regime: $D = 75 \mu\text{m}$	76
5.3	The reference case: $D = 40 \mu\text{m}$	77
5.3.1	Cumulative number of escapees	77
5.3.2	Survival Function	77
5.4	The extreme case: $D = 10 \mu\text{m}$	79
5.4.1	Cumulative number of escapees	79
5.4.2	Survival Function	80
5.5	Evolution of $\alpha$ for all $D$ and $\theta$ values	82
5.6	Avalanche size & Critical diameter $D_c$	83
5.7	Jamming probability	84
5.8	$D - \theta$ phase diagram	85
5.9	Discussion	87
	<b>Conclusion</b>	<b>89</b>
	<b>Annexes</b>	<b>94</b>
A	Introduction	96
B	Matériels et Méthodes	97
B.1	Micro-fabrication Standard	97
B.2	Suivi des particules	97
B.3	Calculs de densité et Calibration	97
B.4	<i>Chlamydomonas Reinhardtii</i> Cultures et Propriétés	98
B.5	Une expérience typique	98
C	Outils statistiques pour l'analyse des foules de micro-nageurs	98
C.1	Temps d'attente	98
D	Transition de blocage, le diagramme $D - V$	99
E	Transition de blocage, le diagramme $D - \theta$	99
F	Additional data for Chapter 4	101
G	Additional data for Chapter 5	102
H	Article & Supplementary materials	102

---



---

---

*N'a de conviction que celui qui n'a rien approfondi.*

Emil Cioran - *De l'inconvénient d'être né* - 1973

## Contents

---

<b>1.1</b>	<b>Crowds from physics point of view . . . . .</b>	<b>2</b>
<b>1.2</b>	<b>The Evacuation Paradox . . . . .</b>	<b>2</b>
1.2.1	In Numerical Analysis . . . . .	3
1.2.2	In Experiments . . . . .	9
1.2.3	Effect of opening angle . . . . .	17
<b>1.3</b>	<b>Micro-swimmers . . . . .</b>	<b>21</b>
<b>1.4</b>	<b>Outline . . . . .</b>	<b>23</b>

---

This manuscript is an experimental work focusing on studying systems of active suspension (microswimmers) in a situation of evacuation. The work reported so far in the community focuses on systems where interactions are governed by short range forces (*i.e* friction forces). It appears that a "universal" behavior exists among those systems, best described in the "faster is slower" paradox (FiS). The FiS states that the faster a crowd attempts to evacuate, the slower the evacuation. In this work we test the persistence of this paradox and the nature of "universality" of crowds by exploring the evacuation behavior of active suspensions where hydrodynamic forces come into play. The behavior of these systems during an evacuation remains largely forgotten by the community.

Prior to diving in the approach by which we provide the answer to our question, it is rather important to dissect our subject into two different parts. The first treats the definition of *crowds* (Section 1.1), their paradox and the numerical as well as the experimental work done so far (Section 1.2). The second part consists in a brief introduction to micro-swimmers, their types and their properties. (Section 1.3)

## 1.1 Crowds from physics point of view

The Oxford English dictionary defines *crowd* as *a large number of people gathered together*. *Crowds* exist in all forms, at all scales in nature; from flocks of birds to school of fishes to colonies of ants. Therefore, it comes as no surprise to us that physicists turn their attention toward this category and do what they do best, that is observe, understand, and try to replicate. As a result a new domain of research has emerged at the end of the twentieth century entitled *Active Matter* (Prost and Bruinsma, 2007a,b). Active matter is defined as a collective of particles able to propel themselves in a fluid by injecting energy into their environment, an energy that comes from their biological or chemical mechanisms (Ramaswamy, 2010). One can conclude that active matter is part of a branch of physics that studies out-of-equilibrium systems. The goal of active matter research is to understand the phenomenology behind some behaviors that emerge from collective motion. One phenomenon that has been studied extensively in collective motion, is the emergence of an ordered state from what appears to be an erratic motion. This subject was first tackled by Vicsek et al. (1995) via looking at the collective flying of birds' flocks and considering the individual orientation of one bird is the average orientation of all neighboring birds, Figures 1.1a & 1.1b. This work was later adopted by Chaté et al. (2008) and Grégoire & Chaté (2004). A more recent work, Chardac (2021) showed in her thesis the emergence of such order in artificial rollers. The work done so far, whether be it numerical or experimental, has proven the existence of phase transition from chaotic to ordered state dictated by an increase in density or by a decrease in noise added to orientations. One can see by now that collective motion exhibits some similarities on all scales and through all types of systems. The goal of this work is to tackle another form of crowd's motion that has its own paradox, transcending the boundaries of active matters, and its own universality. This paradox is just starting to grasp the attention of physicists. We narrow our study to a crowd in a situation of evacuation through an opening.

## 1.2 The Evacuation Paradox

There exists a special type of collective motion, that of evacuation, when a cluster of particles try to escape via an opening. In recent years, physicists and sociologists have focused on observing collective motion in human crowds, particularly, the evacuation scenario, given the high risk it poses. Many accidents have been reported throughout the years with catastrophic consequences. Dickie (1995) analyzed in his work major accidents related to crowd for a duration of 15 years and found that they can happen at any event and at any time. Poor architectural planning that fails to take into consideration panic evacuation, unexpected events that forces a crowd to rush erratically toward an exit, or an overall bad organization, all played a role in catastrophic endings. Hence the necessity for a mechanism to better understand the physics behind crowd's evacuation.

However, in addition to a lack of basic understanding, physicists are directly faced with an ethical problem, it is hazardous to put humans in dangerous situations and ask them to evacuate as it can lead to very unwanted situations. To

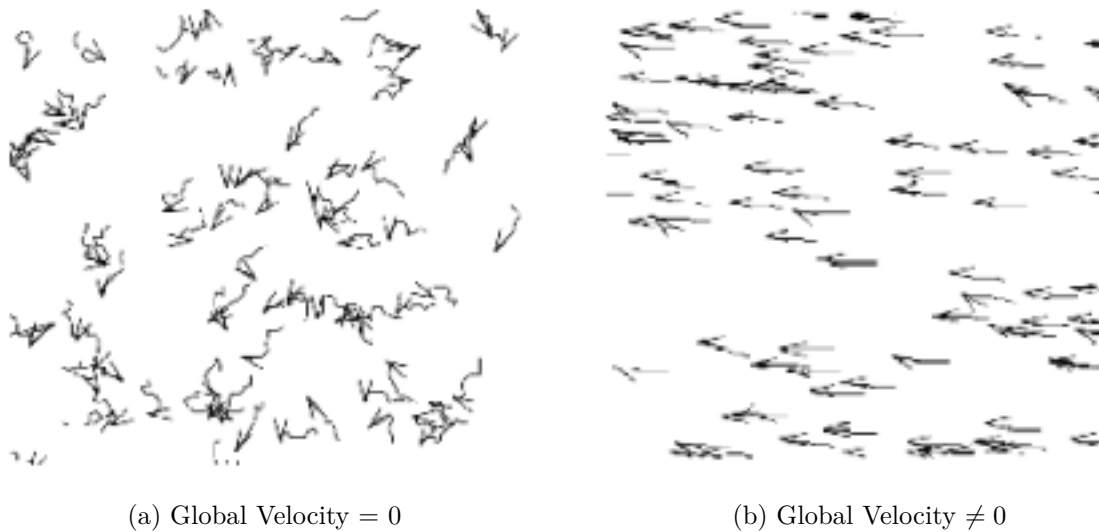


Figure 1.1: Illustration of the model of Vicsek (Vicsek et al., 1995). The orientation is represented by an arrow, and the curve represents the trajectory taken by the last 20 steps. The individual velocity is considered to be constant, and the active particle adopts the average orientation of the neighboring particles, with a certain noise  $\xi$ . a. Is a scenario where the global velocity is null. b. Is a case where the global velocity is different from zero. In general the global velocity of active matter is measured in function of the noise. Going under a certain critical value, the velocity varies following  $(\xi_c - \xi)^{0.45}$ .

surpass this obstacle, two approaches are taken. In this section we will present the most important work done in both approaches and how they contribute to a better understanding of crowds in an evacuation situation. Prior to diving into the vast universe of research, we must clarify some important nomenclature. Evacuation is quantifiable by looking at the time-lapse or waiting time between two consecutive exits and by plotting their complementary cumulative distribution function (or CCDF or survival function). Chapter 3 will include more detailed explanation.

### 1.2.1 In Numerical Analysis

The first tool that physicists have is modeling and computing power. It allows them to simulate scenarios where crowds exit in panic without living human subjects (Lin et al., 2016). This system benefits from an analogy with gas theory (Helbing, 2010) and fluids (Henderson, 1974), by considering humans as particles interacting with each others. It is following this assumption that a first model was built (Helbing & Molnar, 1995) and obeys the basics of molecular dynamics. In what is know as the "Social Force Model" (SFM for short) Figure 1.2a, human motion is caused by the desire of people to reach a certain destination, hence three kind of forces are used to model this behavior: 'desire force', the 'social force' and the 'granular force'. The 'desire force', as its name suggests, represents the pedestrian's desire to reach

a specific position at a desired velocity. We can write this force as:

$$\mathbf{f}_d^{(i)} = m_i \frac{v_d^{(i)} \mathbf{e}_d^{(i)}(t) - \mathbf{v}^{(i)}}{\tau} \quad (1.1)$$

where  $m_i$  is the mass of the pedestrian  $i$  and  $\tau$  is a constant related to the relaxation time needed for the pedestrian reaches his/her destination.  $v^{(i)}$  is the pedestrian velocity, while  $v_d^{(i)}$  is the desired velocity.  $\mathbf{e}_d^{(i)}$  is the direction of motion of the pedestrian (unity vector). The 'social force' is the tendency of two pedestrians  $i$  and  $j$  to stay away from each other and can be written as:

$$\mathbf{f}_s^{(ij)} = A_i e^{r_{ij} - d_{ij}/B_i} \mathbf{n}_{ij} \quad (1.2)$$

where  $(ij)$  is any pedestrian pair or pedestrian-wall pair.  $A_i$  and  $B_i$  are fixed values and  $d_{ij}$  is the distance between the center of mass of pedestrians  $i$  and  $j$ .  $r_{ij} = r_i + r_j$  is the sum of the pedestrians radius.  $\mathbf{n}_{ij}$  is the unit vector from  $j$  to  $i$ . The third force or 'granular force' comes into play when two pedestrians come into contact with each other and is written as:

$$\mathbf{f}_g^{(ij)} = \kappa(r_{ij} - d_{ij}) \Theta(r_{ij} - d_{ij}) \Delta \mathbf{v}^{(ij)} \mathbf{t}_{ij} \quad (1.3)$$

Where  $\kappa$  is a fixed parameter.  $\Theta(r_{ij} - d_{ij})$  is null when  $r_{ij} < d_{ij}$  and equal to 1 for all other cases.  $\Delta \mathbf{v}^{(ij)} \mathbf{t}_{ij}$  is the difference between the individual and the walls (*i.e* the tangential velocities of the sliding bodies).

Having defined the forces that act on a pedestrian in a crowd, the equation of motion can be easily defined.

$$m_i \frac{d\mathbf{v}^{(i)}}{dt} = \mathbf{f}_d^{(i)} + \sum_{j=1}^N \mathbf{f}_s^{(ij)} + \sum_{j=1}^N \mathbf{f}_g^{(ij)} \quad (1.4)$$

Interestingly enough, a particular behavior emerges from these simulations described as 'Faster is Slower' or 'The crowd's paradox'. Basically, the blocking time of an exit increases as the 'desired velocity' is increased, meaning the faster the pedestrians desire to exit, the more time the process will take. In Section 1.2.2 we will see this paradox in details in experiments. Still in numerical analysis, [Sticco et al. \(2017\)](#) have taken the SFM and extended it to larger values of desired velocities. In their work they have reported what is known as 'Beyond the faster is slower effect', where beyond a certain limit value of  $v_d$  the blocking time starts to decrease and the evacuation becomes faster, hence the description of a 'faster is faster' behavior [Figure 1.2b](#). Another more recent approach at model humans in an evacuation situation is to consider them as game players and use a model based on the mean-field game theory. This is done by [Bonnemain et al. \(2022\)](#), and it proves to be remarkably successful in capturing the experimental observations associated with crowds entering the metro [Figure 1.3a](#), where a heat map generated by numerical analysis shows a concentration of density at the entrance of the wagon's door, reminiscent to what

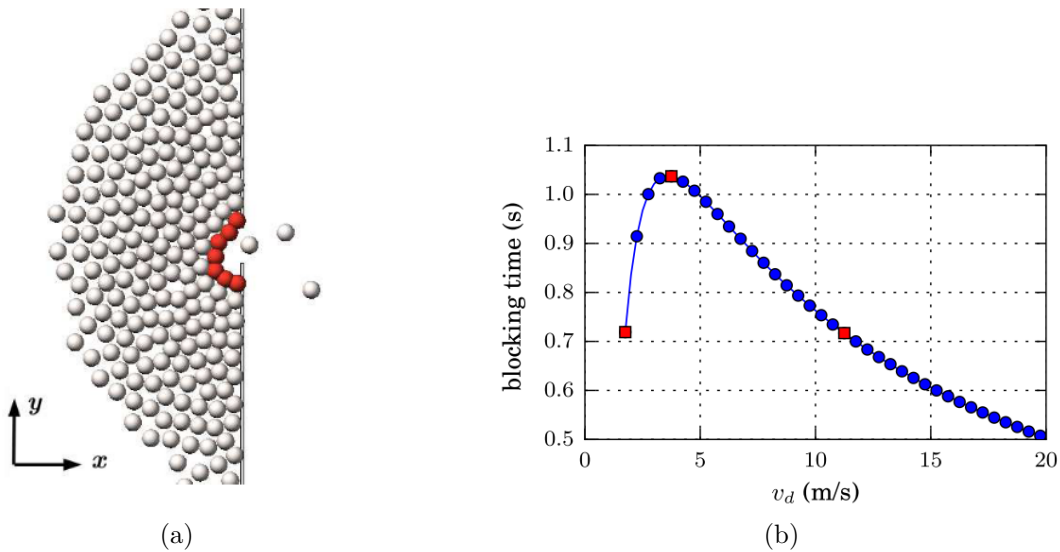


Figure 1.2: a. Numerical analysis results following the Social Force model developed by (Helbing & Molnar, 1995) showing the presence of an arch at the exit causing the clogging. b. The evolution of the blocking time with the desired velocity as done by Sticco et al. (2017). Blocking time increases with increasing velocity describing a faster is slower effect. After reaching reaching a critical velocity, the clogging time starts to decrease describing a faster is faster regime. This is mainly due to an increase in kinetic energy that leads to a breaking of the arch.

is seen in real life Figure 1.3b. A work reminiscent of Heliövaara et al. (2013). This suggests that clogging may be caused by people acting rationally, even when this rational individual behavior results in a bad strategy for the group. Faure & Maury (2015) have tackled the problem from a different angle. They considered individuals as hard disks Figure 1.4b, interacting via friction forces while trying to move and reach their desired velocity while avoiding interactions with their neighbors. Results from numerical simulations show that the probability of blocking the door decreases with increasing door's width Figure 1.4a. A similar observation to the effects seen in granular model.

Physicists extend their study of crowd's evacuation, not just to human or living organisms but also to inert granular systems. For instance, Zuriguel et al. (2014) used the Lattice-Boltzmann method to model the motion of a colloid suspension passing through a constriction Figure 1.5a. They looked at the complementary distribution function of waiting times and found it to be of a power law tail shape with an exponent  $\alpha$ . A survival function is defined as  $P(t > \Delta t) = |\int_{\Delta t}^{\infty} \rho(t) dt|$ , where  $\rho(t)$  is the distribution of the waiting times. Details regarding the CCDF are given in Chapter 3 and Chapter 4. The clogging transition can be achieved naturally by changing the temperature, which controls the interplay between colloidal particle fluctuations and the intensity of the driving force. Low temperatures lead to clogged states and high temperatures to unclogged states. The parameter  $\alpha$  is also used to described the state of the system. Small values of  $\alpha$  represent a system that is prone to clogging Figure 1.5b. In the same study, authors used the SFM model Figure 1.5c and looked at the waiting time distribution for different pedestrian's desired



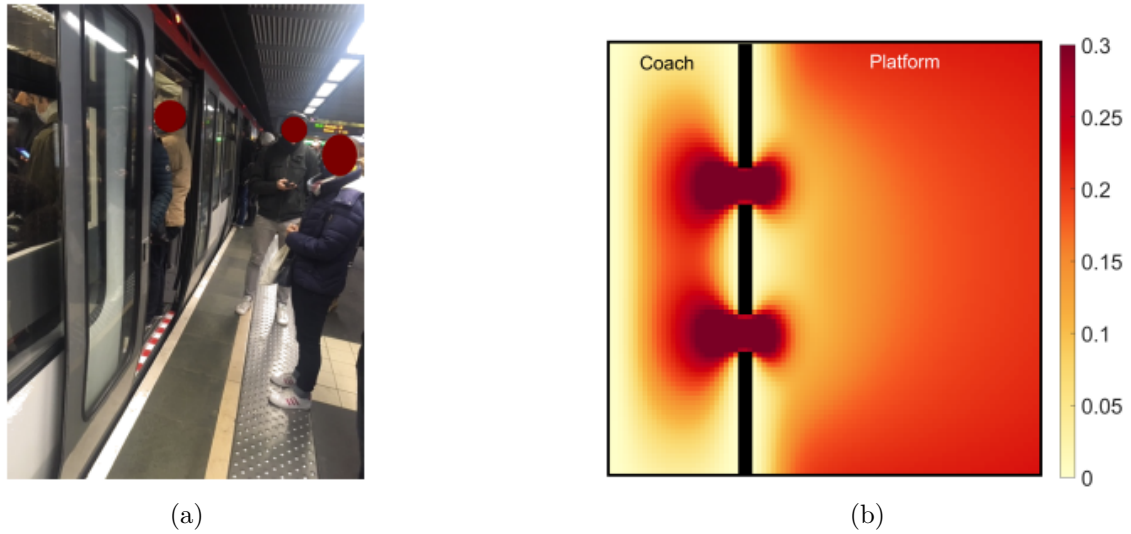


Figure 1.3: a. Passenger waiting on the platform to board the metro in a metro station in Lyon, France. b. Heat map resulting from the game theory showing similarities with the real world, where passengers tend to form crowds at the entrance of the coach. Density follows the scale-bar color. (Bonnemain et al., 2022)

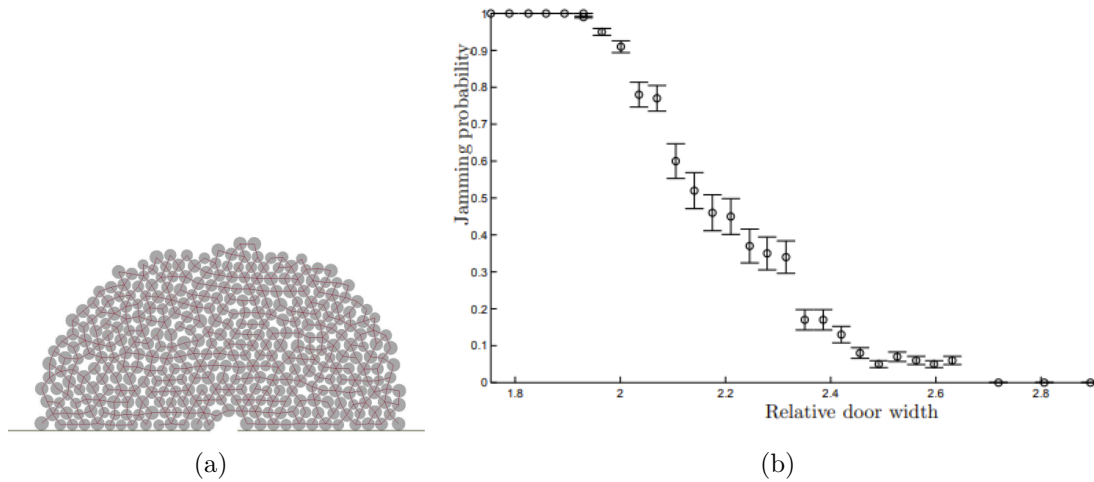


Figure 1.4: a. Results from numerical analysis considering individuals as disks with friction force applied on them while trying to reach a certain desired velocity shows once again the arch formation that leads to clogging. b. The jamming probability as function of relative door width: the bigger the door the less is the probability of it getting jammed. (Faure & Maury, 2015)

velocities as well as a variety of door width. A 'faster is slower' behavior is reported with the survival function following, a power law tail Figure 1.5d with the parameter  $\alpha$  increasing with decreasing desired velocity, this means that the slower the crowd moves toward the door the faster they exit (the probability of finding long waiting times is low). The physical reason behind this clustering and blocking of the exit is believed to be caused by arch formation on the exit. Finding ways to break the arch formation leads to a smoother evacuation. Vibrations are one way to destroy

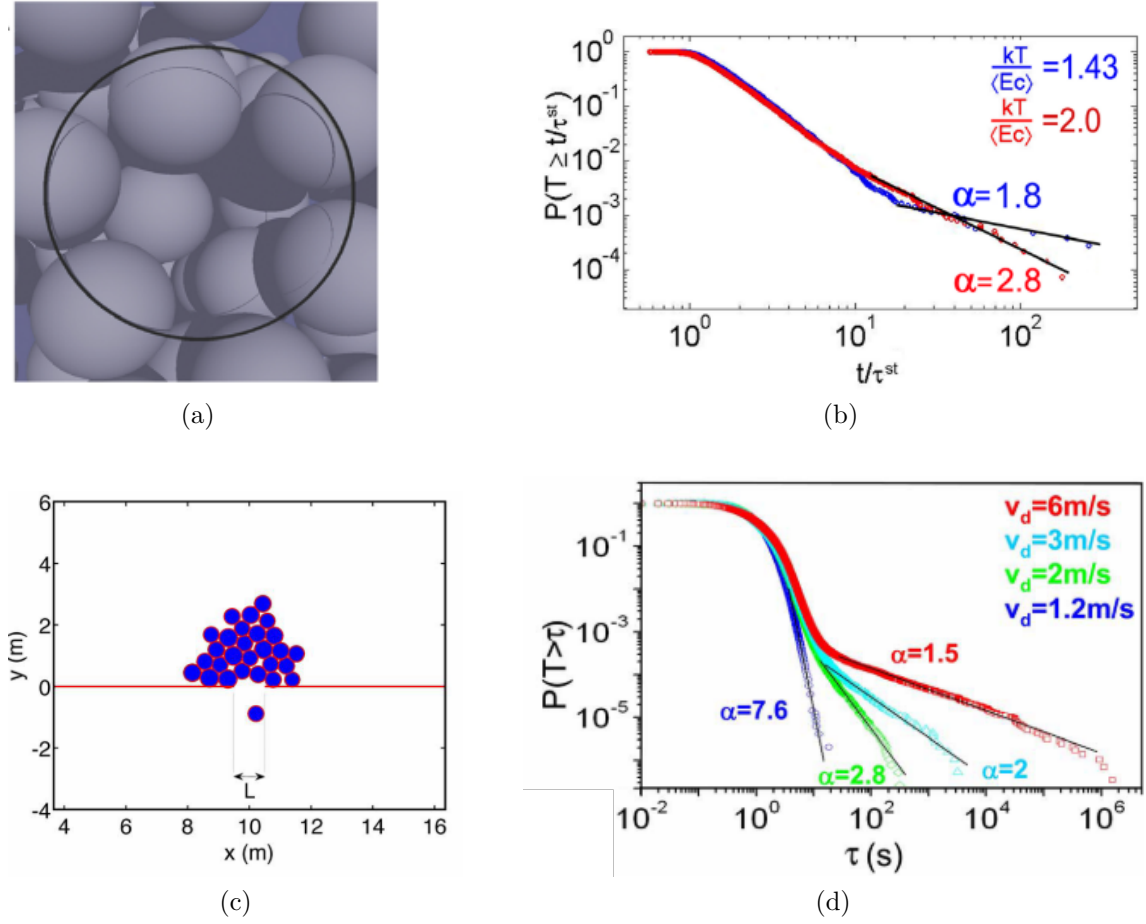


Figure 1.5: a. Numerical analysis results done via the lattice Boltzmann technique of colloidal suspension driven by a pressure gradient through a constriction. b. Survival function of the time lapse distribution for different temperatures. Blue line represents states of low temperature where the system is more prone to clogging. Whereas the red line represents state of high temperature where the system is less prone to clogging. With the exponent  $\alpha_{cold} < \alpha_{hot}$ . Time-lapses are normalized by the Stokes time  $\tau^{st}$  proportional to the size of the sphere over the velocity. c. Sketch of simulation of pedestrians evacuating a room using the Social Force Model plus a random force applied uniformly in the y-direction. d. Complementary cumulative distribution function for different driving velocity shows the trend of power law tail where the exponent is higher for lower velocity and decreases with increasing  $v_d$ , describing a faster is slower effect. Here,  $\tau$  represents the waiting time. (Zuriguel et al., 2014) (Details regarding the CCDF are given in Chapter 3 and Chapter 4)

these clogs. Nicolas et al. (2018) proposed a simple model for arch breaking, where vibrations are equivalent to thermal fluctuations in a Langevin equation and the escape from an energy trap corresponds to the rupture of an arch Figure 1.6a. Their results show similarity with experimental observations and their model is able to capture the heavy tail in the survival function usually observed for clogged states Figure 1.6b. Arch breaking can also be facilitated or exaggerated depending on the particle deformability. In a recent study, Bielinski et al. (2021) used the lattice-

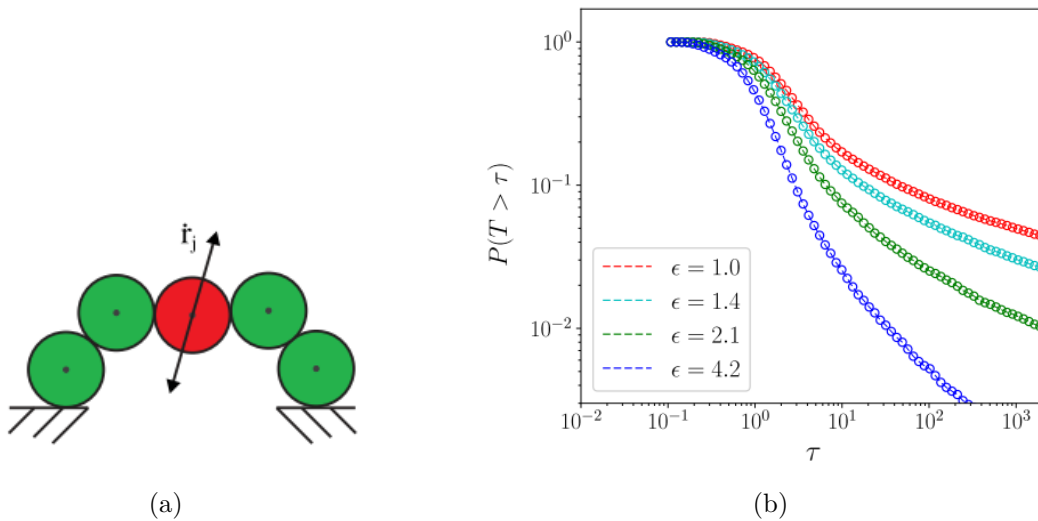


Figure 1.6: a. Sketch of an arch of vibrated grains. b. Survival function for different vibration's temperature  $\epsilon$  showing the effect of increasing vibration on the enhancement of the evacuation process.(Nicolas et al., 2018)

Boltzmann method to investigate numerically how multiple deformable capsules squeeze into a constriction Figure 1.7b. They reported that the transition from clogged to unclogged state is dictated by the ratio between the size of the capsule and the door width and by the particle deformability. These observations allowed them to build a phase diagram Figure 1.7a showing that a high deformable particle can easily *squeeze* its way out of a constriction whereas the opposite causes the system to clog.

Numerical analysis tools have allowed physicists to study the effect of many parameters on the efficiency of the evacuation. We have seen, in general, that both, physiological (*i.e* velocity, pressure...) and geometrical (*i.e* opening size) constraints plays a role in dictating the state of the system. A faster attempt at exiting induces a slower overall evacuation, whereas an increase in door size leads to a more fluid evacuation.

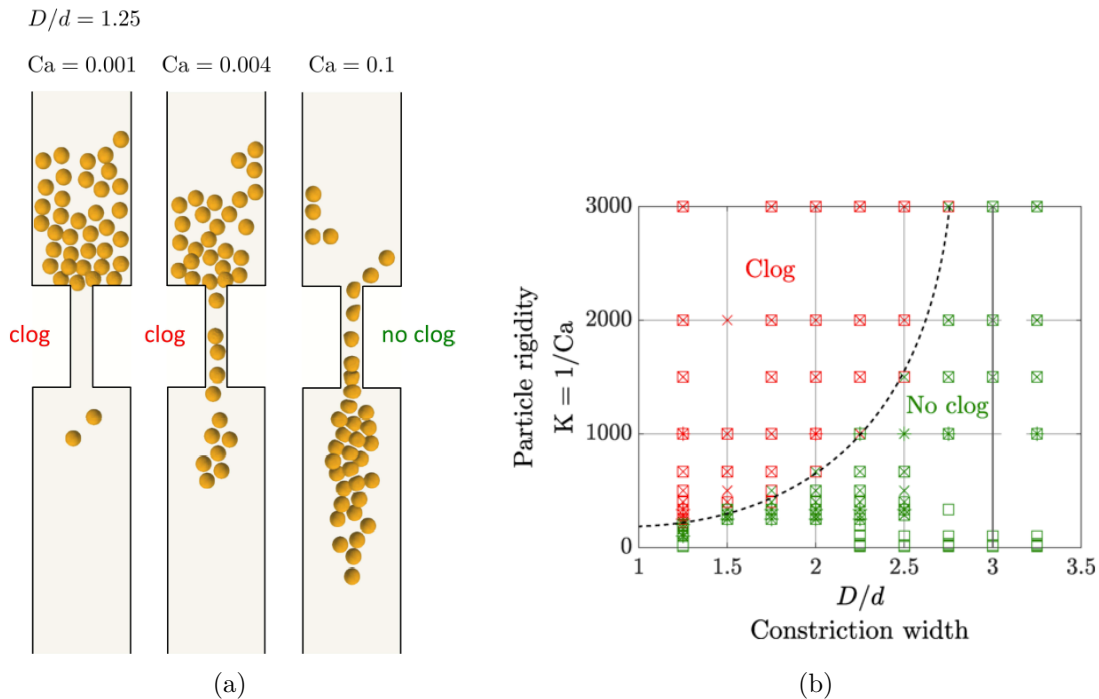


Figure 1.7: a. Sketch of particles evacuating for a fixed door width to particle diameter ratio of  $D/d = 1.25$  and different values of particle deformability quantified by the capillary number  $Ca = \frac{\rho v r \dot{\gamma}}{\kappa_s}$ . It shows that the system is not subject to clogging when the deformability is high enough. b. Phase diagram showing the correlation between door width and particle rigidity in determining the state of the system. (Bielinski et al., 2021)

## 1.2.2 In Experiments

Numerical analyses have shown us a pattern that is repeated whenever a crowd is formed on the exit during an evacuation for a wide range of systems. In addition, the evacuation process is highly influenced by physical and geometrical parameters. We have mentioned earlier that experimenting with humans is deemed unethical. However, physicists have found a way to execute such experiments in a highly safe environment. For instance [Garcimartín et al. \(2017\)](#) (Figure 1.8a) performed experiments on pedestrians evacuating through a door and managed to vary the level of competitiveness during the evacuation. They reported that the higher the competitiveness, the harder it is to evacuate. In the same manner, [Nicolas et al. \(2017\)](#) (Figure 1.8b) conducted the evacuation experiment with pedestrians. However they instructed some individuals to be selfish while others remain polite. They reported a strikingly similar behavior described previously, with the selfish way of evacuation resulting in a longer evacuation time.

Interestingly, a similar study was performed using animals, in particular the passage of sheep through a bottleneck as done in the work of [Garcimartín et al. \(2015\)](#). Authors looked at the entrance of sheep into a barn for feeding time and registered the waiting times between each evacuation (or in this case, between each passage through the door). They were interested in the effect of an obstacle placed in front of the door. They studied the statistical distributions of the waiting times and

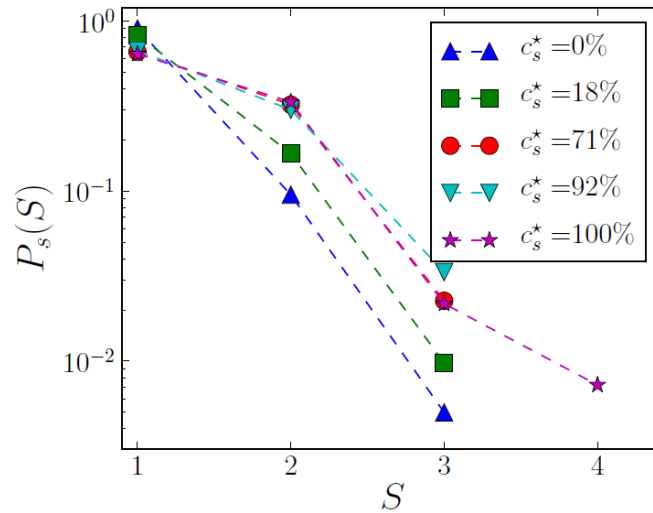
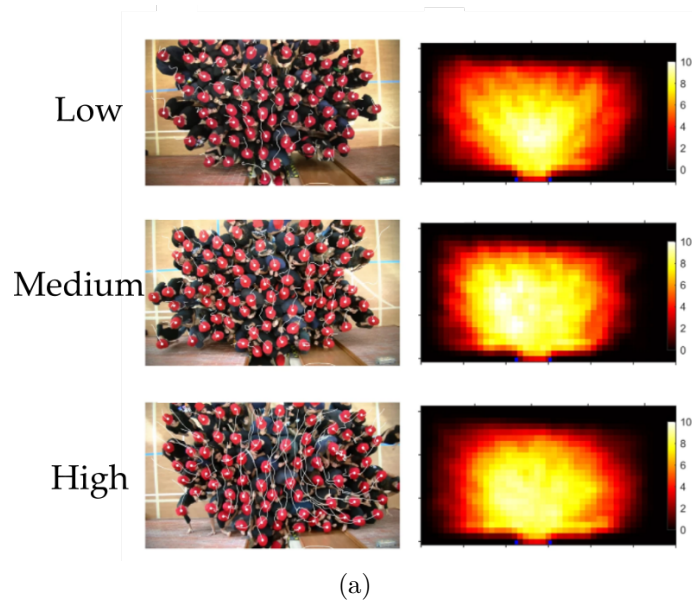


Figure 1.8: a. Snapshot of experiments where a group of pedestrians was asked to evacuate the room with three different degrees of competitiveness, with the corresponding heat maps determining the density. The higher the competitiveness the bigger the crowd at the exit. The color scale at the left indicates the local density in  $person/m^2$  (Garcimartín et al., 2017). b. Complementary cumulative distribution function of waiting times for pedestrians’ evacuation at different percentage of selfishness. When all the pedestrians all selfish,  $c_s^* = 100\%$ , the probability of finding long waiting times increases, meaning a more selfish behavior leads to an interrupted evacuation and is not desired in case of emergency (Nicolas et al., 2017).

found a survival function that decays in a power law. Furthermore, they observed an enhancement in passage with the presence of an obstacle. This similarity can be seen in the work of Pastor et al. (2015), where the authors compared the efficiency of the evacuation for different levels of competitiveness in humans and in herds

of sheep. Competitiveness in sheep is found to increase with increasing ambient temperature. Figure 1.9a shows two different experimental scenarios, on the left a low competitiveness level, with a spatio-temporal diagram showing no gap between people evacuating, and on the right a high competitiveness case with a spatio-temporal diagram showing gaps or *waiting times* between evacuations. A CCDF plot shows a more difficult evacuation at higher competitiveness (red). In the same manner the results of sheep are depicted in Figure 1.9b. Their results are evidence of the striking resemblance to the crowd evacuation across species.

However, even though 'faster is slower' behavior is observed in most living organisms such as sheep and humans, some species escape the trend. For example, when ants run towards an exit via chemo-taxis (a behavior induced by using chemicals), Parisi et al. (2015) found that ants tend to sacrifice themselves for the survival of the colony, hence they avoid any clustering around the exit. A heat map comparing ants experiments and pedestrian numerical analysis, highlights the difference in response Figure 1.10.

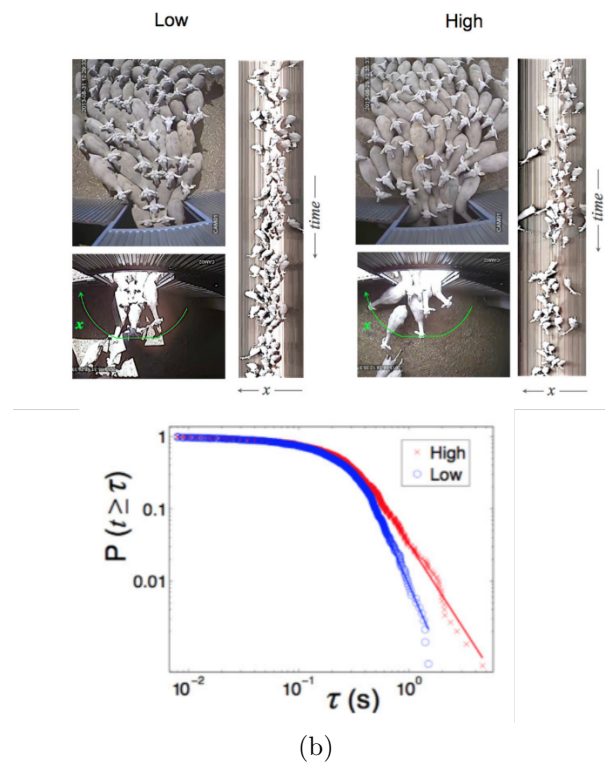
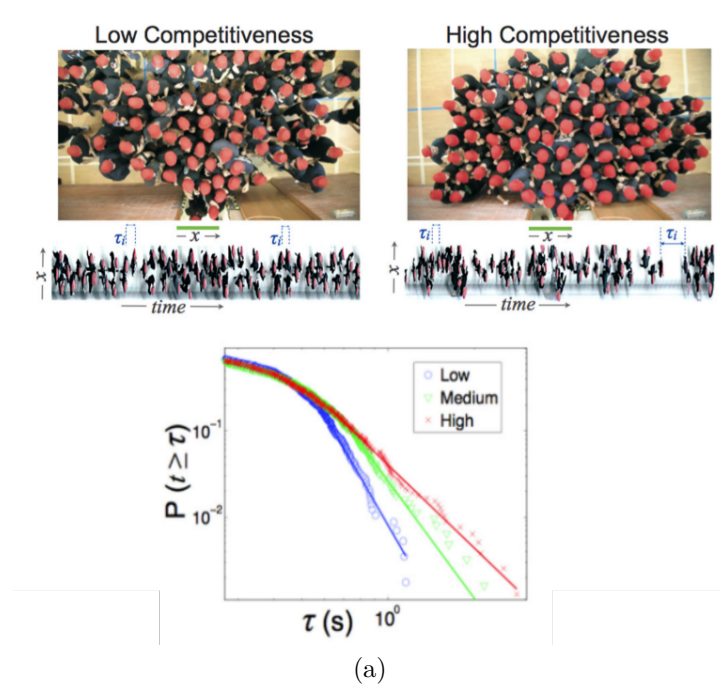


Figure 1.9: CCDF of waiting times  $\tau$  for two different species: a. Pedestrians evacuating at different competitiveness level (low, medium and high), the survival function presents a power law tail where we have a higher probability of finding longer waiting times for higher levels of competitiveness. b. A similar behavior is observed in herd of sheep entering a barn. (Pastor et al., 2015)

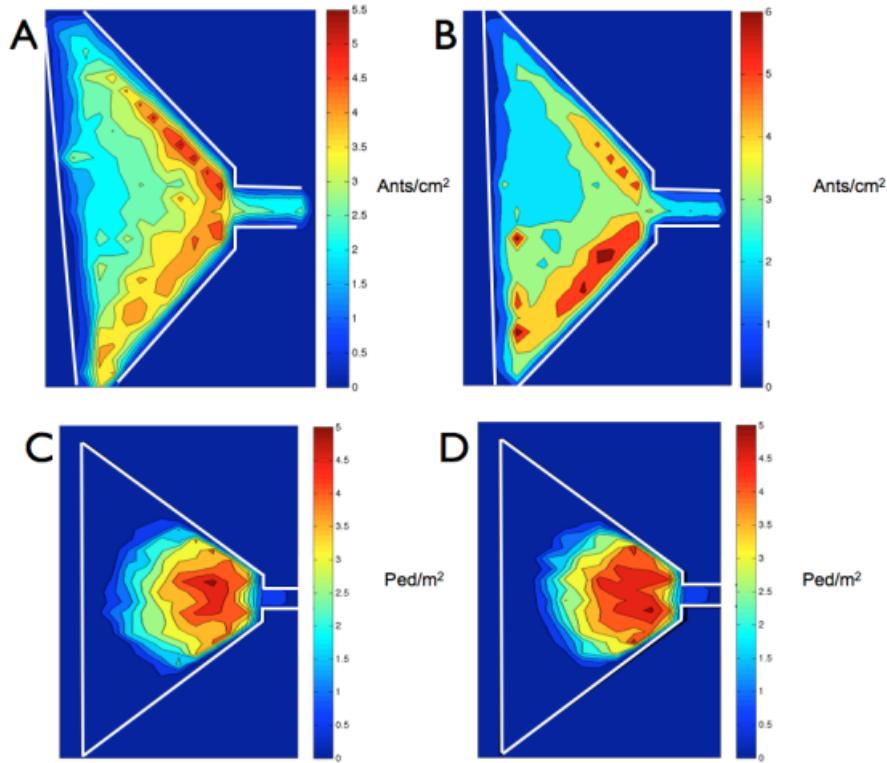


Figure 1.10: Density maps of ants (A and B) and simulation of pedestrians (C and D) in a scenario of evacuation for different excitation level (increases from left to right). For simulated pedestrians, a crowd is formed on the exit, the crowd becomes denser as the excitation level increases. We notice also that the crowd experiences a fall in density just before the opening. On the other hand, ants behave differently, showing little crowding on the exit even when excitation is increased (via addition of lemongrass) (Parisi et al., 2015)

One can see the interesting pattern that emerges in what is defined as *living organisms* regarding the effect of velocity (and level of competitiveness) on the evacuation. Social behaviors play an important role in dictating the state of the system, it is the selfishness in humans and sheep that creates competing individuals inside the crowd, all eager to pass through. Whereas in ants, it is the survival of the colony that is put first resulting in less eagerness and more self sacrifice leading to less concentration on the exit and a more fluid evacuation. From this comparison, we can understand the primordial role that contact forces play in imposing the state of the system during an evacuation.



Crowds and their evacuation procedure are not limited to living organisms, they extend to inert matter. Most recently, evacuation was studied in suspensions in [Souzy et al. \(2020\)](#) where hard colloids are pushed toward an exit by applying a pressure. The effect of opening width on the evacuation's efficiency is reported [Figure 1.11a](#). The survival function of waiting times shows that the evacuation is enhanced by increasing the door's width (*i.e* increasing door width to sphere diameter ratio). They were able to discern three main regimes of the flow with respect to power law tail exponent  $\alpha$ . The flow can either be completely stopped, intermittent or continuous [Figure 1.11b](#). Regarding their experiment, the values of the parameter  $\alpha$  fall in the intermittent regime, mainly because they don't observe a permanent clog, but rather a stop and go behavior. In addition, a similar study investigated the particle jamming in two-dimensional fluid driven flow [Figure 1.11c](#) and compared experimental and numerical results for different flow velocity. [Guariguata et al. \(2012\)](#) reported, surprisingly, no effect on the jamming probability for different driving velocity within the error margins [Figure 1.11d](#). One reason for this behavior is the small increment by which the velocity is varied.

Evacuation studies extend to dry granular systems, since it has been observed that grain silos tend to clog during the emptying process. [Zurigueta et al. \(2014\)](#) investigated the effect of vibrations, head of grains above the orifice and the orifice diameter on the evacuation process [Figure 1.12a](#). They reported a faster evacuation for high vibrations, small grains head height (*i.e* the stack of grains is small) and big orifice size. In another study focused on three-dimensional vertical silos where discharge is dictated by gravity, [Zurigueta et al. \(2005\)](#) reported that, as the ratio between the size of the orifice and the size of the grains is increased, the probability of arch formation and door blocking decreases. They also observed that the arch formation is influenced by the shape of the grain. Indeed, this conclusion is supported by the recent work of [Hafez et al. \(2021\)](#) where the effect of a range of particle shapes on the jamming probability is reported. They concluded, [Figure 1.12b](#), that cubes and three-dimensional crosses are the most prone to clogging due to their ability to interlock [Figure 1.12b](#).

In an interesting study, [Yu et al. \(2021\)](#) observed evacuation mechanisms in a horizontal hopper, where the grains are driven towards the constriction by a conveyor belt. They studied the effect of opening width, hopper angle and belt velocity. They reported, as we have seen by now for the majority of cases, a power law tail for the survival function that becomes steeper with increasing door width [Figure 1.13a](#), and a decrease in clogging probability [Figure 1.13b](#). The authors define  $p$  as the probability of a particle passing through the door without interacting with its neighbors to cause clogging. Hence,  $1 - p$  would be the probability of a particle to interact and clog the exit. We discuss this approach more in details in [Chapter 4](#), [section 4.3.2](#). As for the driven velocity effect, they observed a 'faster is faster' effect [Figure 1.13c](#). They relate this effect to the fact that the pushing force is proportional to the belt velocity. Hence the compression between individuals in the clogging arch does not slow down the grains and the arch is broken easily leading to a decrease in jamming probability with increasing velocity [Figure 1.13d](#).

Work done on crowd evacuation, whether be it experimental or numerical, shows the importance of a survival function in identifying the state of the system. Indeed, a power law tail is the dominant shape that best describes the shape of the survival

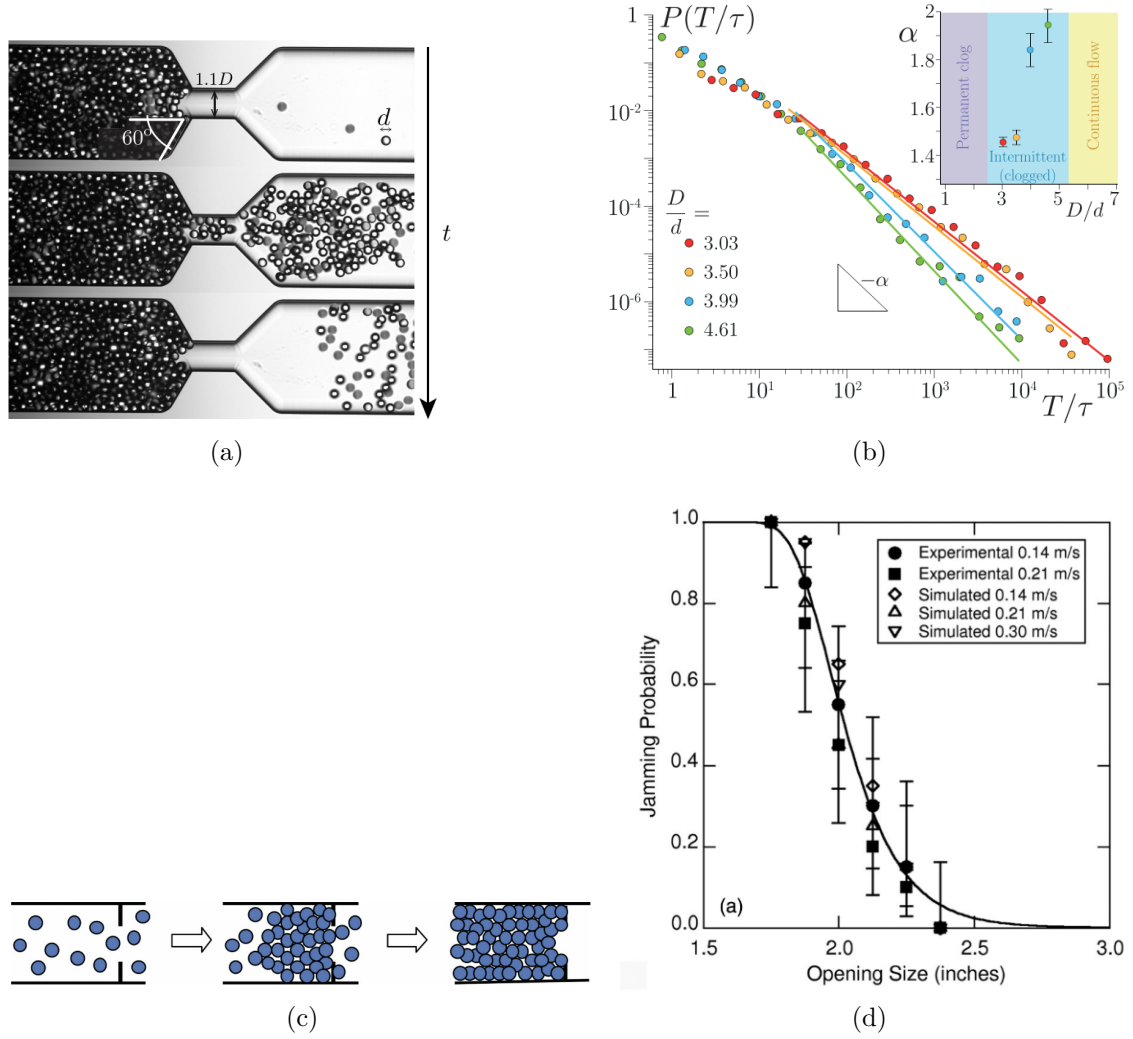


Figure 1.11: a. Snapshot of a colloidal suspension being driven toward the constriction via a pressurized flow. Arch formation is visible on the first and last shot. b. Survival function of time-lapses for different door width to particle diameter ratio re-scaled by the Stokes time. Inset: Evolution of  $\alpha$  with  $D/d$  showing three main regimes, unclogged, clogged and intermittent (Souzy et al., 2020). c. Schematic of particle jamming in a 2 dimensional driven flow showing the arch formation. d. Comparison between numerical analysis and experimental data shows almost no effect of velocity change on the jamming probability (Guariguata et al., 2012). Note that the variation remains in a small margin.

function, with the parameter  $\alpha$  that can be used to identify the state of the system. Mathematically speaking, a quantity  $x$  obeys a power law if it is drawn from a probability distribution  $p(x) \sim x^{-\alpha}$ .

Another way of quantifying the state of the system proposed by Zurigueta et al. (2014), is to look at the *flowing parameter*:

$$\Phi = \frac{\langle t_f \rangle}{\langle t_c \rangle + \langle t_f \rangle} \quad (1.5)$$

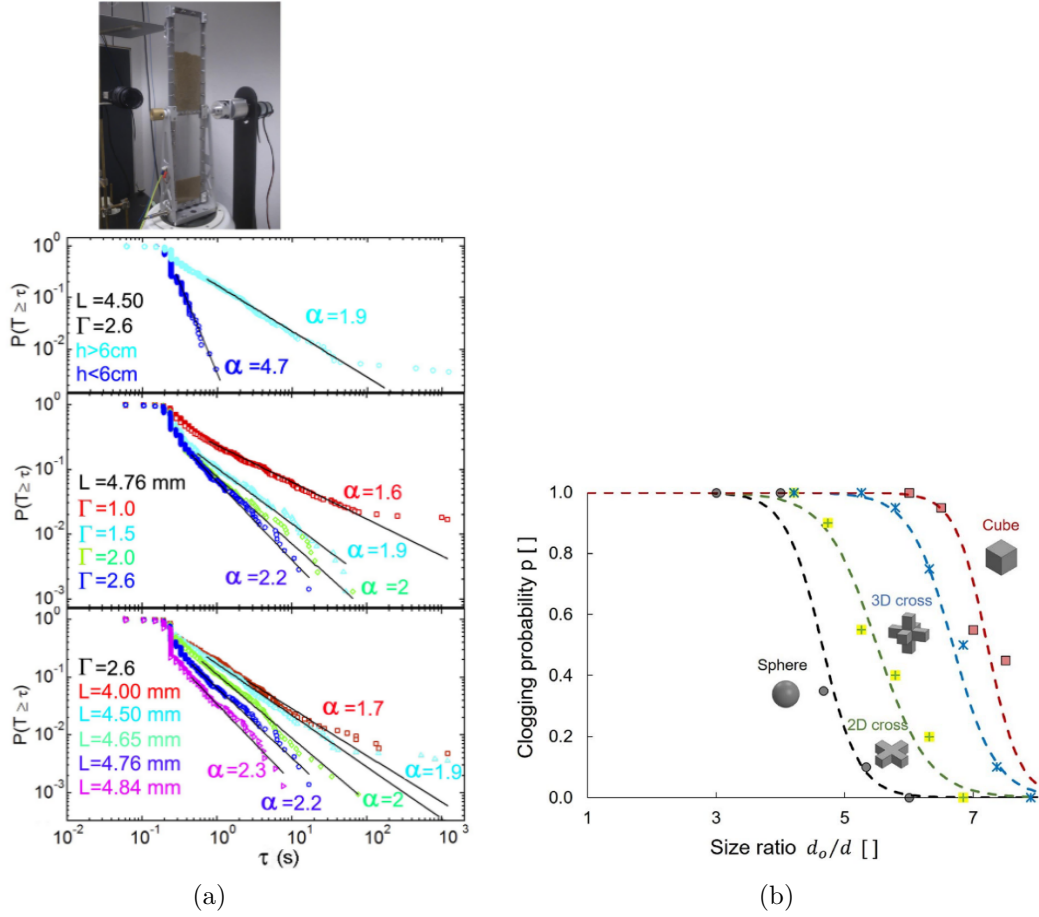


Figure 1.12: a. Top: snapshot of the vertical silo. Bottom: Three plots of survival functions capturing the effect of vibrations, head of grains above the orifice and orifice diameter on the evacuation process. b. Effect of grain shape on the clogging probability. One can see that a shape that encourages interlocking has a higher clogging probability for smaller size ratios.

where  $\langle t_f \rangle$  is the average duration of particles passing without interruption and  $\langle t_c \rangle$  is the average clog duration. Given that definition, it follows that  $\Phi = 0$  when  $\langle t_c \rangle$  diverges and  $\Phi > 0$  when  $\langle t_c \rangle$  is finite. Accordingly, authors defined a system in a clogged state for  $\Phi = 0$ , and in unclogged state for  $\Phi > 0$ . The latter case can be divided into two states. For  $0 < \Phi < 1$  the flow is intermittent and for  $\Phi = 1$  the flow is continuous.

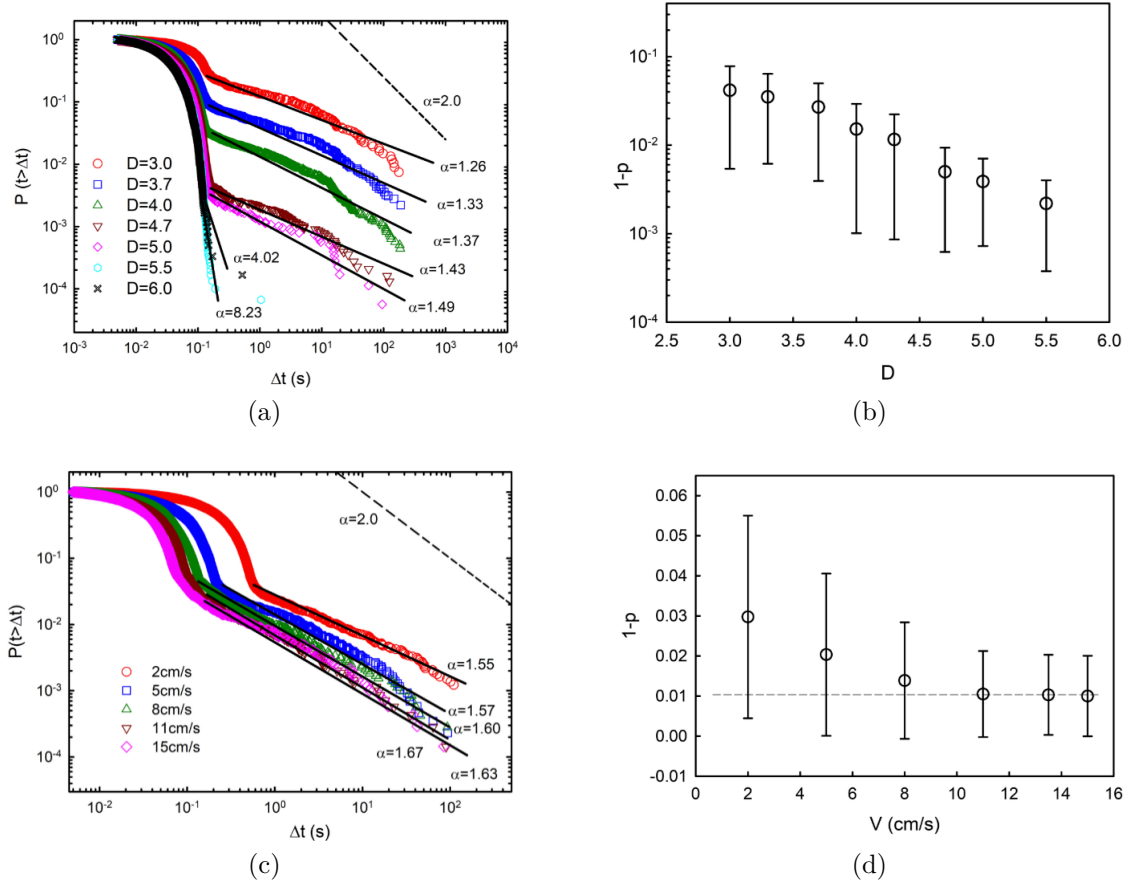


Figure 1.13: Horizontal hopper experiment where grains are pushed toward the opening using a conveyor belt a. Survival function for different opening sizes for a fixed velocity showing the decrease in tail's steepness as  $D$  increases, describing system that is more prone to clog. b. The corresponding clogging probability decreases with increasing  $D$ . c. Survival function showing the effect of velocity change, interestingly, the higher the velocity the lesser the waiting time, an observation in contrast with previous cases, due to the kinetic energy that breaks the arch. d. Clogging probability decreasing with increasing  $V$ . (Yu et al., 2021)

### 1.2.3 Effect of opening angle

Besides velocity and door width, the hopper angle plays an important role in the transition between clogging and flowing. We hear by hopper angle as the angle that the walls of the vertical hopper form with the horizontal plane. It goes to say that a hopper angle of  $90^\circ$ , the geometry becomes a pipeline. In a recent study, López-Rodríguez et al. (2019) investigate experimentally the effect of hopper angle on the state of grains discharge from a two-dimensional silo under gravity action, see Figure 1.14a (where  $\theta$  is the hopper angle). They reported that for very large values of  $\theta$ , the avalanche size  $\langle s \rangle$  grows step-wise with the opening width  $D$ . In contrast, for a flat-bottom silo,  $\langle s \rangle$  grows smoothly with  $D$ . Authors relate this effect to the static equilibrium requirement imposed by the hopper geometry to the arch that arrests the flow. In summary, we can say that the flatter the bottom (*i.e.*

the smaller the hopper angle) the more prone to clogging is the state of the system, see Figure 1.14b.

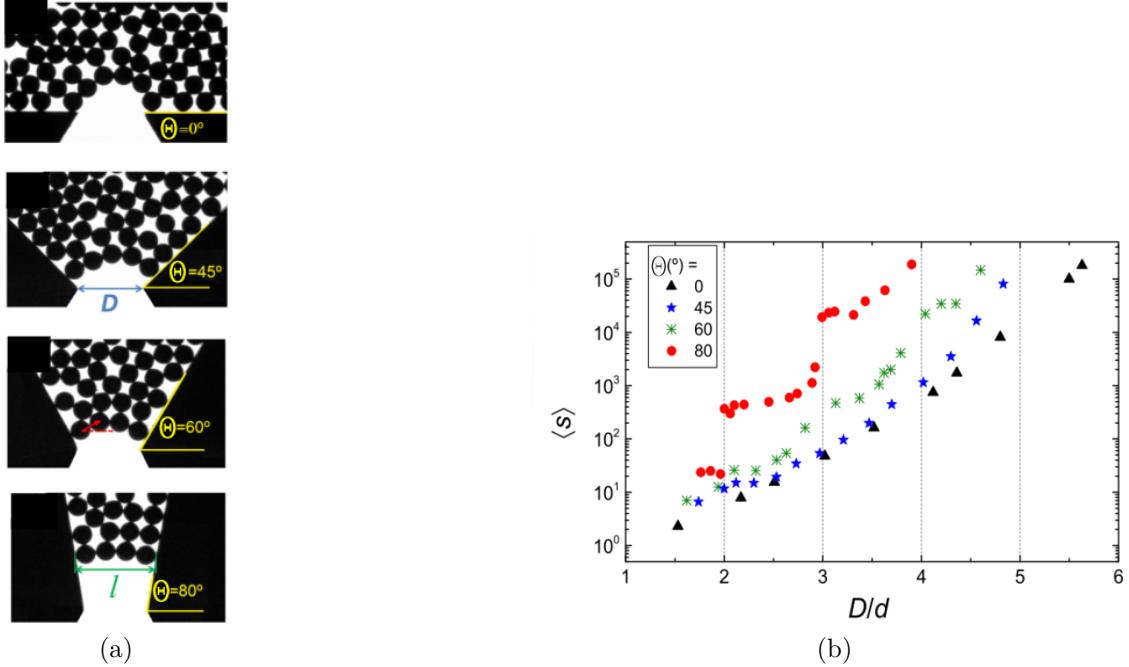


Figure 1.14: a. Snapshots of the experimental setup with zoom on the neck where the angle  $\theta$  is marked. When  $\theta$  approaches the value of  $90^\circ$  the shape of the hopper is close to a pipe. b. Avalanche size in function of  $D/d$  for different values of  $\theta$  where  $D$  is the door width and  $d$  is the size of the grain, showing a step increase for high values, while for flat-bottom hopper the trend is smooth. (López-Rodríguez et al., 2019)

To et al. (2001) tackled the question of hopper angle in a previous work, where they studied experimentally the jamming phenomenon of granular flow in monodisperse disks of diameter  $d = 5$  mm in a two dimensional hopper, see Figure 1.15a. They reported the evolution of the jamming probability with respect to door width to grain diameter ratio for different angles. They found that for the same value of door width, as the hopper angle decreases, the jamming probability increases. This indicates that the flatter the bottom of the hopper becomes the more the system experiences jamming, see Figure 1.15b.

This trend appears to be valid for horizontal hoppers as well. Yu et al. (2021) reported a hardly visible clogging when the hopper angle reaches the value of  $90^\circ$  where the geometry becomes a pipeline. Their study is of great interest given the fact that they looked at the survival function of time-lapses for a fixed door size and fixed conveyor belt velocity all while varying the value of the angle. Figure 1.16a shows the power law tail nature of the distributions with the coefficient  $\alpha$  being very high for  $\theta = 90^\circ$ . We can also notice the transition from  $\theta = 80^\circ$  to  $\theta = 90^\circ$ , where the system is in a flowing state. A flat-bottom hopper where  $\theta = 0^\circ$  is the most prone to clogging. This result is supported by looking at the jamming probability and hopper angle relationship, where the authors note a decrease of  $J = 1 - p$  as  $\theta$  increases until it reaches the maximum value of  $\theta = 90^\circ$  where the clogging

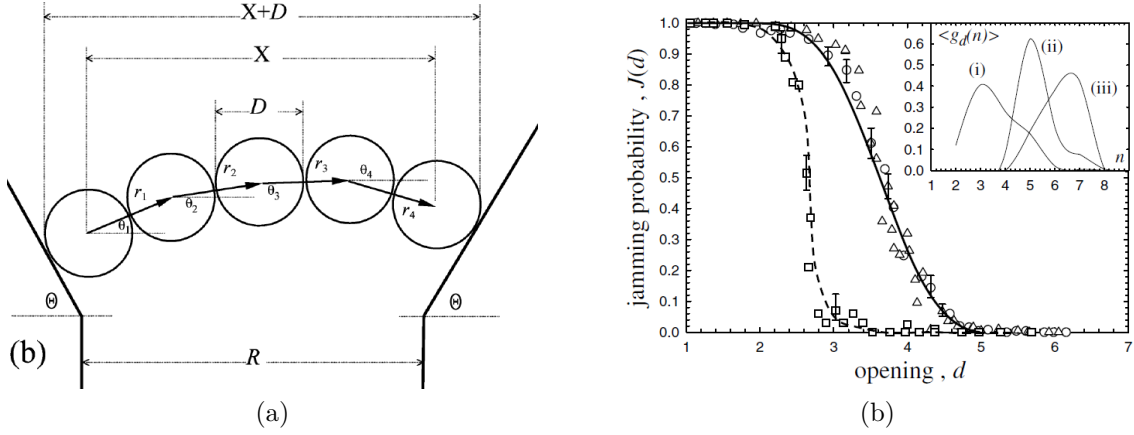


Figure 1.15: Experiment of a vertical hopper. a. Configuration of the arch formation. b. Jamming probability for different hopper angle  $\theta = 34^\circ$  ( $\circ$ ),  $\theta = 60^\circ$  ( $\triangle$ ) and  $\theta = 75^\circ$  ( $\square$ ). The solid line is the approximation from the restricted random walk model. Inset: statistics of the number of disks in the arch in the ranges (i)  $d < 3.3$ , (ii)  $3.3 < d < 4.3$ , and (iii)  $d > 4.3$  respectively where  $d$  is the opening size. (To et al., 2001)

probability becomes null, see Figure 1.16b. Clogging probability is discussed in details in Chapter 4, section 4.3.2.

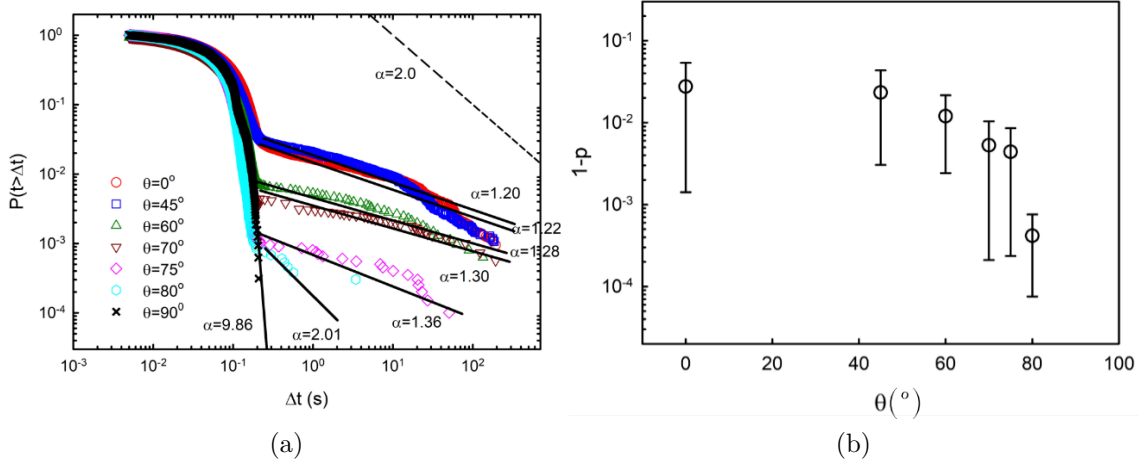


Figure 1.16: Experimental approach to study the effect of angle in horizontal hoppers. a. The survival function of time-lapses for different hopper angle shows a power law tail with the parameter  $\alpha$  that decreases with a decreasing  $\theta$ , meaning that a flat-bottom hopper have the higher blocking probability. For a pipe like geometry at  $\theta = 90^\circ$ , the flow is continuous. b. Clogging probability  $1 - p$  (where  $p$  is the probability of not blocking the exit) to emphasis on the fact that the system tends to flow as  $\theta$  increases. (Yu et al., 2021)

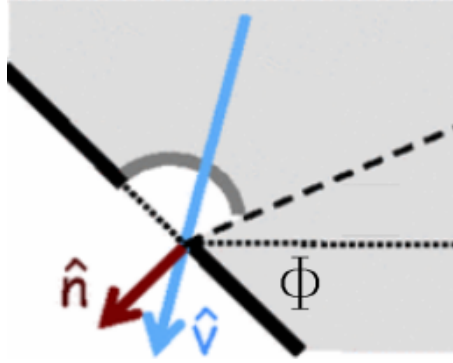


Figure 1.17: Schematic showing the tilt angle  $\Phi(^{\circ})$ . The thick solid lines are the base of the hopper. The small dotted line is the horizontal axis. The vector  $n$  is the directional vector perpendicular to the base and the vector  $v$  is the directional vector of the velocity of the grains. (Thomas and Durian, 2013)

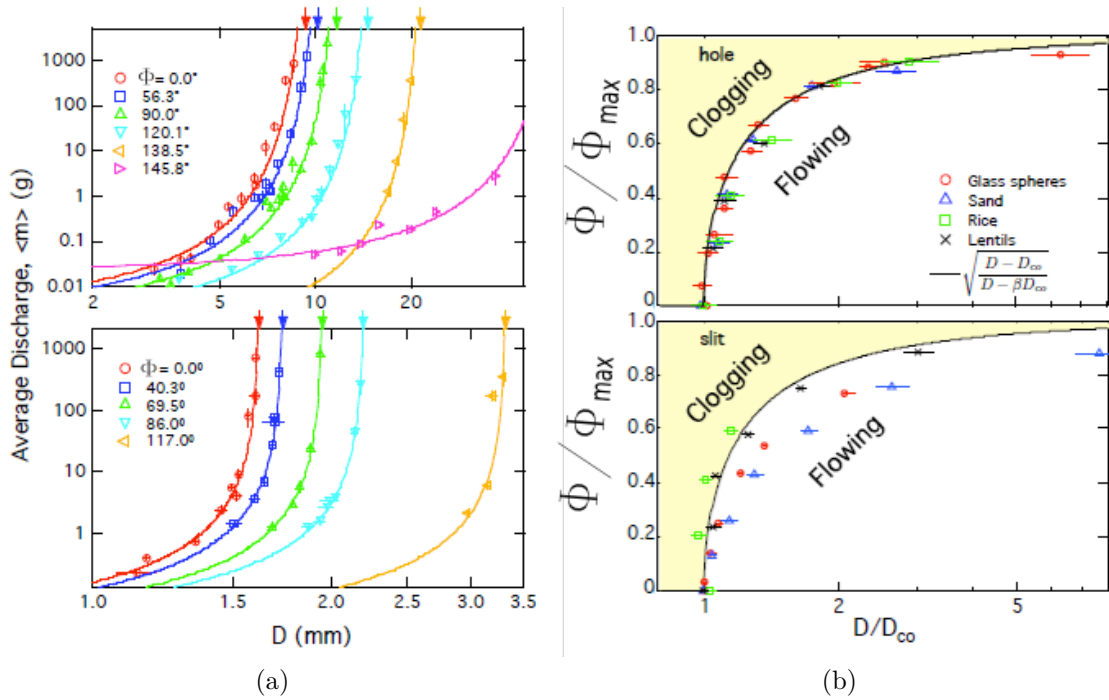


Figure 1.18: a. Average discharge mass  $\langle m \rangle$  as function of  $D$ ,  $\langle m \rangle$  is the equivalent of what we defined as avalanche size in our case  $\langle s \rangle$ .  $\langle m \rangle$  increases with  $D$  until it diverges for a critical value of  $D$  denoted as  $D_{co}$  hence the power law divergence fit. This behavior is similar for both hole (up) and slit (down) and for all values of tilt angle  $\Phi$ .  $\langle m \rangle$  increases as  $\Phi$  decreases for a fixed  $D$ , meaning when the bottom of the hopper is parallel to the horizontal less clogging occurs. b. Clogging phase diagram for hole and slit and for different types of grains showing a clogging regime for small  $D$  and large  $\Phi$  and flowing regime for large  $D$  and small  $\Phi$  (Thomas and Durian, 2013)

Another approach looked into is to change the tilt angle of the horizontal hopper (Thomas and Durian, 2013). The experiment is carried on by keeping a flat bottom while tilting it away from the horizontal. Thomas and Durian (2013) defined the tilt angle as  $\Phi(^{\circ})$  (the angle that the flat bottom makes with the horizontal). They reported the effect of system geometry on the clogging of granular materials for different aperture sizes  $D$  and variable tilt angle  $\Phi$  and found that in general larger tilt angle make the system more susceptible to clogging. An observation that is reasonable, since tilting the bottom of the hopper means deviating the alignment between the particles and the axis of the aperture whereas changing the hopper's angle as in previous cases the alignment is conserved and grains fall directly toward the opening. Measurements of the distribution of mass discharged between clogging events, an equivalent parameter to the avalanche size, as function of  $D$  allow a quantification of the effect of  $\Phi$ . In addition, values of the critical diameter  $D_{co}$  are obtained by extrapolating to the critical size of aperture at which the average mass diverges, see Figure 1.18a. Authors repeated the study for a range of angles and were able to map out the clogging phase diagram as a function of  $D$  and  $\Phi$ . They reported a free flow regime for large values of  $D$  and small values of  $\Phi$ , whereas clogging regimes is dominant for small values of  $D$  and large values of  $\Phi$ , see Figure 1.18b. They took their study a step further and examined the effect of a slit versus orifice types of aperture, as well as different types of grains.

We can clearly see the importance of the opening angle on the evacuation process and the way this parameter affects directly the phenomenology behind clogging, mainly arch formation.

### 1.3 Micro-swimmers

We have dissected the *Crowd* part of our title, it is therefore only logical to move on and discuss the second half of our study, that is micro-swimmers. We hear by micro-swimmer, as an entity that moves through a liquid by modifying its shape creating therefore a certain swimming mechanism. It exists in nature a wide variety of micro-swimmers dotted with very different yet impressive swimming mechanisms. To name few examples, the bacteria *E. Coli*, propelled by flexible filament of 20 nm in length. When rotated in a counter-clockwise direction, they induce the motion of the bacteria at a velocity of about 20  $\mu\text{m/s}$  (Berg, 2003, 2004). In their study, Turner et al. (2000) reported the behavior of the filament, they noticed that when one part of the rotors changes its rotation to the opposite direction, the filaments enter a de-synchronization, inducing a change in the direction of swim of the *E. Colis*, in general, bacteria adopt a similar mechanism in order to propel themselves.

Another type of organism that adopts a different propulsion mechanism, is the eukaryote cells. These cells are by nature bigger in size than the bacteria and are propelled by flagella that are larger than the filament used by their counterparts from bacteria (Sheikh et al., 1997). Usually, their body size can attain around hundred microns. Interestingly, swimming method inside this group of swimmers differs greatly, and can change from one specie to another.

Furthermore, it exists a novel category of micro-swimmers fabricated by humans and known as artificial micro-swimmers. In fact, these micro-robots are able to be



activate mechanically or chemically in order to form a crowd. The most famous example used in laboratories is the Janus non-deformable particle. The particle is built from latex and covered in platinum that catalyzes the hydrogen peroxide into oxygen and water. The asymmetric formation of gas is what induces a swimming motion (Palacci et al., 2010) (Howse et al., 2007). Another propulsion mechanism is to applied electromagnetic field for micro-robots made from para-magnetic materials. We recall here the use of Quincke rollers in Chardac (2021).

It is this swimming mechanism that renders the study of micro-swimmers interesting. In fact, and in contrast with passive suspension like granular systems, active suspension transfer some their internal energy to the fluid in which they swim. This causes out-of-equilibrium effect that are of huge interest for the point of view of hydrodynamic and physics. For instance, the viscosity of the fluid is seen to be affected by the movement induced by such swimmers. Using standard rheology techniques, Rafai et al. (2010) showed that the viscosity is affected by the motion of living *Chlamydomonas Reinhardtii* algae comparison to dead ones Figure 1.19a. This is due to the hydrodynamic interactions that is generated from their propulsion mechanism (pullers), leading to an increase in viscosity. In addition, plotting the average swimming velocity in function of the inverse of the viscosity in Figure 1.19b, the authors found a linear relationship governing the two physical quantities. This leads to the conclusion that the swimmer moves in the fluid at constant force given by the Stokes-Einstein law for a sphere (Einstein et al., 1905):

$$v = \frac{F}{6\pi\eta a} \tag{1.6}$$

where  $v$  is the average swimming velocity,  $F$  is the force,  $\eta$  is the viscosity and  $a$  is the characteristic length of the swimmer. This relationship shows the effect of microscopic properties like swimming velocity on the macroscopic parameter like the viscosity.

In a relatively short time span, work on crowds enduring an evacuation witnessed fast growth. From the first numerical results showing a paradoxical *faster is slower effect* to the experiments on living matter where the effect was first seen and quantified, to the extrapolation of the analysis to different types of systems. It is then that a pattern started to emerge. Mainly, the faster the attempt at evacuating the slower the process. In addition, geometrical factors affect as well the state of the system. However, the consensus regarding this "universality" is based on crowds governed by short range forces. The "wet" microscopic world is largely overlooked if not forgotten.

It is in the purpose of this work to analyze active suspensions undergoing an evacuation through the development of an adequate and reliable set up. The "universality" of the paradox is put to test as we look at whether the presence of hydrodynamic forces affect the evacuation or not. We look at different scenarios ranging from velocity variation to geometrical effects and compare to the literature in order to understand the phenomenology behind the behavior.

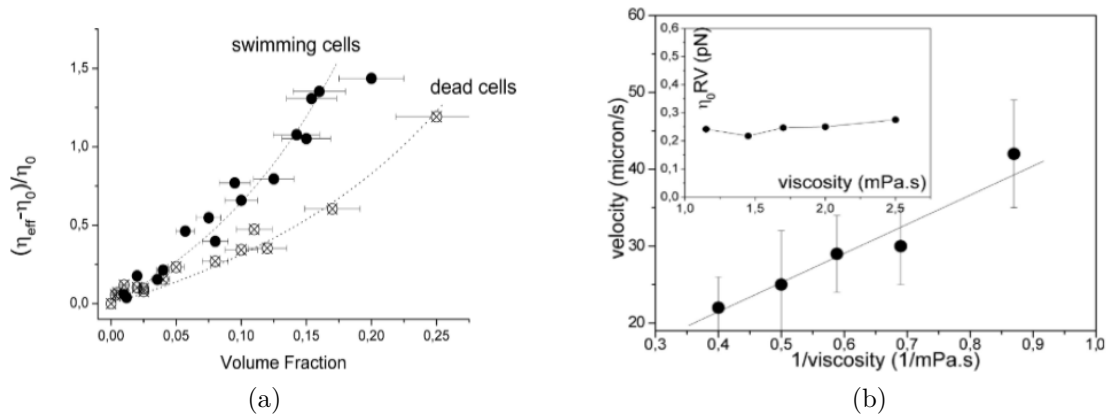


Figure 1.19: Rheological study of the behavior of the *Chlamydomonas Reinhardtii*. a. Relative viscosity as a function of the volume fraction of cell. This graph shows the effect of living and dead cells on the viscosity. Living cells act on the medium by increasing its viscosity. b. Average swimming velocity as function of the inverse of the fluid viscosity. The velocity is inversely proportional to the viscosity following the Stokes-Einstein law and suggesting a constant propulsive force. (Rafai et al., 2010)

## 1.4 Outline

In the first chapter after the introduction, we discuss in details our experimental approach where we introduce the micro-fabrication process that allows us to control the geometrical parameters of the channel where our *crowd* will be swimming. In addition to the microscopy set up used in order to observe clearly the motion of the suspension, followed by a description of the tools used in the post processing and a detailed explanation of the calibration procedure. It is after the build up of our experimental arsenal that we introduce the type of suspensions we work with, that is the *Chlamydomonas Reinhardtii* algae, a photo-tactic micro-algae that lives in non-salty waters. We describe the methodology by which we insure a healthy and homogeneous supply of these cells inside our team, and we report their behavior in different *ex-situ* scenarios. We end this chapter with a step by step guide on the manner by which we conduct a typical experiment.

It is then after that we can begin our analysis. Chapter 3 is a case study chapter, where we take one experiment and detail the process of data treatment. First, we specify the sampling window, then we proceed to dissect the process that goes into data analysis. We predict the trend of the data via a probabilistic model and we extract the expression of the complementary cumulative distribution function. In addition, we explain the statistical validity of the parameter  $\alpha$ . Finally, we give the outputs that are of importance to our analysis. We tackle the case study from two different point of views, mainly the waiting time and the avalanche sizes.

Chapter 4 is where we present the first experimental results concerning the effect of swimming velocity and door width. We observed an interesting relationship between the two parameters that lead us to build a  $D - V$  diagram. This diagram

allows us to determine a transition zone where the system goes from a jammed state to an un-jammed one. More precisely, we found the existence of a critical value of door width that we denote  $D_c$  for a given velocity, above which the evacuation is continuous.

A comparison between the evacuation behavior in active suspensions and granular systems suggests underlying similarities in jamming mechanisms. When it come to granular system, it has been established that clogging is due to arch formation. Arching is also found to be highly dependable on the opening angle. In order to investigate to what extent this similarity between systems goes, we opt to see in Chapter 5 the effect of angle change. Indeed we observe a striking difference with respect to granular system. We give a causality related to the behavior of the suspensions.

Finally we end the manuscript by a conclusion and some perspectives of the work that can follow, mainly to apply our observations to a numerical model.

## Materials & Methods

*Ma chère amie, le bon sens nous dit que les choses de la terre n'existent que bien peu, et que la vraie réalité n'est que dans les rêves.*

Charles Baudelaire - *Les Paradis Artificiels* - 1868.

### Contents

---

<b>2.1</b>	<b>Standard Micro-fabrication</b>	<b>26</b>
<b>2.2</b>	<b>Microscopy &amp; Acquisition</b>	<b>28</b>
<b>2.3</b>	<b>Particle Tracking Velocimetry (PTV)</b>	<b>28</b>
<b>2.4</b>	<b>Density Measurements &amp; Calibration</b>	<b>29</b>
<b>2.5</b>	<b><i>Chlamydomonas Reinhardtii</i></b>	<b>32</b>
2.5.1	Cell Culture	33
2.5.2	Response to Light	34
2.5.3	Effect of viscosity on swimming velocity	36
<b>2.6</b>	<b>A typical Experiment</b>	<b>39</b>

---

In this chapter, we introduce in details the experimental methods we employ in order to build a reliable experiment able to tackle the problematic we presented in the previous chapter. First, we present the standard micro-fabrication techniques used to build the channels in which our suspension swims. Second, we lay out the microscope/camera set up used for a proper acquisition with adequate spatial and temporal resolutions. In addition, we introduce the algorithm used to locate and track individual cells from one frame to another. For density measurements, we present the calibration method by which we correlate pixel intensity to volume fraction. We then describe in details the well established cell culture protocol that we follow in order to maintain a constant supply of *Chlamydomonas Reinhardtii* (CR). We end the chapter by describing the methodology by which a typical experiment is conducted.

## 2.1 Standard Micro-fabrication

Cells are observed swimming in micro-channels made from a transparent silicone-like materials known as Polydimethylsiloxane (PDMS). Fabrication of these channels follows multi-steps protocol.

The first step is to cast a mold by engraving the desired print on a SU-8 resin via a soft lithography process. Channel height is also determined through a spin coating process (Qin et al., 2010). Figure 2.1 summarizes the main steps of the standard soft lithography process used in our laboratory and executed in dedicated, dust free, space known as a Clean Room (*a.k.a* White Room) where temperature, pressure and humidity are controlled. First, the wafer is heated for 2 hours at a temperature  $T = 200\text{ }^{\circ}\text{C}$  to remove any traces of water, the dried wafer is then placed on a spinner where it remains steadily attached due to vacuum. It is at this moment where the resin of type GM-1070 is poured through a syringe attached to a pump. The coating is done on two stages, the first at 500 rpm and for a duration of 10 s to evenly spread the resin and the second at 3900 rpm for 40 s to get a desired thickness of  $h = 20\text{ }\mu\text{m}$ . Both rotations are done at an acceleration of 100 rpm/s. With the resin evenly spread, the wafer goes through a first baking procedure where the plaque is heated from room temperature to  $65\text{ }^{\circ}\text{C}$  at a rate of  $2\text{ }^{\circ}\text{C}/\text{min}$ . After 15 min, the temperature is brought up to  $95\text{ }^{\circ}\text{C}$  where it stays for 30 min marking the end of the pre-bake and the hardening of the resin allowing the fixation of the thickness. A mask of the desired print is then placed on top of the wafer, the design is a transparent pattern drawn on the mask allowing U.V. light to go through and activate the resin. A second baking step, defined as the post-bake, is needed before submerging the wafer in a development bath of PGMEA (Propylene glycol monomethyl ether acetate) in order to wash away the non-activated areas leaving the imprint of the channels. A final baking at  $130\text{ }^{\circ}\text{C}$  for 2 h hardens the mold and renders it ready to be used.

Masks are supplied from the Swiss manufacturer SELBA, and are printed with high resolution of 25400 pixel per inch (Lim et al., 2014). Figure 2.2 shows the print of a typical mask and the corresponding mold engraved on a wafer. A degassed PDMS solution formed from 90 % silicon and 10 % hardener is poured on the mold to take the shape of the channel. Figure 2.3 shows a simplified schematic of the procedure, where after the pouring the PDMS is left to cure at  $65\text{ }^{\circ}\text{C}$  for 2 h, after which the hardened PDMS is detached from the mold and bonded to glass via plasma-oxygen exposure. Inlet and outlet holes are made to insert our suspension.

Through the plasma-oxygen process, the activated surface of the channel and the glass becomes hydrophylic. When put into contact with each other, a strong bond takes place, this is essential to our experiment since a strong bond leads to the structural integrity of the channel, decreasing the probability of a detachment when injecting the suspension via a syringe. It is directly after gluing the channel to the glass that we fill the channel of a solution of Bovine Serum Albumine (BSA), a protein that reduces wall adhesion.

The traditional soft lithography technique described above relies on the import of masks from SELBA based in Switzerland, this induces waiting time and delays. It is for this reason that we use the newly acquired Dilase 250 from Kloé to create new molds described in Chapter 5, section 5.1. The Dilase 250 is a tabletop high

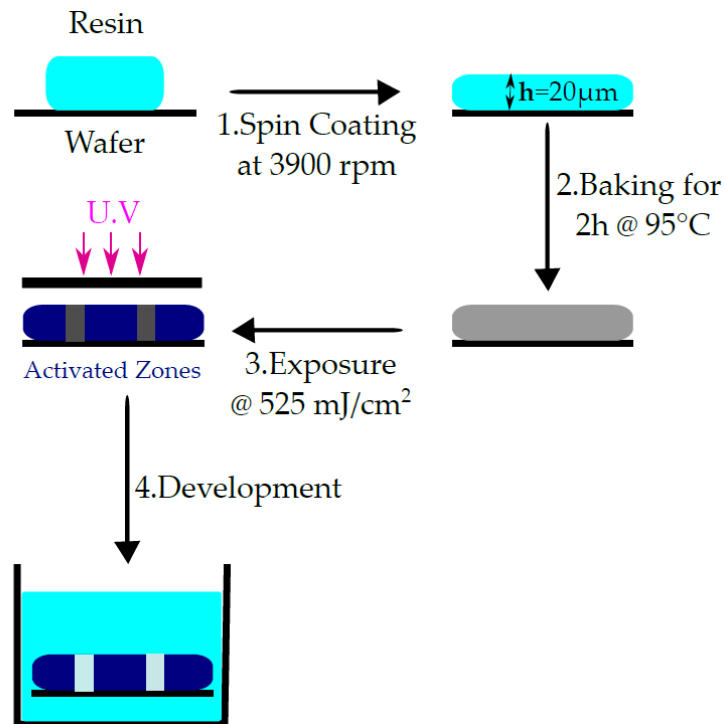


Figure 2.1: Schematic representing the main steps needed to make a mold. 1. The resin is poured on a dried wafer attached to a spinner via vacuum, the rotation speed dictates the thickness. The second phase 2. consists in baking the wafer that is now coated in order to harden the resin and prevent it from potentially spilling over and modifying the thickness. 3. The exposure is done by placing a mask of the desired print in contact with the hardened resin and shine U.V light through the transparent area allowing the resin to get activated. The final step 4. is necessary to remove all non-activated area or excess by immersing the wafer in a development bath.



Figure 2.2: Typical mask provided by SELBA. The white area allows the passage of U.V. rays to activate the resin following the desired shape. Black areas obstruct the passage of the light and covered zones remain inactivated.

resolution laser lithography system. The channels are engraved on the photosensitive resin via a laser. Designs are drawn using FreeCAD and fed to the machine.

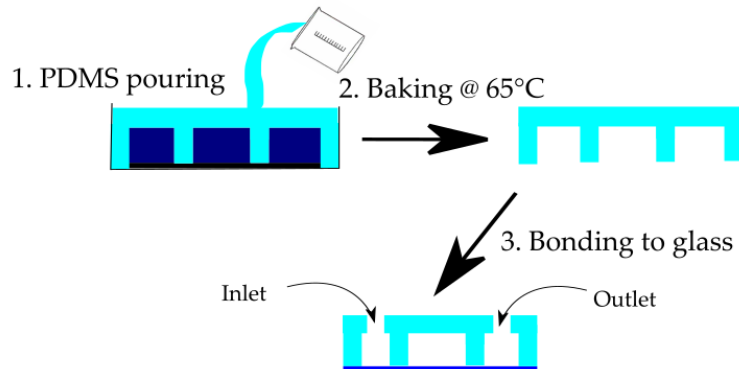


Figure 2.3: Schematic representing steps of PDMS pouring. 1. The mixture of silicone and hardener is poured on the mold after degassing and 2. left to bake for 2 h at 65 °C to harden it, it is then removed and bonded to glass through plasma-oxygen exposure.

## 2.2 Microscopy & Acquisition

Channels are observed under a bright field inverted microscope, the Olympus IX71 with a  $\times 4$  objective. Acquisition is done via a 14 bit AVT camera, the Prosilica Gx3300, coupled to the microscope, with a resolution of  $5.5 \mu\text{m}$  per pixel and a sensor with a field of view of  $3296 \times 2472$  pixels. By not using any binning in both the horizontal and vertical dimension, we get a resolution of  $1.375 \mu\text{m}$  per pixel (for the  $\times 4$  objective). We aim at spatial resolution of  $100 \times 2000$  pixels, allowing us to capture suspension and calculate the average swimming velocity in the upstream, downstream and neck regions, all while not taking a lot of memory space, hence increasing the temporal resolution. The frequency of acquisition is chosen to be 20 hertz or 20 frames per second for a total number of frames of 40000, equaling 33 min worth of recording. We find that this compromise between spatial and temporal resolution is the best fit for our study since it allows us to record for longer times all while disregarding regions that are unnecessary. In addition, as it will be investigated in details further in the manuscript in section 2.5.2, our cells are reactive to light, therefore the acquisition set-up is put in total darkness, and precautions are taken to filter the light coming from the microscope so it doesn't bias the recordings.

## 2.3 Particle Tracking Velocimetry (PTV)

Analyzing the trajectories of our suspensions and being able to know the location of each particle at a given time is crucial for our study. An effective tool that allow such detailed analysis is the *trackpy* library implemented in python (Crocker & Grier, 1996; Allan et al., 2021). The package is able to detect dark particles over bright background, the user gives information about the size of the object in pixels and the light intensity. After having identified individual object in all given frames, the algorithm uses the closest neighbor method to link particles and reconstruct

their trajectories; basically it searches in an area around a particle from frame  $i$  and links it to the closest particle present in the same area in frame  $i + 1$ . A reasonable value of the search radius is an input made by the user. This procedure allows us to obtain the  $x$  and  $y$  position for individual particles for every frame. Figure 2.4a shows an example of a detection scenario of particles swimming in a capillary tube of  $2 \times 0.2 \text{ mm}^2$  and a typical plot of trajectories built from values given by the tracking algorithm.

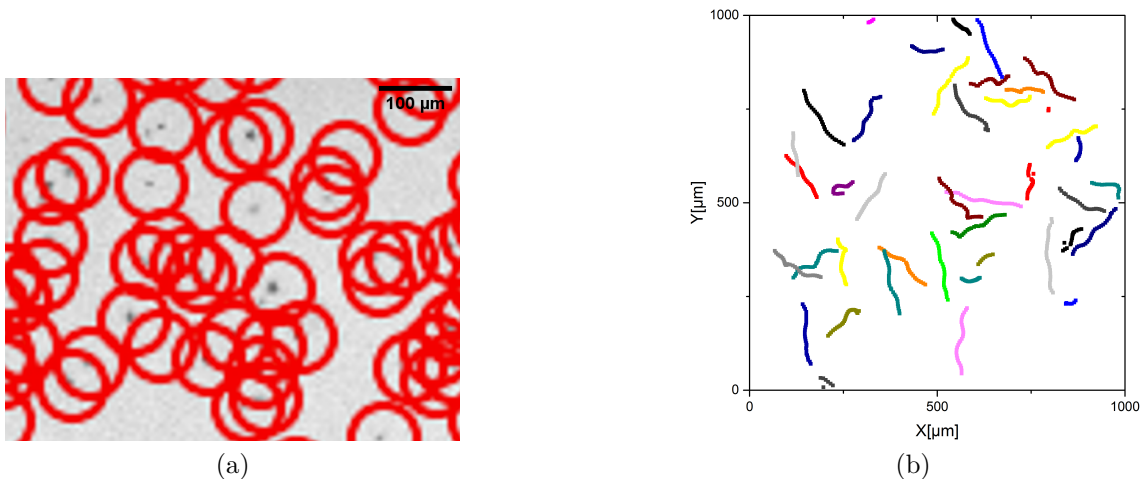


Figure 2.4: a. A snapshot showing the degree of accuracy of the *trackpy* algorithm in detecting particles. Red circles are generated by the algorithm when it detects a particle b. Reconstruction of particle trajectories from the data acquired via tracking.

In our study, we are not only interested in constructing individual trajectories but also need the velocity information. We look at the velocity from a population point of view instead of individuals. Already the tracking routine gives us the spatial and temporal information. With that it is straightforward to calculate the velocity of each particle over a  $\frac{1}{20}$  s. Indeed, some particles present anomalies in their behavior, and need not to be taken into account in our analysis or else the result will be biased. Therefore we take good care in objectively discard any particle that has a null velocity for more than 90 % of the time, equivalent to a total of about 200 particles. A histogram of velocity distribution is plotted as in Figure 2.5 and can be fitted by a Gaussian fit, from which the mean swimming velocity of the population  $V$  is extracted and corresponds to the peak with  $V = 163 \text{ } \mu\text{m/s}$  and a standard deviation equal to the width of the fit  $std = 37.48 \text{ } \mu\text{m/s}$ .

## 2.4 Density Measurements & Calibration

Analysis tools and methods presented in section 3.2 require the ability to measure locally the evolution of the volume fraction ( $\phi$ ) throughout the experiment. In fact, crowd formation is identified by a phenomenon of clustering causing an increase in the local density. In those regimes particles become so closely packed that it



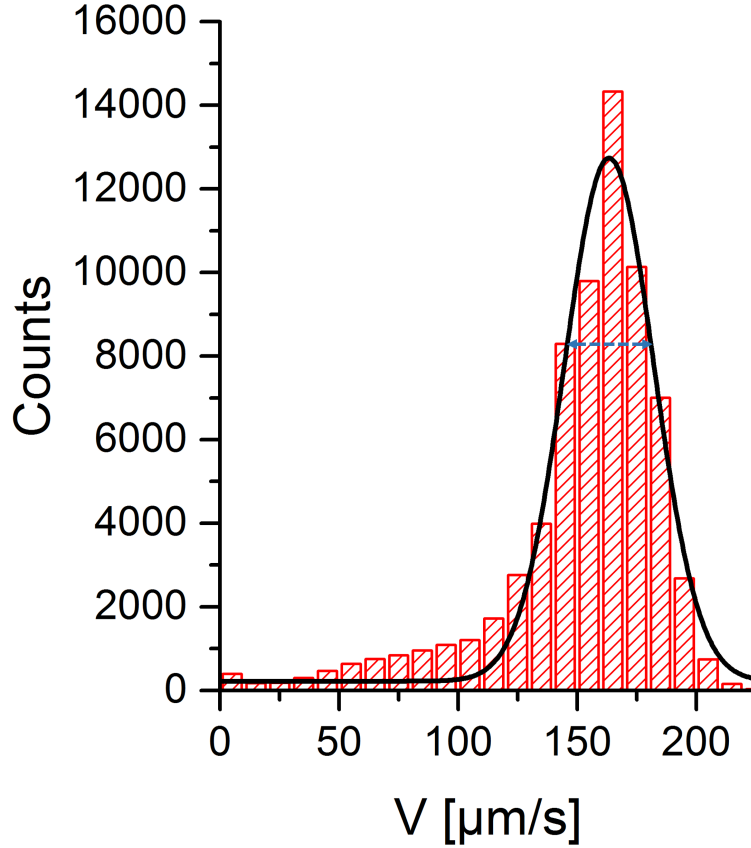


Figure 2.5: Velocity histogram showing the wide range of values present in a typical suspension and the Gaussian fit in solid black line from which the values of the swimming velocity  $V$  (peak value) and the standard deviation are extracted (dotted arrow).

becomes quasi-impossible to count them. Therefore the traditional technique used in diluted regimes to calculate  $\phi$  based on counting, fails. To solve this issue we opt to measure the grey level and tie it to the absorbance. Following Beer-Lambert law, there exists a relationship between the volume fraction  $\phi$  (or density) and the absorbance  $A$  via the equation:

$$\epsilon l \phi = A = -\log \frac{\langle I \rangle}{\langle I_0 \rangle} \quad (2.1)$$

where  $\langle I \rangle$  is the intensity averaged over all the pixels in the image,  $\langle I_0 \rangle$  the average intensity of the background where no particle are present,  $l$  the length of the optic trajectory and  $\epsilon$  the molar attenuation coefficient. Previous studies done using *Chlamydomans Reinhardtii*, mainly in the work of [Martin \(2017\)](#), show that the law is valid for diluted regimes, where volume fractions are below 2%. It is important to us to investigate the validity of the Beer-Lambert at high concentration and see if the linearity between  $\phi$  and  $A$  still stands for those regimes.

To do so, we opt first for measuring volume fractions in diluted regimes by

simply counting particles, where the number  $N$  is related to  $\phi$  via:  $\phi = N \times \frac{V_{cell}}{V_T}$ , where  $V_{cell}$  is the volume of one CR, and  $V_T$  is the volume of the geometry with a depth of 20  $\mu\text{m}$ . Due to their spherical shape, we consider the volume of CR to be that of sphere. Cells are neutralized by adding alcohol to the medium, then injected in wells of volume 0.4 mL (type *Thermo Scientific*), where they sediment, counting in diluted regimes is done using the *trackpy* routine. On the other hand, measurements of absorbance are done by observing each well using the apparatus described in section 2.2 and using a *python* routine to calculate  $I$  for each pixel and average it over the whole image. Relating the volume fraction obtained by simple counting and the absorbance calculated via grey levels intensity in Figure 2.6a, we notice that the linearity is broken for values of  $\phi \geq 2.5\%$ .

Indeed, in crowd formation we expect to have much larger concentrations as our cells aggregate in front of the opening. Hence, we have to extend the calibration to high density regimes. Immediately we are confronted to an issue, the *trackpy* routine loses its ability of detection at high  $\phi$ . To counter this obstacle, we resort to a technique known as *Log Dilution*. Using a centrifuge we obtain a concentration 50 $\times$  higher than the initial one. Letting the cells sediment, we remove the excess liquid leaving a highly concentrated cells' suspension. We then dilute 10 $\times$  resulting in a regime where we can easily count and can calculate the volume fraction  $\phi_{diluted}$ . If one supposes that the number of cells present in a solution diluted 10 $\times$   $N_{diluted}$  and in the initial one  $N_{concentrated}$  are proportional to one another, one can write  $N_{concentrated} = 10 \times N_{diluted}$  and consequently  $\phi_{concentrated} = 10 \times \phi_{diluted}$ . Figure 2.6b represents the calibration to obtain the relationship between volume fraction and absorbance extended to high density regimes. We use a fourth degree polynomial to characterize the relationship:  $\phi = aA^4 + bA^3 + cA^2 + dA + e$  where:  $a = -9.16$ ,  $b = 16.8$ ,  $c = -7.52$ ,  $d = 1.38$  and  $e = -0.016$ .

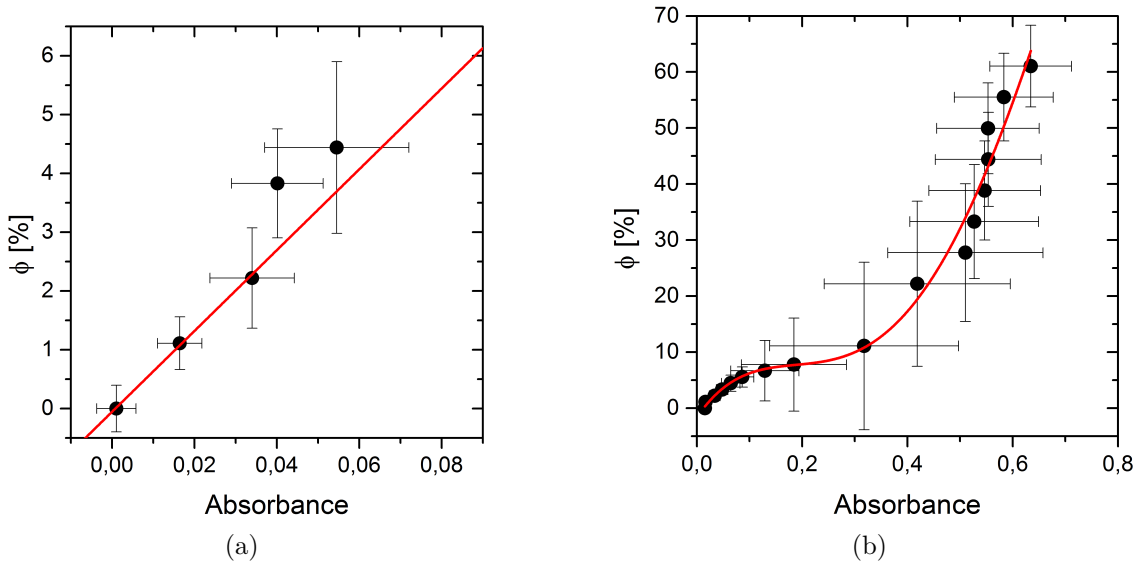


Figure 2.6: a. Validity of the Beer-Lambert law for density regimes  $\phi < 2.5\%$ . b. Calibration extended to the high concentration regimes, where the relationship can be characterized by a fourth polynomial  $\phi = aA^4 + bA^3 + cA^2 + dA + e$ .

## 2.5 *Chlamydomonas Reinhardtii*

Up till this point we have described in details the technical tools needed in our arsenal to tackle our problematic. But the most important of them all is our suspension system, that needs a special protocol to insure routinely healthy and clean supply of *Chlamydomonas Reinhardtii*.

The *Chlamydomonas Reinhardtii* (Harris et al., 2009) is a micro-algae with non-salty waters as natural habitat. Its anatomy consists of a main body with a spherical shape and a size of 10 micrometers, to which are attached two flagella of same length. The beating of these flagella induces the motion by which the alga discovers its environment in a quest for food. A zoomed picture, Figure 2.7, of the alga reveals a body rich in chlorophyll inside a chloroplast, giving the alga the ability to use photosynthesis. This particular physiology is at the origin of the name that originated from Greek and can be roughly translated to "unique coat" with *chlamys* meaning coat and *monas* meaning unique. The alga detects the presence of light via an "eye spot" that is sensitive to green light with a wavelength of 510 nm (Martin et al., 2016), and can direct itself toward regions where it can activate its photosynthesis. This motion toward the light is known as positive phototaxis. Some strains exhibit a contrary behavior where they tend to flee light, a phenomenon known as negative phototaxis.

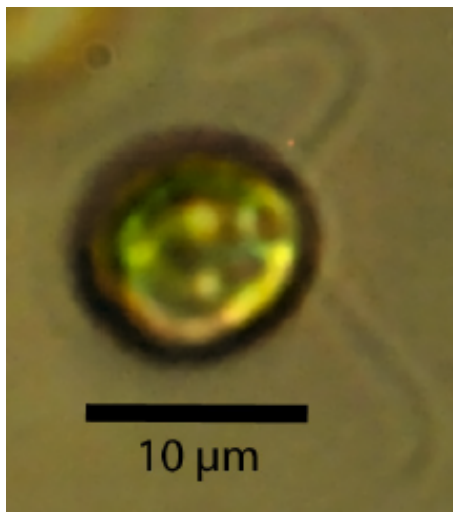


Figure 2.7: Zoomed picture of a *Chlamydomonas Reinhardtii* showing the dominant green color. The spherical shape makes it easy to replicate in numerical analysis. The two flagella can also be distinguished. (Brun-Cosme-Bruny, 2019)

Before being used as a model studied from the point of view of physics, the *Chlamydomonas Reinhardtii* has been subjected to detailed investigations from the biologists' community. It has helped them understand better photosynthesis, flagella in plants and the study of genomes. Interestingly enough, a resemblance is present between the "eye" of the alga and that of the animal world in the sense that both have a protein known as rhodopsin (Harris et al., 2009).

Beyond the biology realm, interests in micro-algae are also rising in industry. On one hand its capacity of absorbing carbon dioxide in big quantities and the possibility

of it being used as a bio-fuel (Scranton et al., 2015) and sustainable heating source plays a big role in the market orientation towards a more eco-friendly mode of production and consumption. On the other hand, the waste can be used as feeding source for cattle. The easiness by which its genome can be modify in order to get desired properties makes the field of micro-organisms an attraction for investments (Batyrova & Hallenbeck, 2017). One example is increasing hydrogen production by making the environment poor in sulfate (Tsygankov et al., 2006)

Its spherical shape makes it easy to build numerical model in order to understand it's swimming and interactions with its neighbors. In our case, we can compare the crowd motion to a granular system as we will see later on in Chapter 4.

### 2.5.1 Cell Culture

A crucial practice for our investigation is to keep an homogeneous and consistent supply of *Chlamydomonas Reinhardtii*. Given that there exists a large variety of strains, we restrict our usage to the train CC-124, with its negative photo-taxis (Ide et al., 2016) and high sensibility to light. This strain has been previously used in work done by our group. A procedure is developed and consists in growing cells in an incubator ICP 110, where their growth conditions are well regulated. A circadian cycle is achieved via 4 white neon lights that replicate a 14h/10h day-night cycle. Cells reproduce at night and scavenge for light necessary for photosynthesis during the day. Temperature is set at 22 °C for optimal growth conditions. Strains are provided by the Chlamydomonas Resource Center<sup>1</sup>.

In order to obtain cell suspension for our experiment we followed different steps. The *Chlamydomonas Reinhardtii* are received as a green paste form that we spread out on petri-dish filled with a nutriment enriched jelly-like material made from a mixture of Agar-Agar and TAP (Tri-acetate-phosphate). We define this step as solid culture and it is repeated on a weekly basis to sustain a continuous and healthy supply of cells. Our team has developed a reliable protocol in order to obtain a final suspension of homogeneous size. The process, summarized in Figure 2.8, is based on a two-steps procedure. The first consists in harvesting the solid culture and diluting it in 50 mL of TAP, hence creating a "mother solution". The suspension is then placed in the incubator for 3 days. This period is not arbitrary, in fact Figure 2.9a shows that the volume fraction increases during three days before stabilizing indicating that no new cells are being produced due to the lack of nutriments. Looking at the volume fraction of the suspension as a whole gives us only the information from a biomass point of view which includes both living and dead cells. Using the photo-tactic properties of the *Chlamydomonas*, we can calculate the volume fraction of living cells by placing a light source under wells and removing the cells swimming on the surface. Figure 2.9b, shows that healthy cells concentration increases during the first three days to reach the maximum value at the third day before starting to decrease.

---

<sup>1</sup><https://www.chlamycollection.org/>

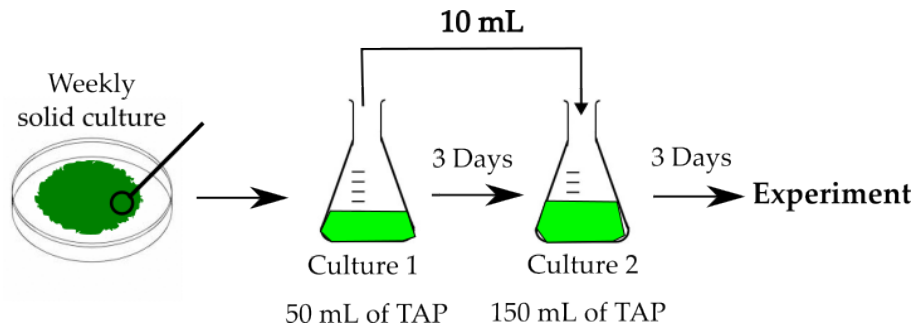


Figure 2.8: Schematic describing the cell culture procedure done weekly. First we have the solid form of the *Chlamydomonas Reinhardtii* spread in petri dish. This paste is harvested and diluted in 50 mL of TAP and left to grow for 3 days in the incubator in order to reach saturation. Then, 10 mL of this suspension is taken and diluted in 150 mL of TAP, and left to grow for 3 days in order to have a homogeneous suspension. It is on the third day where the suspension is ready for experiments.

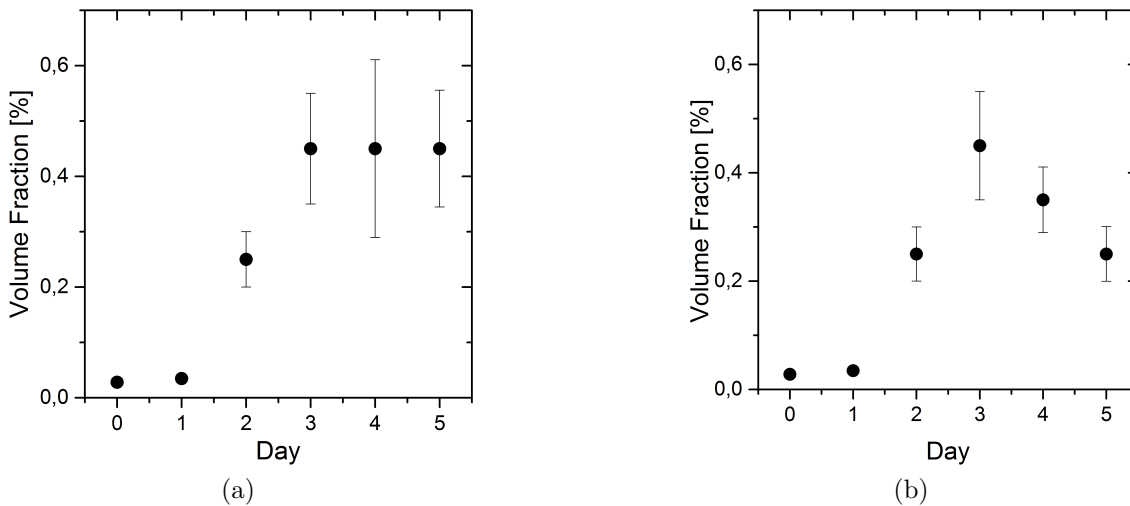


Figure 2.9: a. Graph showing the evolution of the biomass inside the suspension, where it reaches saturation on the third day indicating a deficiency of nutriment in the solution. A biomass contains both living and dead cells. b. Graph showing the evolution of living cell's volume fraction. It reaches its maximum value on the third day, then starts falling due to the absence of nutriment.

## 2.5.2 Response to Light

Until now, the behavior described in section 2.4a is in a purely random walk regime, where the CR swim without directional bias. However, we are interested in the photo-tactic response (*i.e.* the ability of the CR to respond to a presence of light). In general, when confronted to a light source, the CR exhibits two opposite behaviors, the first being attracted to the source or positive photo-taxis, the second, fleeing the light or negative photo-taxis. The later being a characteristic of our CC124 strain.

The bio-chemistry play behind this response is quite interesting. In their work, [Harris et al. \(2009\)](#) reported the role of the cation  $\text{Ca}^{2+}$ , released when the eye

perceives light. It results in one of the flagella being frozen, and as consequence the body rotates to a position parallel to the light direction Figure 2.10. One should also point out a very interesting phenomenon known as photo-shock. When exposed to high light intensities, the CR experiences a shock that results in a complete momentary stop, followed by a random swimming (Witman, 1993). We are particularly

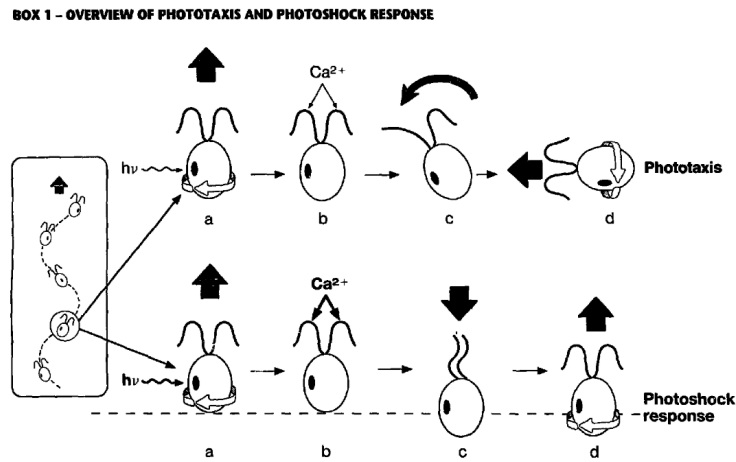


Figure 2.10: Schematic describing the stages of a CR response to light. First, when the eye of rhodopsin receives light, a bio-chemical reaction leads to a secretion of  $\text{Ca}^{2+}$  that leads to a freezing of one flagella while the other continue to beat resulting in a reorientation of the body in the direction parallel the source. The schematic also shows the photo-shock. (Witman, 1993)

interested in exploiting this property in order to create a directed crowd's motion toward a constriction. It is therefore important to study closely the photo-tactic behavior from a physicist point of view. To do so, we look at the response of the CR swimming in a capillary tube of  $0.2 \times 2 \text{ mm}^2$  to a white LED. We make sure that no external light source affects our measurements by inserting the capillary tube and the LED in a black box with two windows covered by red filters through which observation is made (CR do not perceive red light). We take our precautions one step further and conduct our experiments in a completely dark external environment. A reconstruction of trajectories under photo-tactic can be seen in Figure 2.11a, where the dominating motion is of a ballistic nature and the CR swim parallel to the light direction of the LED. We can also follow the evolution of the average swimming velocity along the  $x$ -axis,  $\langle v_x \rangle = V_x$ , through out the experiment. Figure 2.11b clearly shows the two regimes. When the light is off, the value of  $V_x$  fluctuates around  $0 \text{ }\mu\text{m/s}$  describing a random walk behavior. Turning on the LED, causes a response from the CR and dictates a re-orientation of the body to a direction opposed to the light source. This reaction time is in the order of the second ( $t_r = 2 \text{ s}$ ), before reaching its maximum value around which it fluctuates.

A comparison of the polar representation of the distributions of the orientation angle  $\theta$  in Figure 2.12a shows that in absence of light stimulus, the CR adopts all directions in their swimming without any bias represented in a uniform distribution (a particularity of the diffusive regime), whereas when the light are on, their orien-

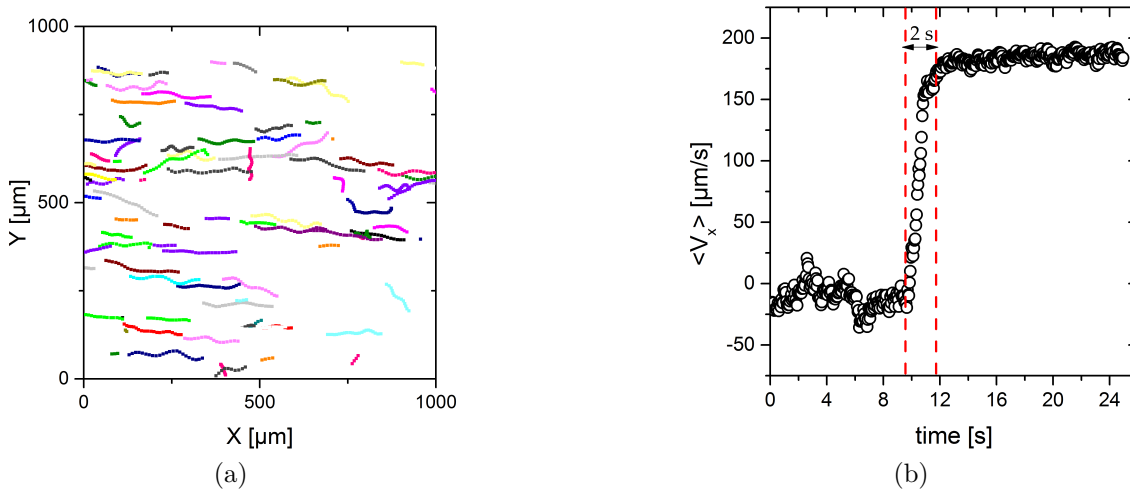


Figure 2.11: a. Reconstruction of particles trajectories during photo-tactic response. The general behavior is a ballistic motion fleeing the light (swimming from left to right) b. Values of  $V_x$  throughout the experiment. One can clearly see that before switching the light on, at  $t < 10$  s the value fluctuates at 0. When the light is turned on at the tenth second, the CR response is to reorient their body before swimming at full velocity in a direction opposite to the source. This reorientation time also known as the response time is in the order of the second,  $t_r = 2$  s

tation becomes biased and fluctuates around the value 0 as seen in Figure 2.12b. In the later case, the distribution of orientation  $\psi(\theta)$ , Figure 2.12c, can be fitted with a Lorentz function of type:

$$\psi(\theta) = \frac{\Gamma}{2\pi} \frac{1}{\frac{\Gamma^2}{4} + \theta^2} \quad (2.2)$$

With  $\Gamma = 0,57845$

### 2.5.3 Effect of viscosity on swimming velocity

Studying the effects of velocity variation on the efficiency of the evacuation is the core of our problematic. Hence we need to develop a reliable protocol that allows us to modify the swimming velocity of our CR without interfering with their biological mechanisms. To do so we opt to increase the viscosity of the medium. In fact, in their work, [Rafai et al. \(2010\)](#), showed the average swimming velocity varies linearly with the inverse of the viscosity. It means that the increase in viscosity leads to a decrease in swimming velocity. Interestingly this is done without altering the forces that the swimmer exerts on its surrounding, as we described previously in Chapter 1 section 1.3.

Increasing the viscosity is done by adding a polymer known as Dextran from *Leuconostoc mesenteroides*<sup>2</sup> with average molecular weight 9,000-11,000 and formula  $(C_6H_{10}O_5)_n$  supplied by *Sigma-Aldrich*. We use this specific type of Dextran for its

<sup>2</sup>We use this specific type because it is soluble in TAP. A Dextran from *Leuconostoc* spp caused solubility problems.

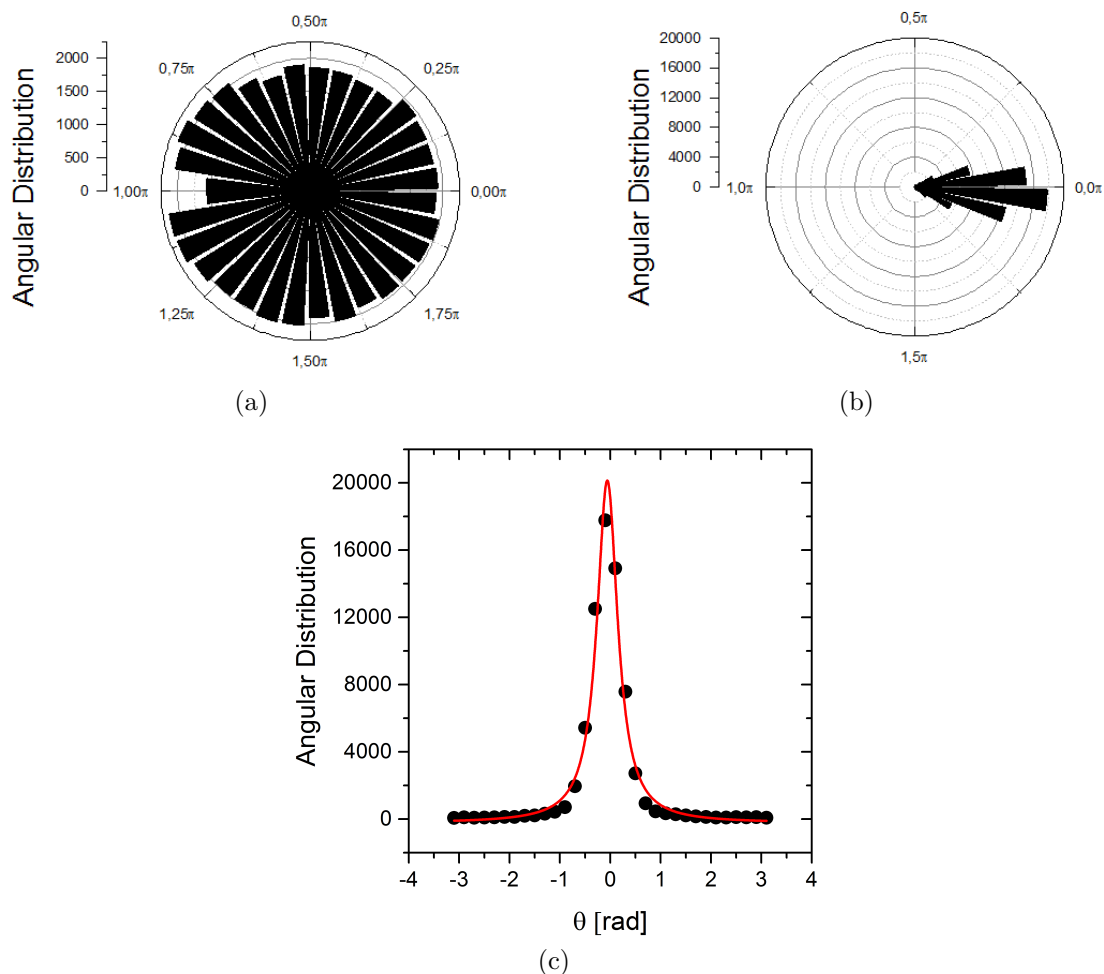


Figure 2.12: a. Polar form of angular distribution in the absence of any stimulus, the CR adopts all directions in its swimming a behavior typical of a diffusive regime. b. Polar form of the angular distribution when light is on, the swimming directions fluctuate around 0 indicating that the CR is fleeing the source in a direction parallel to the light direction. c. Histogram of angular distributions under light stimulus showing that it culminates around 0 and can be fitted with a Lorentz function 2.2.

high solubility. We prepare a solution of 20 %wt Dextran diluted in TAP, from which we take desired percentage and mix them with the suspensions to reach desired concentration of Dextran.

### In capillary tubes

First we would like to study the effect of adding Dextran on the swimming behavior *ex-situ*, through observing the behavior of CR in closed capillary tubes of  $0.2 \times 2 \text{ mm}^2$ . We use the same set up described in section 2.5.2. Figure 2.13 shows an average swimming velocity that decreases with increasing %wt of dextran (*i.e* the fluid viscosity). The maximum percentage of Dextran that we were able to reach is about 10 %wt, a threshold above which no motion is observable. As expected,



Dextran didn't affect the physiology of our cells nor their response to light. Another problematic concern is, that of confinement effect on the swimming.

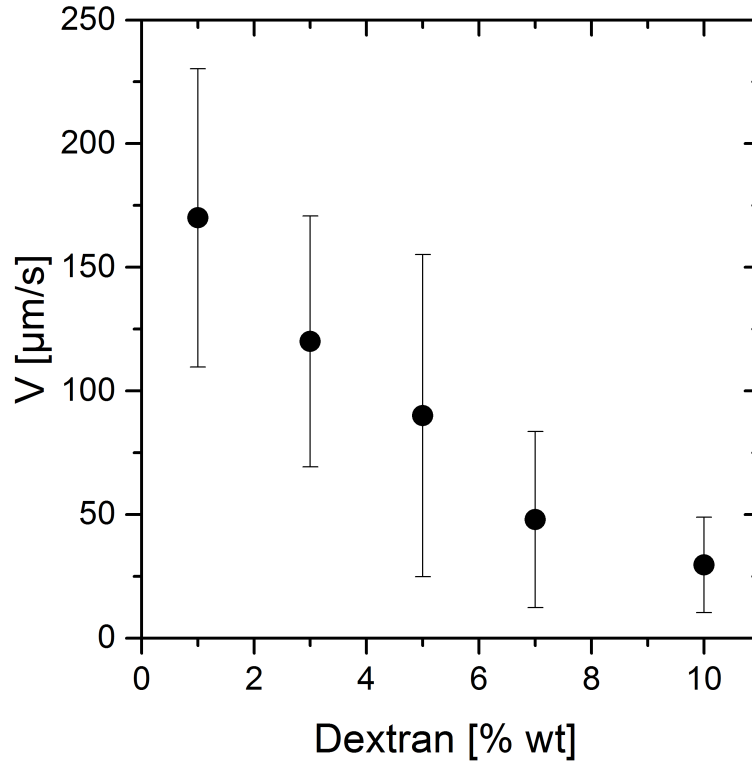


Figure 2.13: Effect of increasing viscosity through increasing Dextran concentration in the medium on swimming velocity in capillary tube. We can thus vary the value of the velocity in a range of  $[30, 50]$   $\mu\text{m/s}$

### In confinement or the *Hele-Shaw* effect

One of the advantages of using a micro-fluidic channel is the ability to confine our suspensions. As seen in section 2.1 while describing the microfabrication process, we aim to obtain a thickness of  $20 \mu\text{m}$ , we cannot but wonder if this extreme confinement has an effect on the swimming velocity in what we call an *in-situ* environment. Indeed, it is well known that confinement has an effect on a flow, as reported in Cohen et al. (2004). In his thesis, Brun-Cosme-Bruny (2019) dedicated a whole chapter to understanding the behavior of CR in confinement, and has reported that as the confinement gets more extreme, the swimming velocity decreases as shown in Figure 2.14.

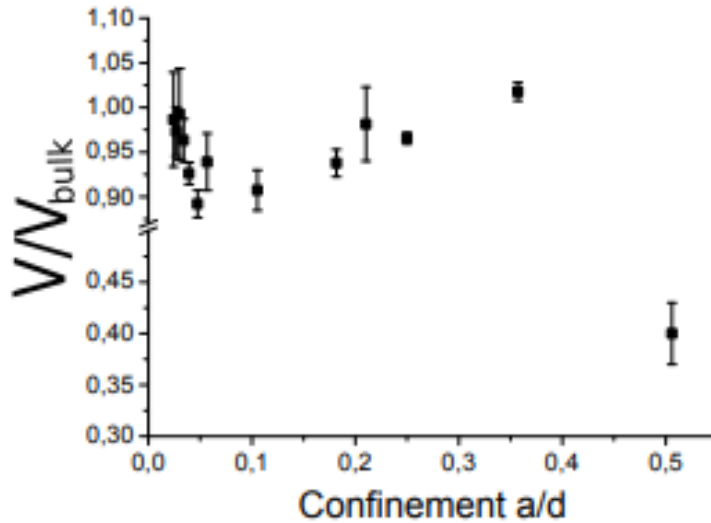


Figure 2.14: Confinement effect on swimming velocity as a function of  $a/d$  where  $a$  is the size of the CR and  $d$  is the height of the channel. The more thin a channel is, the slower is the velocity calculated. This graph shows that for a width of  $20\ \mu\text{m}$ , the average swimming velocity is expected to be slower than the one calculated in capillary tubes.  $a$  being the CR diameter and  $d$  the thickness of the channel. (Brun-Cosme-Bruny, 2019)

## 2.6 A typical Experiment

A typical experimental protocol consists first in preparing the PDMS channels and Dextran solution the night before, as well as a solution of 0.6 %wt Bovine-Serum-Albumin (BSA) dilute in TAP. The benefit of such solution is to reduce cell's adhesion to wall. On the day of the experiment, PDMS channels are attached to the microscopy glass via plasma-oxygen after drilling the inlet and outlet and being well cleaned to avoid any impurities from blocking the constriction. BSA is then deposited on one end leaving it to spread via capillary forces.

While waiting for the hydrophylic effect to wear off, we centrifuge four tubes of 40 mL each at 1000 rpm for 15 min, a reasonable spinning velocity that would not cause any harm for our cells. After it, the excess liquid is removed leaving with 1 mL of suspensions at a concentration  $\phi \sim 50 \times \phi_0$ . We leave it for 1 h under red light to give the suspension enough time to fully recover from the spinning and to reduce their sensibility to light in order to avoid any photo-shock. To this suspension we add TAP and Dextran in calculated amounts to get the desired Dextran's percentage in a total of 2.5 mL, before injecting it in the channel at a rate of 0.15 mL/min. After completion of the injection process, we close the channel hermetically and leave it for 15 min under red light for stabilization.

The circuit is then placed in the box under the microscope, see Figure 2.15. Camera's settings are adjusted to record at 20 frames per second for 40000 frames, enough to capture a whole experiment before the CR loses its photo-tactic ability. The white LED is aligned opposite to the constriction to impose a ballistic motion

directly towards it and to avoid any upward or downward motion. Recording starts when the LED is turned on, setting off the photo-tactic property of the *Chlamydomonas Reinhardtii*, leading to a build up at the door and a crowd formation, see Figure 2.16. Recording ends after the 40000 frames have been reached. The channel is then placed under red light for another 30 min for the CR to recover its photo-sensibility. Channels are used at maximum three times before hysteresis (i.e complete loss of photo-tactism) as we approach the beginning of the cells' night cycle.

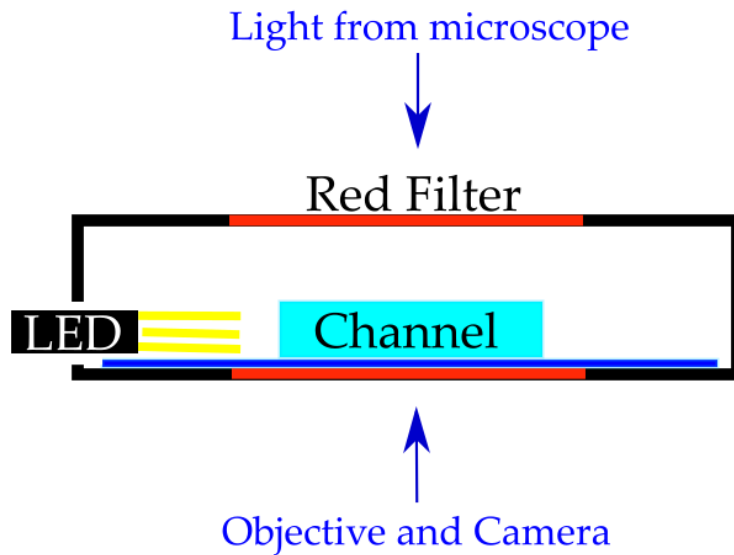


Figure 2.15: Schematic of the box through which observation is made without letting outside light source impact the CR behavior. Two red filters allow the passage of light for observation, a LED light inserted from the side is the only light source to which the CR reacts.

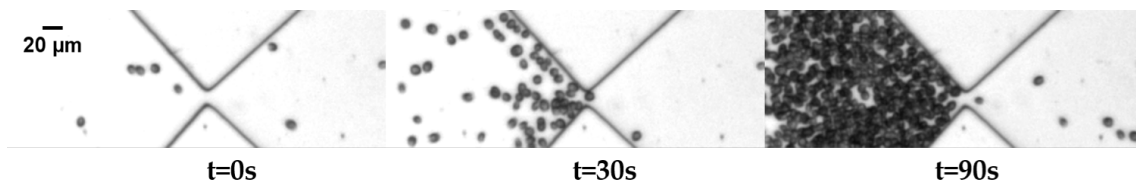


Figure 2.16: Snapshots of a typical experiment for  $D = 10 \mu\text{m}$  observed under the microscope. Black dots represent the *Chlamydomonas Reinhardtii*. Light source is at the left inducing a left-to-right motion. We can see the build up and crowd formation as the experiment goes on.

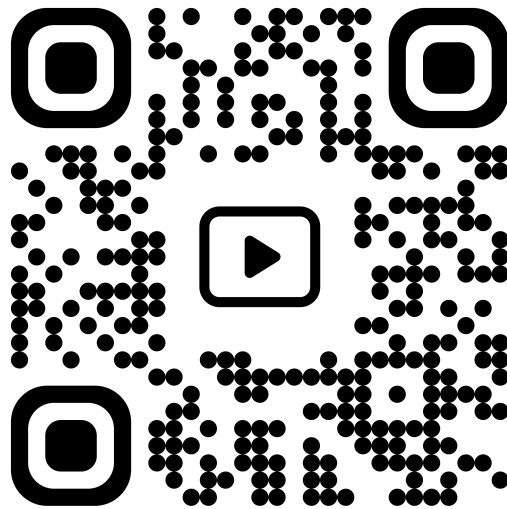


Figure 2.17: Scan in order to see an accelerated video of a typical experiment for  $D = 10 \mu\text{m}$  and  $V = 120\mu\text{m/s}$



## Statistical Tools to analyse Crowds of Microswimmers

*Nous pouvons regarder la mort en face ; mais sachant, comme  
quelques-uns d'entre nous le savent aujourd'hui, ce qu'est la vie  
humaine, qui pourrait sans frissonner (en supposant qu'il en fut  
averti) regarder en face l'heure de sa naissance?*

Thomas De Quincey (traduction de Beaudelaire) - *Confessions d'un  
mangeur d'opium anglais* - 1856

### Contents

---

<b>3.1 Velocity Calculation . . . . .</b>	<b>44</b>
<b>3.2 Crowd Formation . . . . .</b>	<b>45</b>
<b>3.3 Evacuation Statistics from the Waiting time perspective</b>	<b>46</b>
3.3.1 Cumulative Number of Escapees . . . . .	47
3.3.2 Time-lapse $\Delta t$ . . . . .	49
3.3.3 Dependent probabilities due to CR-CR interactions. . . . .	50
3.3.4 Survival function . . . . .	51
3.3.5 The Clauset-Shalizi-Newman fitting Method . . . . .	51
<b>3.4 Evacuation Statistics from the Avalanche Size perspective</b>	<b>53</b>
3.4.1 Avalanche size . . . . .	54
3.4.2 Jamming time . . . . .	54

---

In the same concept of presenting the methods we employ in our investigation, this chapter focuses on presenting the tools we use in our data analysis. We present the methods by which we scrutinize the validity of our experiments, the point at which the recording reveals valuable data, the position of the sampling window and the parameters which are valuable to our analysis.

### 3.1 Velocity Calculation

In Chapter 2 section 2.6 we laid out the details and steps involved in a typical experimental procedure. To analyze the recordings, first we look for any irregularities in the flow by studying the  $x$  – axis component of the velocity  $V_x$ . We are particularly interested in the presence of any counter flow that is due to some leak in our channel. Our study focuses mainly on the ballistic regime in two important zones. The first being away from the door in a diluted regime, the second being downstream far from the door as cells evacuate. The order of magnitude of  $V_x$  and its polarity, give us an insight on the validity of our experiment. We take a case study where  $D = 10 \mu\text{m}$  and a **Dextran’s percentage of 7%wt**. Figure 3.1 shows the distribution of the  $x$  component of the velocity upstream and downstream of the channel. The motion is indicated by an arrow and is from left to right, opposite to the light source. The positive value of  $V_x$ , with a Gaussian fit that peaks at around  $48 \mu\text{m/s}$  for both sides give us two important information. The first describes the behavior as purely ballistic with  $V_x = V$ , and that the behavior persists even after crossing the door, indicating a persistence in phototaxis. The second is the well-being of our cells given that they swim at the same velocity, meaning that the *squeezing* due to crowd’s formation did not have an impact on their physiology.

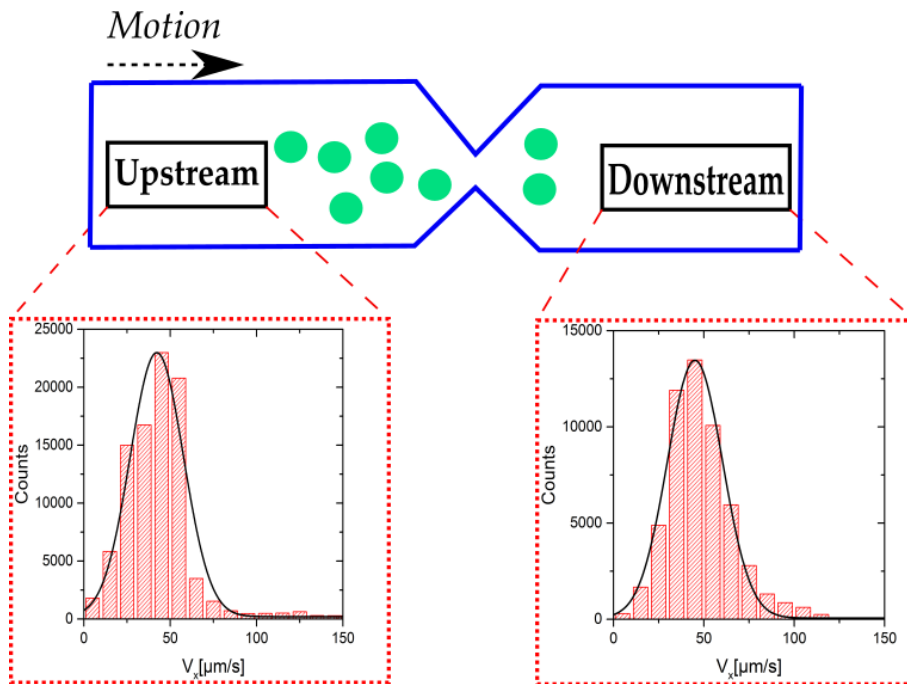


Figure 3.1: Schematic representing the distribution of the  $x$  component of the velocity for 7%wt Dextran. The motion is from left-to-right. The positive value of  $V_x$  indicates that the CR are traveling away from the light in a ballistic motion. The similarity of the behavior upstream and downstream shows that the phototactic response is not lost after crossing the constriction and light is still perceived. In a similar observation, an equal peak at  $48 \mu\text{m/s}$  at both sides indicates the wellness of our cells, increasing the accuracy of our results and proving that no bias exists due to any biological defect caused by crossing the door.

We repeat the procedure for experimental campaigns with different  $D$  and different Dextran's percentage. We focus our attention on the average swimming velocity. As explained in Chapter 2 section 2.3, we calculate the velocity by taking the peak value of the histogram of velocity distribution of all the particles in the diluted regime far from the door. Figure 3.2 shows the effect of the viscosity on the swimming velocity, as  $V$  decreases with increasing viscosity.

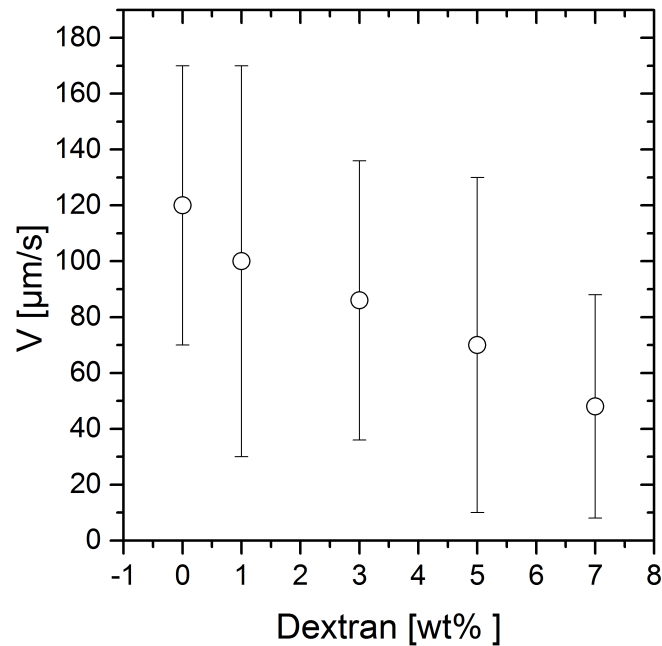


Figure 3.2: Velocity variation inside the channel for different Dextran percentages. The velocity is calculated upstream far from wall or crowd interference. Error bars represent the distribution inside the population (*i.e* the width of the histogram)

## 3.2 Crowd Formation

We remain interested in the upstream section of our channel, however we move our analysis closer to the door. To accurately quantify the efficiency of the evacuation, we must wait for a stable build up of CR to form at the door, *i.e* we must wait for a crowd formation, that is to avoid any bias induced from density variation. In a typical experiment we can identify three main phases of crowd buildup. The first is defined as the transition phase, where cells start to build up and is characterized by the steep increase in volume fraction that we see in Figure 3.3a. The duration of this phase is of about 100 s. We would like to study the effect of door width on this build-up time  $\Delta t_{build}$ . When we fix  $V$  and vary  $D$ , we notice, in Figure 3.3b, a much pronounced effect of  $D$  on  $\Delta t_{build}$ , where it varies from 100 s for  $D = 10 \mu\text{m}$  to 400 s for  $D = 67 \mu\text{m}$ . Now that we have uncovered the dynamics of the crowd's



build up as function of  $D$ , we can define the second phase, that of crowd stability, where the volume fraction remains stable at a high value of  $\phi \sim 55\%$ . It is in this window where our analysis takes place. The final phase is characterized by a dispersion where the CR go into photo-shock and lose their phototactic behavior thus recovering the random walk motion. The dispersion phase occurs outside the recording window, for exposure time that lasts  $\sim 40$  min.

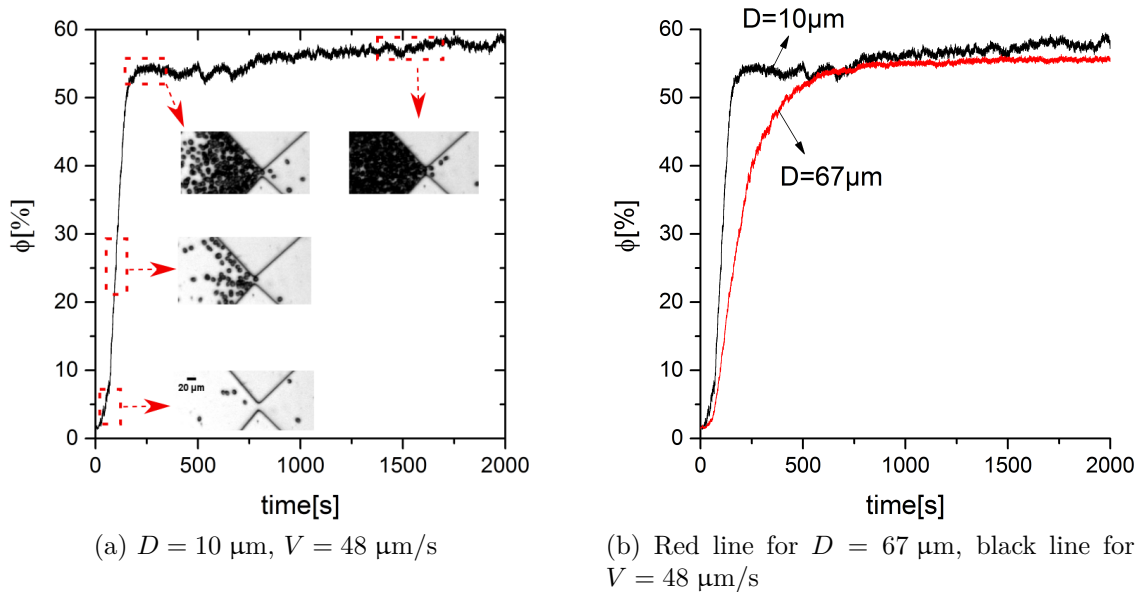


Figure 3.3: a. Evolution of the volume fraction at the entry of the door through out the experiment, with the corresponding snapshots showing the build up that occurs as the CR travel toward the opening. b. Comparison of build up time for small and large door size. It is clear that, in compliance with reason, the larger the opening the more time it takes to build up.

### 3.3 Evacuation Statistics from the Waiting time perspective

We now focus on a case study of properties  $D = 10 \mu\text{m}$  and  $V = 120 \mu\text{m/s}$ . The approach described is applied to all the results shown later in Chapter 4. Until this point we only tackled the upstream part of our channel, where we have defined the swimming velocity and studied the crowd formation in order to define a window of analysis. We shifted our attention briefly to the far-downstream part in order to analyze the behavior of our cells, making sure that no anomaly occurred due to high density crowding, and the robustness of our experiment. We now focus completely on the downstream, very close to the door, where we can evaluate the efficiency of the evacuation for different set-ups based on two criteria: 1) The waiting time (or

as we will later define it as time-lapse), the main parameter of this section. 2) The avalanche size discussed thoroughly in Section 3.4.

But first, we would like to know the behavior of our cells when they are exiting the door. Two questions need to be answered: 1) Are they still phototactic? 2) What is their escaping velocity? A simple reconstruction of trajectories of the escaping CR in Figure 3.4a, shows a ballistic evacuation in a direction opposite to the light source, meaning that stimulus is still perceived and phototactic response is still valid. In addition, a histogram of the velocity distribution in an area of  $20 \times 40 \mu\text{m}^2$  close to the exit in Figure 3.4b, shows that CR escape at their initial velocity, with no acceleration phase, this observation supports the claim that the high density crowding does not alter the physiology of our cells that regain their initial swimming characteristics as soon as they are in a diluted regime once again.

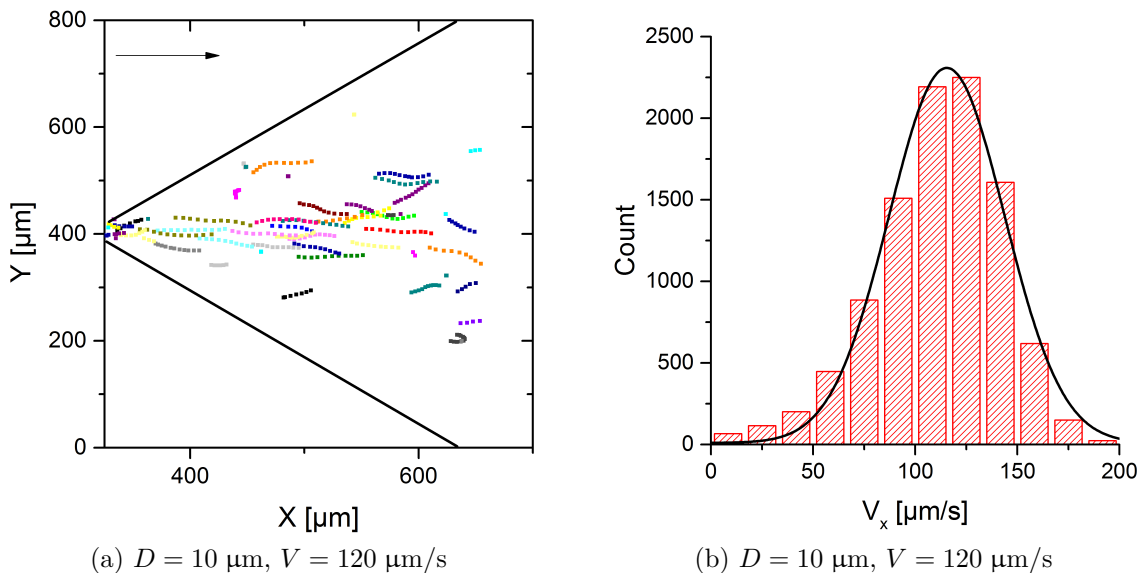


Figure 3.4: a. Trajectories of the evacuating cells, the motion is purely ballistic from left to right as indicated by the arrow, demonstrating a preserved phototactic response and a light perception even beyond the constriction. b. Distribution of values of  $V_x$  just at the exit, the positive values and the peak at  $120 \mu\text{m/s}$  come to support the ballistic nature and the intact physiology of the CR after being submitted to extreme density regimes. In addition it shows that CR evacuate with their initial velocity.

We set our observation window of height  $1.5 \times D$  and width  $1.375 \mu\text{m}$  at a distance  $30 \mu\text{m}$  from the door and perform tracking, Figure 3.5a. A narrow window is chosen in order to accurately measure waiting times between two consecutive evacuating CR, if one takes a bigger area, one risks to merge two evacuation events in one and bias the results.

### 3.3.1 Cumulative Number of Escapees

The first parameter to look at is the number of CR that escape through out the experiment, termed as the cumulative number of escapees, or cumulative for short.

Figure 3.5b shows the cumulative number of escapees throughout the experiment for  $D = 10 \mu\text{m}$  and  $V = 120 \mu\text{m/s}$ . The plot can give us two insightful information about the evacuation. The first is the *flux* that we denote by  $q$ .  $q$  gives us the number of particles that escape per second. By looking at this parameter we can judge the efficiency of the process. A higher  $q$  signifies a better evacuation. Graphically  $q$  is the slope of the linear fit of the cumulative curve; an in-depth study of  $q$  is discussed in Chapter 4, section 4.1.2. Another parameter that is essential for our analysis, is the time-lapse  $\Delta t$ .

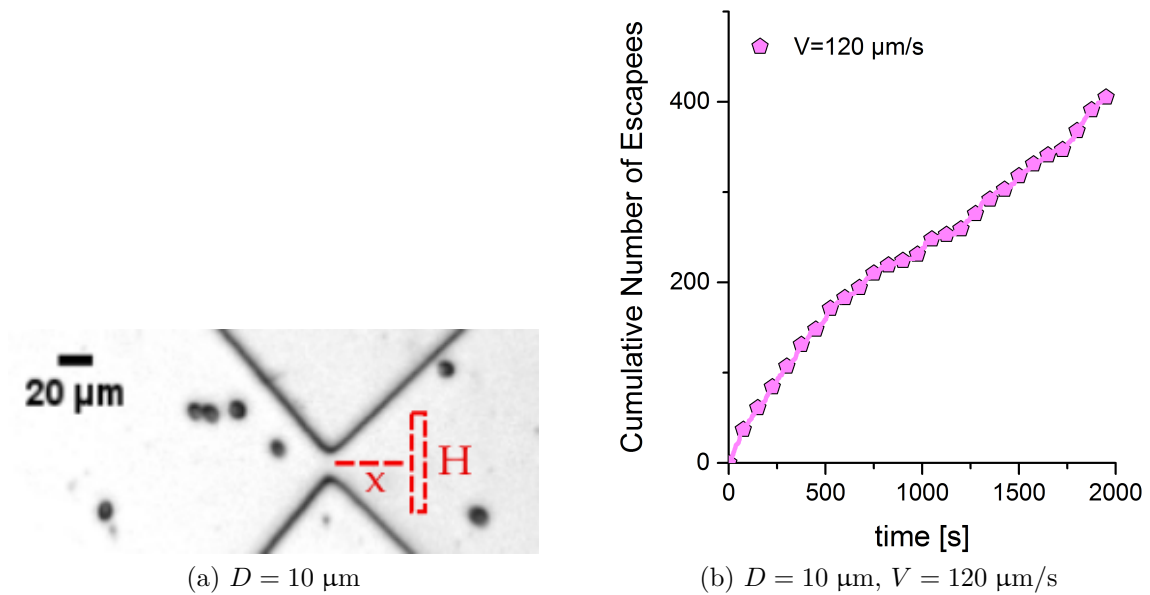


Figure 3.5: a. Zone of analysis just at the exit where  $x = 30 \mu\text{m}$  and  $H = 1.5 \times D$ .  
b. Cumulative Number of Escapees graph showing the number of particles passing through the analysis zone through out the experiment.

### 3.3.2 Time-lapse $\Delta t$

By definition, the time-lapse or waiting time  $\Delta t$  is the duration that elapses between two consecutive evacuations. A zoom in the cumulative number of escapees curve in Figure 3.6a, gives us an insight on how to extract this time. It is the length of *plateaus*, resulting from no passage of cells, that determines the value of  $\Delta t$ . The histogram of distribution of the time-lapses in a logarithmic scale plotted in Figure 3.6b, shows that the probability of easy passage with no jamming occurrence, decreases with increasing time-lapse  $\Delta t$ . We define the following probabilities:

$p = \beta\delta t \equiv$  the probability of a particle being evacuated during a time interval  $\delta t$ , with  $\beta = 1/\tau = \text{cte}$  independent of time, given the independent nature of events in this case. With  $\tau$  quantifying the average time of evacuation.

$q = 1 - \beta\delta t \equiv$  is consequently, the probability of a particle not to be evacuated during the time interval  $\delta t$  at whatever time  $t$ .

If we consider the probability  $q(\Delta t)$  of a particle not being evacuated during a time interval  $\Delta t$ . After an infinitesimal small time  $\delta t$ , the probability of not being evacuated over  $\Delta t + \delta t$  can be written :

$$\begin{aligned} q(\Delta t + \delta t) &= q(\Delta t) q(\delta t) \\ &= q(\Delta t)(1 - \beta\delta t) \\ \frac{q(\Delta t + \delta t) - q(\Delta t)}{q(\Delta t)} &= -\beta\delta t \\ \frac{dq}{q} &= -\beta\delta t \\ \ln q &= -\beta t + \text{cte} \\ q(\Delta t) &= e^{-\beta\Delta t}. \end{aligned}$$

The prefactor is 1 since for  $\Delta t = 0$ , we must have  $q(0) = 1$ . The final probability distribution :

$$\rho(\Delta t) = \left| \frac{dq}{d\Delta t} \right| = \beta e^{-\beta\Delta t},$$

We can deduce that the probability of evacuation in an uninterrupted scenario follows an exponential trend with an average evacuation time of  $\tau$ . We will study this case in details and extract the expression of  $\tau$  in Chapter 4.

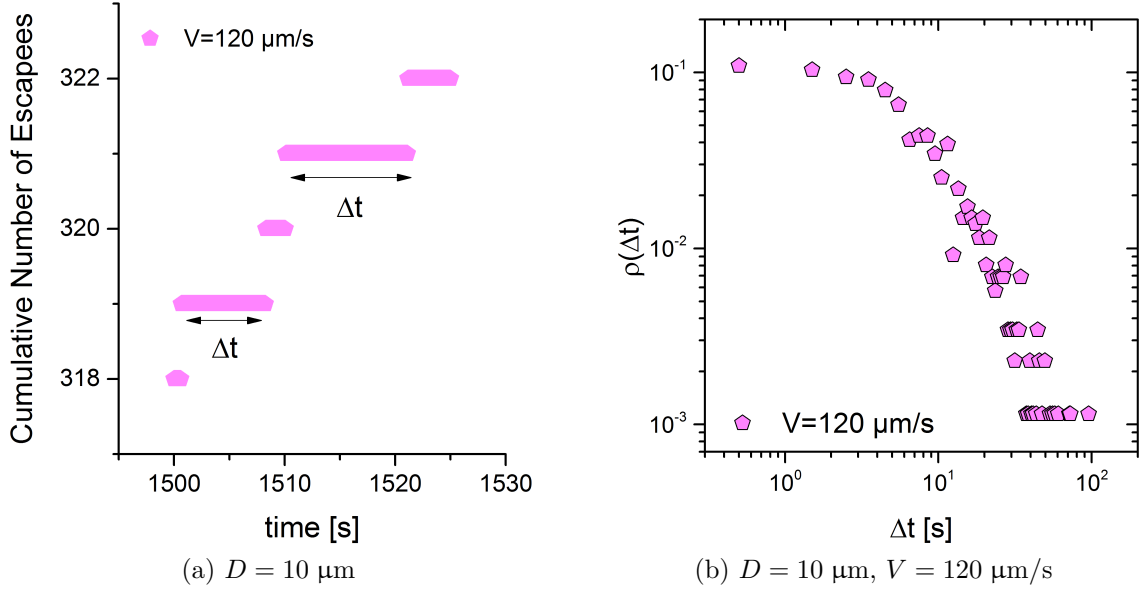


Figure 3.6: a. Zoom on the cumulative graph shows the *plateaus* where no CR is evacuating. The length of these *plateaus* corresponds to the waiting time or  $\Delta t$ , the bigger the length, the longer the  $\Delta t$ . Sparsely dots are just referring to the curve in Figure 3.5b. More data points are recorded. b. Histogram of the frequency of  $\Delta t$  (i.e *plateaus* showing a power law tail distribution;  $\rho(\Delta t) \sim \frac{1}{\Delta t^\alpha}$ : the bigger the waiting time, the less frequent its occurrence. However, the tail presents noise.

### 3.3.3 Dependent probabilities due to CR-CR interactions.

$p$  be the probability of a particle being evacuated during time interval  $\delta t$

$q = 1 - p$  is therefore the probability of a particle not being evacuated during the time interval  $\delta t$ .

Considering that the probability are dependent, we can write:

$$q(\Delta t + \delta t) = q(\Delta t) q(\delta t)|_{\Delta t},$$

where  $q(\delta t)|_{q(\Delta t)}$  is the probability  $q$  at time interval  $\delta t$  knowing that the probability  $q(\Delta t)$  is realized. We write  $q(\delta t)|_{\Delta t} = 1 - \gamma \frac{\delta t}{\Delta t}$  with  $\gamma \delta t < \Delta t$  admitting that the chance of a particle blocking the exit increases when  $\Delta t$  increases. Hence :

$$\begin{aligned} q(\Delta t + \delta t) &= q(\Delta t) \left(1 - \gamma \frac{\delta t}{\Delta t}\right) \\ \frac{dq}{q} &= -\gamma \frac{\delta t}{\Delta t} \\ \ln q &= -\gamma \ln \Delta t + \text{cte} \\ q(\Delta t) &= q_0 \frac{1}{\Delta t^\gamma}. \end{aligned}$$

The distribution is written as :

$$\rho(\Delta t) = \left| \frac{dq}{d\Delta t} \right| = q_0 \gamma \frac{1}{\Delta t^{\gamma+1}} = q_0 (\alpha - 1) \frac{1}{\Delta t^\alpha},$$

Here also, we see that  $P(t > \Delta t) = q(\Delta t)$  where  $\alpha$  quantifies the efficiency of the evacuation.

### 3.3.4 Survival function

Due to the highly scattered tail of the distribution (Figure 3.6b), it is preferable to use the cumulative complementary distribution function (CCDF for short) known also as the survival function, with:

$$P(t > \Delta t) = \left| \int_{\Delta t}^{\infty} \rho(t) dt \right|$$

As argued in the literature presented in Chapter 1, crowd's evacuation is characterized by  $P(t > \Delta t)$  which has a power law tail decreasing with the exponent  $\alpha$ , it appears that the evacuation of active suspensions of CR are no exception. Plotting the survival function in Figure 3.7 in the logarithmic scale, we can see the power law tail for big waiting time  $\Delta t$ . One reads the graph as follows: the higher the waiting time  $\Delta t$  the less probable it occurs during the experiment. We now understand how to describe the scenario where the CR are blocking the door and the evacuation is interrupted.

### 3.3.5 The Clauset-Shalizi-Newman fitting Method

To identify whether the CCDF of our data has a tail that follows a power law or another trend we use the library `powerlaw` implemented in python ([Alstott et al.](#),

2014). Mathematically, a given quantity  $x$ , in our case  $x$  represents time-lapses  $\Delta t$ , follows a power law if it is drawn from a probability distribution:

$$p(x) \sim x^{-A} \quad (3.1)$$

where  $A$  is a constant parameter of the distribution.  $A$  can be referred to as the *exponent* or *scaling parameter*.

It is rare to find a practice empirical phenomena that obeys a power law for all values of  $x$ . Hence, we should expect in the distribution of our  $\Delta t$  that the power law is applicable only for values greater than a minimum  $\Delta t_{min}$ . We can say that the *tail* of the distribution follows a power law, this insight will be of great help when looking physical quantities to describe the state of our system in Chapter 4.

The question of how to recognize a power law trend when we see one, is not straightforward, in fact we can rarely be certain that the quantity we are observing follows a power law trend. The method we use in our analysis is drawn from the work of (Clauset et al., 2009). We can summarize the procedure in a recipe of three main steps:

1. First, the authors attempt to estimate the values of the parameters  $\Delta t_{min}$  and  $A$ . The case we are mostly interested in understanding and applying is the one where the value of the lower bound of the power law ( $\Delta t_{min}$ ) is unknown. Authors propose an approach for estimating the values of  $\Delta t_{min}$ . The fundamental idea behind this method is fairly simple and can be resumed as follows; first, the authors choose an arbitrary value of lower bound that makes the probability value of the data and the best-fit power law model as similar as possible. The *similarity* can be interpreted as the distance between the data points and the power law model points. One can quantify this distance by using the Kolmogrov-Smirnov (KS) statistic. The KS statistic is nothing but the maximum distance between the CCDF of the data and the fitted model. KS is expressed as follows:

$$D = \max_{\Delta t \geq \Delta t_{min}} |S(\Delta t) - M(\Delta t)| \quad (3.2)$$

Where  $S(\Delta t)$  is the CCDF with the experimental data points for  $\Delta t \geq \Delta t_{min}$  and  $M(\Delta t)$  is the power law model that fits best in that data region. We recall that our goal is to actually find the value of the lower bound where the power law tail starts in our data, this value corresponds to the value of  $\Delta t$  that minimizes  $D$  in Equation 3.2.

Having identified the method by which the CSN method determines the lower bound value of the power law tail, we can now determine the value of the parameter  $A$ . As one recalls from the literature, the value of this parameter is key in quantifying and describing the state of the system. The method of choice of the authors is the *method of maximum likelihood*. For a data that follows a power law tail for all values  $\Delta t > \Delta t_{min}$ , one can derive maximum

likelihood estimate or MLE of the parameter  $A$  in Equation 3.3:

$$A = 1 + n \left[ \sum_{i=1}^n \ln \frac{\Delta t_i}{\Delta t_{min}} \right]^{-1} \quad (3.3)$$

Where  $i = 1 \dots n$  are the observed values of  $\Delta t$  such as  $\Delta t \geq \Delta t_{min}$ .

2. Till now the tools described are only useful in fitting a power law to a data set and provide estimates to the parameter  $A$  and  $\Delta t_{min}$ . We have not yet got the information of whether the power law is a plausible fit for our data or not. The authors attempt to answer the question by using the *goodness of fit test*. This test generates a  $p$ -value quantifying the plausibility of the hypothesis. This type of test is based on measuring the "distance" between the actual data set measured in the experiments and the hypothesis model. If one recalls, such distance can be quantifiable through the usage of the KS statistics described in the previous point. Authors argue that for a value of  $p \leq 0.1$ , the hypothesis of a power law is ruled out.
3. The final step is to compare the power law with other hypothesis. To do so authors use the likelihood ratio test. Even though we now know whether the use of a power law fit is plausible or not, via the method described in the previous point, we are still missing a part of the analysis, that is even if the data are well fitted with a power law function, there is still a chance that another fitting function can be used. It is thus important to have a method that can compare two types of fits against one another (for example, a power law compared to an exponential). Authors use the likelihood ratio test that computes the likelihood of the data under two competing distributions. Reasonably, the one with higher likelihood is the better fit. It easier the calculate the logarithmic ratio  $R$  of the two likelihood, and look at the sign of  $R$ .

A typical fitting process consists in inserting the raw data of  $\Delta t$  in the algorithm and look at the output. A scenario where the power law hypothesis is accepted, consists of having a value pf  $p > 0.1$  and an  $R > 0$  in comparing the power law function with the exponential. The fit is shown in Figure 3.7.

### 3.4 Evacuation Statistics from the Avalanche Size perspective

Understanding the evacuation procedure from the waiting time perspective is sufficient in general to evaluate its efficiency but it is not deemed satisfactory. Another parameter we can look at is the number of CR that escape. This parameter is widely looked at in the literature and from it we can extract many properties such as the jamming probability and critical diameter as explained in details in Chapter 1. In the case of active suspension, and due to the novel nature of this study, we go beyond the waiting time and tackle the question of avalanche sizes.



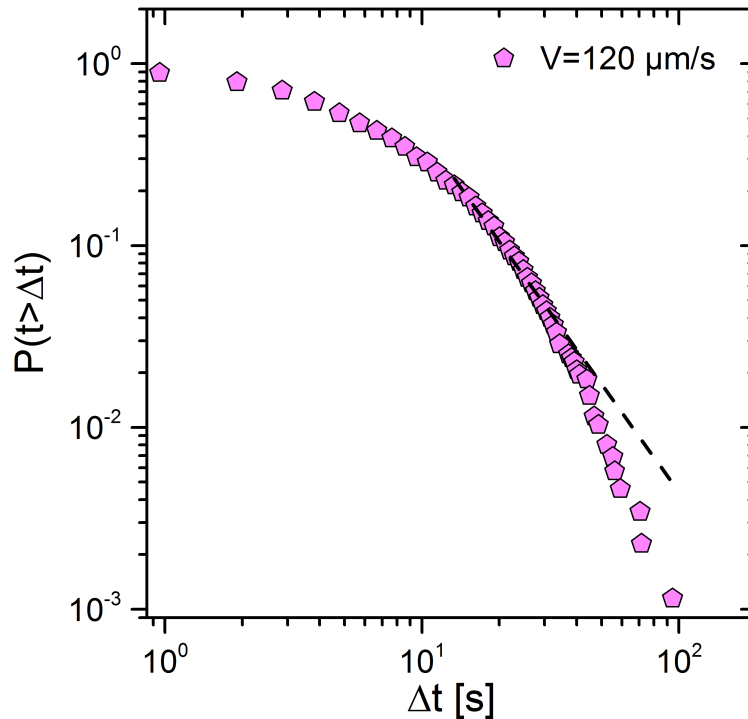


Figure 3.7: Survival function of the waiting times, the probability of finding large waiting time decreases. Dotted line represents the power law fit done by the described algorithm.

### 3.4.1 Avalanche size

During an evacuation, it is very common to notice *bursts*, meaning a group of particles that evacuate together once the door is momentarily unblocked. We define these *bursts* as avalanche and their size corresponds to the number of particles that are present inside them. We denote the avalanche size by  $s$ . Figure 3.8 is a spatio-temporal diagram of the sampling window for the first 100 s after crowd formation. We can see two clusters of CR (highlighted in green) separated by a blank space (highlighted in dashed blue). The number of CR inside the clusters represents the avalanche size, whereas the duration of the blank zone represents the waiting time. Graphically, we can extract this number by looking at the cumulative number of escapees plot. Following the definition, the avalanche size represents the number of CR counted between two *plateaus*. However, when attempting to extract the avalanche size from our data, we are immediately confronted with a problem, forcing us, once again, to introduce a new parameter.

### 3.4.2 Jamming time

Length of the *plateaus* in our cumulative number of escapees graph varies. In fact we can distinguish two regimes, the first being for short waiting times or small  $\Delta t$  the second being for longer waiting times or big  $\Delta t$ . Visually, Figure 3.8 the small waiting times are the blank spaces that exist between cells inside the avalanche.

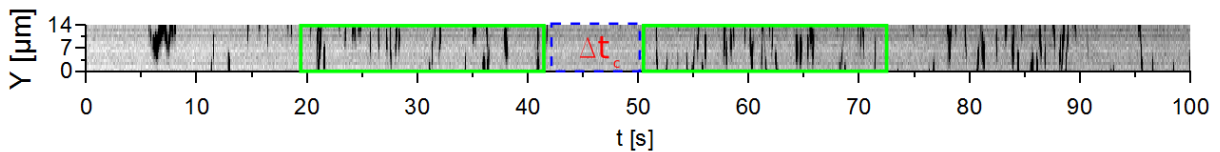


Figure 3.8: Spatio-temporal diagram of the evacuation, each black dot represents a CR evacuating. We can see the *bursts* highlighted in green separated by a blank space representing the waiting time or jamming time, followed by another burst. *plateaus* seen in the cumulative graph of Figure. 3.6a are representative of the blank space highlighted in dashed blue.

Hence, we should be careful with regard to what is the minimum length of *plateaus* we can consider as waiting time  $\Delta t_c$ , above which the system is in a jammed state. A schematic in Figure 3.9a describes the difficulty faced when trying to determine  $s$ . Being able to accurately define  $\Delta t_c$  have been a challenge in crowd studies. To avoid the arbitrariness involved in choosing the value of  $\Delta t_c$ , many solutions are reported in the literature. For instance, when looking at herd of sheep passing through a bottleneck in (Garcimartín et al., 2015), the typical time scale proposed is proportional to the length of the animal  $l$ , divided by their velocity  $v$  times how many sheep can exit through the door shoulder to shoulder (or the door-to-length ratio)  $\Delta t_c = \frac{l}{v \times D}$ . Another method to find the desired time is to calculate the mean flow rate within the avalanche, as explained in (Garcimartín et al., 2015) and repeated by (Yu et al., 2021), the avalanche size is divided by the avalanche duration for all the avalanches. The weighted average is then calculated. The values of the mean flow rate converges to a constant value for  $\Delta t > \Delta t_c$ . A more simplistic yet accurate approach exists and uses the output of the CSN fitting method described in section 3.3.5 above. We have seen in the recipe given by the authors, that one of the requirements is to get the value of  $t_{min}$  above which the trend becomes a power law distribution. Therefore it is acceptable to take the value of  $\Delta t_{min}$  given by the algorithm as the minimum waiting time above which the system is considered jammed. It is this method that is used in our analysis. Figure 3.9b shows the histogram of avalanche size distributions for our case study. We notice that the probability decreases as the avalanche size increases. It is important to note that the main difficulty of this study is due to the fact that we do not observe any permanent jamming of the door. In the literature we can find experiments where finding  $\Delta t_c$  is not a problem since the particles block opening indefinitely until a user intervention to unblock the system, a process mainly seen in granular system such as those studied in (Zuriguel et al., 2005) and (Janda et al., 2008).

Having described in details the experimental methods and the process of analyzing the data, we can now present the results.

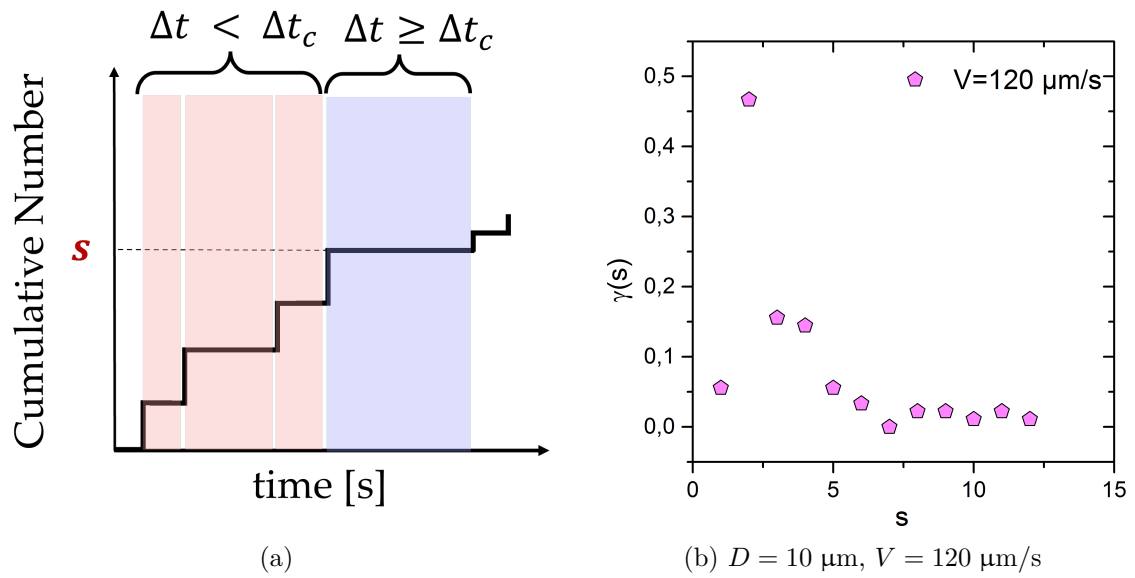


Figure 3.9: a. Schematic describing the method by which we identify avalanche size by distinguishing two categories of  $\Delta t$ , the first being smaller than the critical waiting time, the second being equal to or bigger then  $\Delta t_c$ . b. Probability distribution of avalanche sizes in our case study, showing a low probability for big sizes, which is normal given the fact that  $D = 10 \mu\text{m} \sim a$ .

## Jamming transition, the $D$ - $V$ phase diagram

*Nous ne pensons presque point au présent, et si nous y pensons, ce n'est que pour en prendre la lumière pour disposer de l'avenir. Le présent n'est jamais notre fin. Le passé et le présent sont nos moyens, le seul avenir est notre fin. Ainsi nous ne vivons jamais, mais nous espérons de vivre, et nous disposant toujours à être heureux, il est inévitable que nous ne le soyons jamais.*

Blaise Pascal - *Pensées* - 1670

### Contents

---

<b>4.1</b>	<b>Reference Case <math>D = 67 \mu\text{m}</math></b>	<b>58</b>
4.1.1	Cumulative Number of Escapees	58
4.1.2	Stokes Time rescaling	59
4.1.3	Survival Function	61
<b>4.2</b>	<b>Extreme Case <math>D = 10 \mu\text{m}</math></b>	<b>62</b>
4.2.1	Cumulative Number of Escapees	62
4.2.2	Survival Function	63
4.2.3	Coefficient $\alpha$	65
<b>4.3</b>	<b>D-<math>V</math> phase diagram</b>	<b>66</b>
4.3.1	Avalanche size & Critical Diameter $D_c$	66
4.3.2	Active Jamming probability	68
4.3.3	Location of Active Jamming transition	69
<b>4.4</b>	<b>Discussion and Conclusion</b>	<b>70</b>

---

Having presented in details the process by which we treat our experiments in order to get significant results, we can now proceed to find an answer to our problematic: Does active suspension behave similarly to other system in an evacuation scenario? Does the addition of hydrodynamic forces have any effect?

In this chapter we present experimental results of two different cases and discuss them so we can extract useful information on the state of our system. We focus on varying door width  $D$  and swimming velocity  $V$  with viscosity increase as discussed in Chapter 2, section 2.5.3. Results from a range of varying parameters allowed us to build a  $D$ - $V$  diagram pinpointing the location of the transition frontier where our system changes state. We end the chapter with a discussion of the results as well as a conclusion.

A nuance between the terms *Jammed* and *Clogged* needs to be clarified. In our description of the evacuation we prefer to use the term jammed, despite the expression clogged is dominant in literature. The reason behind this is that the evacuation in our system does not fully stop *i.e* reach a *clogged* state. Instead, the flow of CR exiting is momentarily halted (order of seconds) before resuming *i.e* *jamming*. We find it crucial to make the distinction between the terms, so the reader won't assume that our system is completely blocked.

**N.B:** Results of this Chapter are presented in the article: "Active jamming of microswimmers at a bottleneck constriction" by Edouardo Al Alam, Marvin Brun-Cosme-Bruny, Vincent Borne, et al. accepted for publication in **Physical Review Fluids** on 14 September 2022, published on 26 September 2022 (see Annexe H)

## 4.1 Reference Case $D = 67 \mu\text{m}$

It is trivial to characterize first the evacuation process in a scenario where the door is large. We refer to this geometric set-up as the reference case. The door width is  $D = 67 \mu\text{m}$  almost seven time the diameter of a CR, meaning that at any given time seven particles can exit simultaneously. As per the protocol described, we wait for a crowd formation on the neck before starting our analysis. We fix the door width and vary the swimming velocity.

### 4.1.1 Cumulative Number of Escapees

The first parameter to look at is the cumulative number of escapees for different swimming velocities. We plot the results in Figure 4.1a. The first observation one can make is that the faster the CR swim, the higher is the total of cells that escaped through out the experiment. Indeed for a velocity of  $V = 120 \mu\text{m/s}$  a total of roughly 8500 particles escaped, whereas for the slowest swimming velocity, the total of CR that escaped is about 3000 for the same duration of the experiment. Almost  $\sim 3\times$  more particles escape when we triple the swimming velocity. As a result, one can say that the flux  $q$  increases with the velocity as more particles escape per time unit. A zoom at the cumulative graph for the highest velocity in Figure gives us an in depth look and clearly shows the absence of long plateaus, pointing to the absence of long waiting time, therefore no jamming is reported. The experiment

time is less than 2000 s due to the fact that the crowd needs longer time to form as explained in Chapter 3, section 3.2.

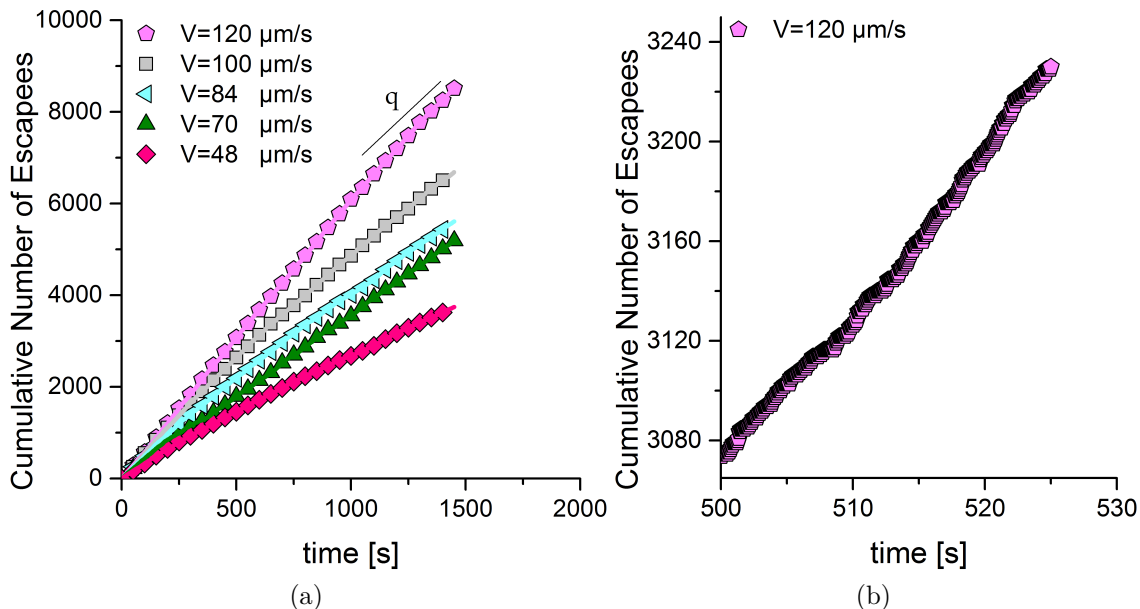


Figure 4.1: a. Cumulative Number of Escapees of CR through out the experiment for different swimming velocities. The higher the velocity, the greater the total number of particles escaping at the end of the recording. This behavior is proper to an uninterrupted evacuation process. b. A zoom of the curve corresponding to the highest swimming velocity. No long *plateaus* are observed, hence the absence of long waiting times and avalanches.

### 4.1.2 Stokes Time rescaling

The initial observation so far gives a clue to the nature of our evacuation process as continuous and uninterrupted. In Chapter 3, section 3.3.3, we have developed the expression of the survival function for a continuous evacuation and found that it exists an average evacuation time  $\tau$ . Our objective is to find the value of  $\tau$  and its relationship with the swimming velocity. On one hand, we start by looking at the flux  $q$ , by definition  $q$  is the number of particles per second, therefore we can deduce that the value of  $q^{-1}$  is nothing but the average time that separates two consecutive escaping particles. In Figure 4.2a we can see that  $q^{-1}$  is proportional to the inverse of the swimming velocity  $q \sim V$ . On the other hand, during a continuous evacuation scenario, were the particles follow each other one by one in a queue, the average time that separates these particles is usually related to the duration that a particle takes in order to cover a distance equal to its diameter, by definition this parameter is referred to as Stokes time, and has been used extensively in the literature, and is expressed as:

$$\tau = \frac{a}{V} \quad (4.1)$$

Where  $a$  is the particle diameter and  $V$  the swimming velocity. In an attempt to see if we can use the Stokes time described in Equation 4.1, we plot the evolution of  $q$  with the swimming velocity in Figure 4.2b and deduce that the value is constant for all  $V$ . We can conclude that the average time separating two consecutive evacuations for  $D = 67 \mu\text{m}$  is related to the swimming velocity via the Equation 4.1. Re-scaling

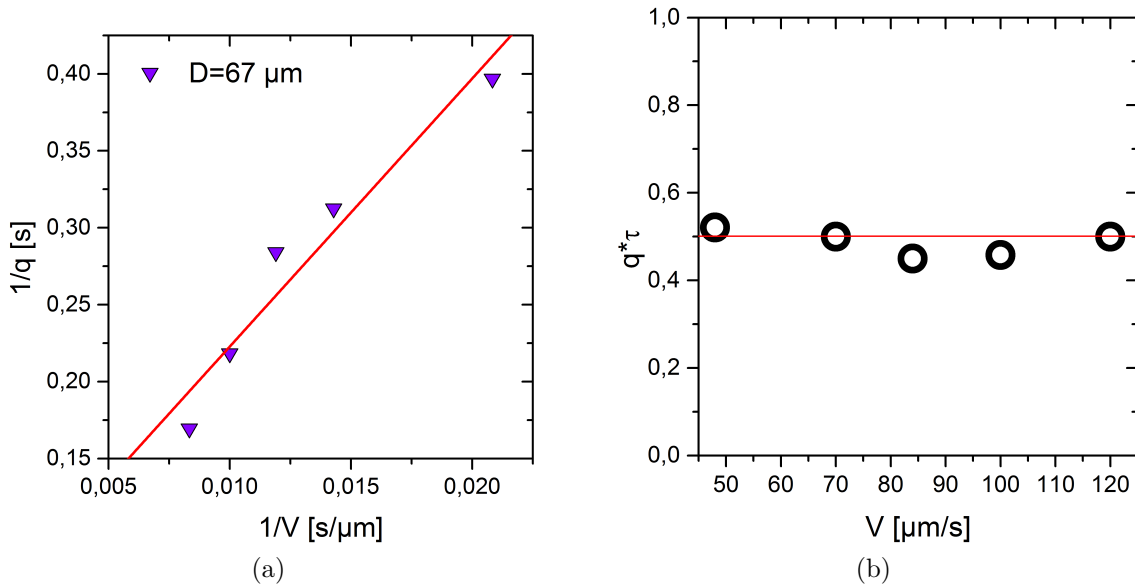


Figure 4.2: a. The linearity between the average duration between to consecutive evacuations  $q^{-1}$  and the inverse of the swimming velocity, the faster the CR swim the less they have to wait. b. Stokes time  $\tau$  as the average waiting time for a door opening of  $D = 67 \mu\text{m}$

the cumulative number of escapees, in Figure 4.3 with  $\tau$ , we obtain a collapse of the curves following a linear trend.

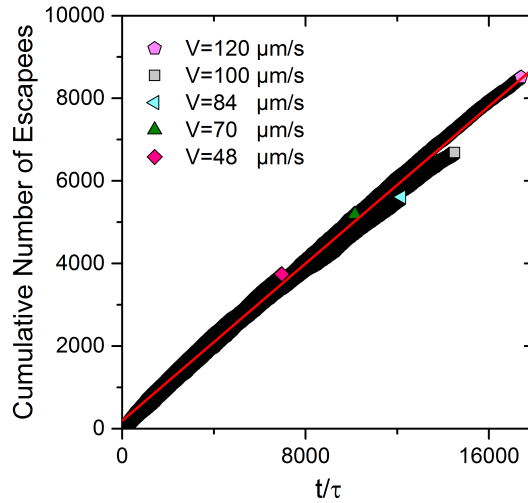


Figure 4.3: Re-scaling with Stoke time leads to a collapse of all the curves following a linear trend, this behavior is reminiscent of what we would expect in an uninterrupted evacuation scenario.

### 4.1.3 Survival Function

Following the re-scaling of the cumulative graph and the collapse of all the curves in a linear trend, a first phase of characterization is achieved. We now focus our study on the Survival Function, as stated previously, it is this quantity that determines the efficiency of the evacuation. The expression developed in Chapter 3, section 3.3.3 predicts a CCDF that decays following an exponential trend in a case of uninterrupted evacuation. We plot the survival function in Figure 4.4a for different swimming velocities in logarithmic scale, where the dominant exponential decay trend is clearly visible. When re-scaled by the Stoke time  $\tau$  in Figure 4.4b, the curves collapse following  $e^{-\frac{\Delta t}{\tau}}$ , meaning that for such a large door dimension, all velocities have the same probability of jamming the exit.



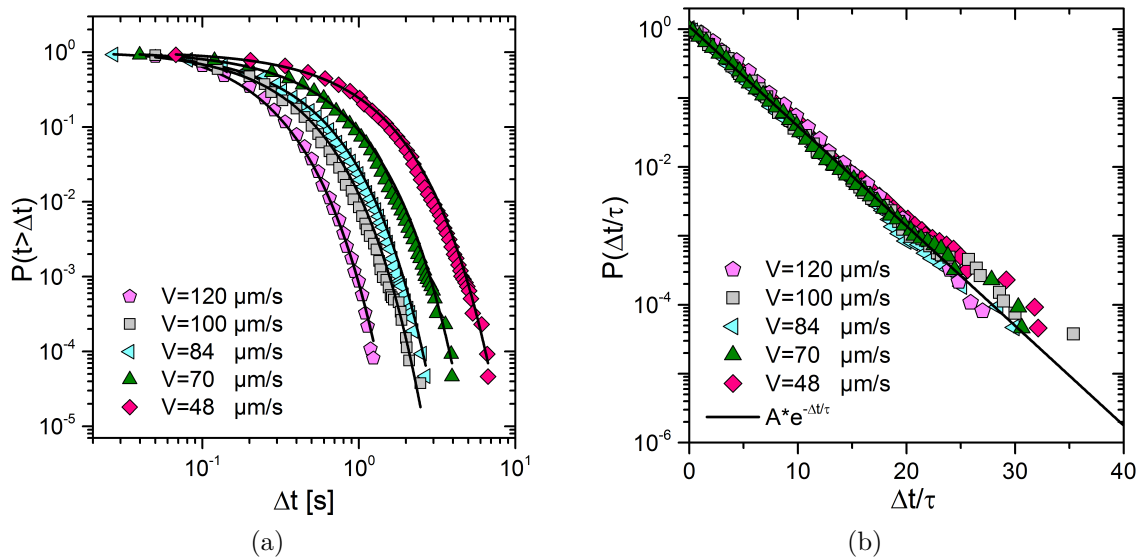


Figure 4.4: a. Survival function for different velocities, where the curves follow an exponential decay trend predicted via a simple probabilistic model for uninterrupted evacuation (see Chapter 3). The velocity influence on the evacuation is also shown. The faster the CR swim toward the door, the lesser is the waiting time. b. Rescaling by  $\tau$  leads to a collapse following  $\sim e^{-\frac{\Delta t}{\tau}}$  meaning all velocities have the same probability of blocking the exit of  $D = 67 \mu\text{m}$

## 4.2 Extreme Case $D = 10 \mu\text{m}$

Having characterized the reference case of uninterrupted evacuation, we shift our attention to an opposite scenario, always keeping  $D$  constant and change  $V$ , we fix the new door dimension to  $D = 10 \mu\text{m}$  which is roughly equal to the diameter  $a$  of a CR. A drastic decrease in the door size that leads to a faster build up on the exit, hence the density saturation is reached within seconds.

### 4.2.1 Cumulative Number of Escapees

As it has been established by now, the first parameter to look at is the total number of CR evacuated. This is done by looking at the cumulative number of escapees graph. Interestingly enough, Figure 4.5a shows a discrepancy with what we have in the previous section regarding a wide door opening. As a matter of fact, it is a complete opposite behavior, as the total number escaped for the lowest velocity is higher than the total number of escapees for the highest swimming velocity. One can say that the faster the CR swim toward the door, the less they evacuate. We also notice the loss of linearity due to the presence of long *plateaus* as a result of longer waiting times (Figure 4.5b). This loss in linearity is reflected in the relationship between the flux  $q$  and the swimming velocity, as  $q$  is now inversely proportional to the velocity squared Figure (4.5c). As a result the re-scaling with  $\tau$  fails and the curves don't collapse (Figure 4.6b). Hence we can conclude that we are in a scenario where the evacuation is interrupted.

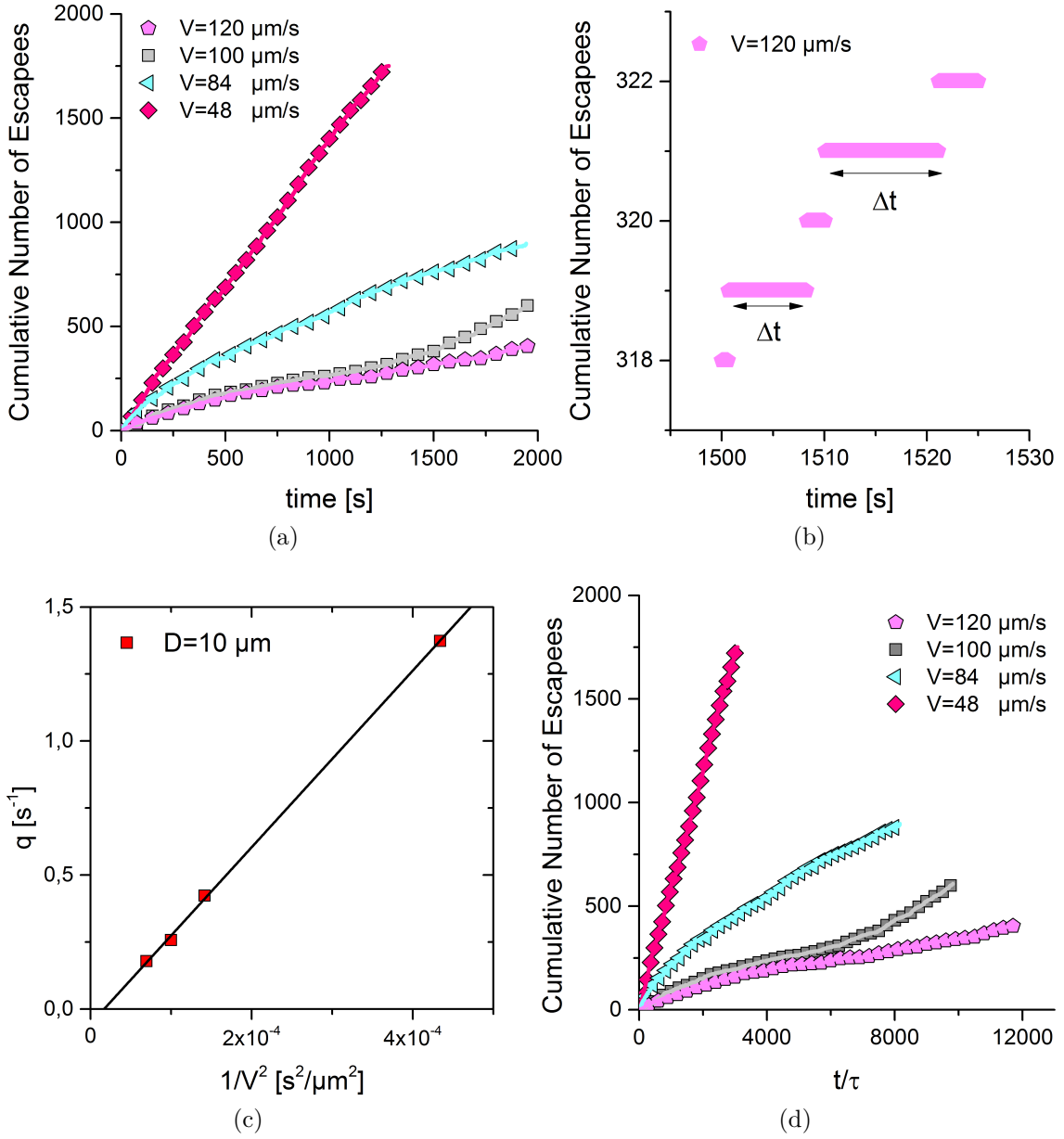


Figure 4.5: a. Cumulative number of escapees for  $D = 10 \mu\text{m}$  where more CR escape for slower velocities, a behavior that is opposite to the previous case. b. Zoom for  $V = 120 \mu\text{m/s}$  showing the existence of large *plateaus* due to a longer waiting time between two consecutive evacuations. Here  $\Delta t \sim 10 \text{ s}$ . c. The flux is proportional to the inverse of the velocity squared, hence the proportionality with the Stokes time is broken. d. Re-scaling with  $\tau$  verifies the broken proportionality mentioned earlier leading to a no collapse of the curves.

## 4.2.2 Survival Function

In Chapter 3, section 3.3.3 we have discussed the benefits of using the survival function to study the efficiency of the evacuation. We have also developed and predicted the expression that the survival function follows in the case of an interrupted flow

*i.e Jamming*, that is a power law tail that decreases following  $1 - \alpha$

$$P(t > \Delta t) = \left| \int_{\Delta t}^{\infty} \rho(t) dt \right| = \Delta t^{1-\alpha}$$

The CCDF plotted for different swimming velocities in Figure 4.6a manifest a rather interesting trend. The higher the velocity the higher is the probability of finding long waiting times, a behavior contrary to the one reported in a wide door geometry. The power law algorithm based on the CSN method confirms that the trend is in fact a power law tail. A re-scaling by Stoke time shows a deviation from the exponential trend for values of  $\Delta t > \tau$  (Figure 4.6b).

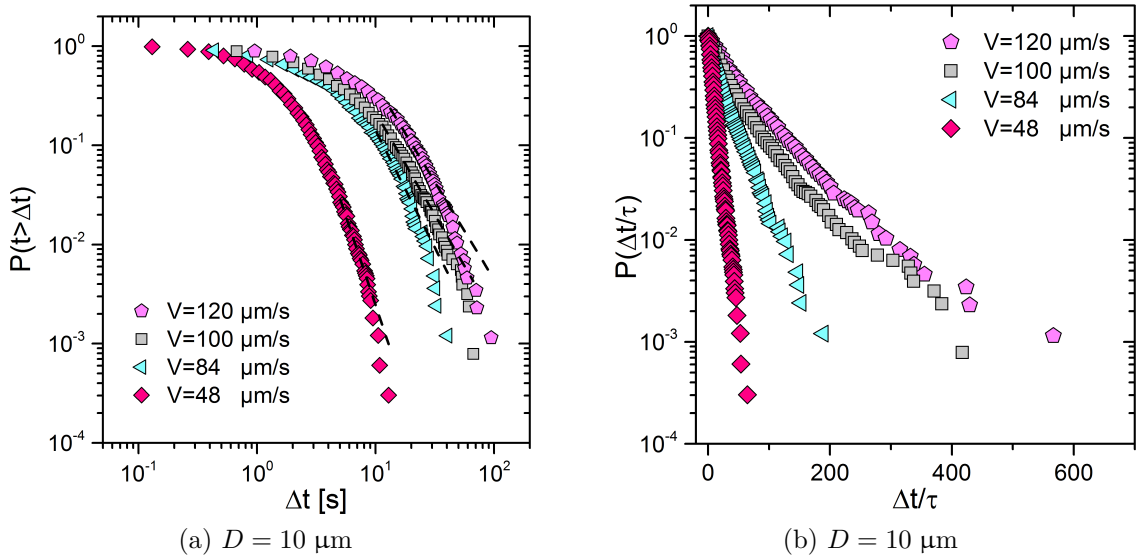


Figure 4.6: a. Logarithmic scale graph of the CCDF showing the effect of velocity on the waiting time. Dashed lines represent the fit of the power law function done via the CSN method. b. CCDF of re-scaled waiting values in semi logarithmic scale graph, the curves do not collapse, on the contrary they deviate from the exponential. The power law tail is seen for large values of  $\Delta t$ .

### 4.2.3 Coefficient $\alpha$

The two opposite cases that we reported in detailed previously show the effect of the swimming velocity on the evacuation process in different door width. For a big enough door, the evacuation is enhanced with increasing velocity, whereas the contrary behavior is observed when the width is drastically decreased. We do the same analysis for additional door width values of  $D = 20, 30, 50 \mu\text{m}$  with the same range of swimming velocities. As per the literature, we summarize our results by plotting the values of the parameter  $\alpha$  extracted from the  $1 - \alpha$  coefficient given by the CSN analysis. Since only regimes that are subjected to jamming follow a power law tail governed by the parameter  $\alpha$ , Figure 4.7 only shows the scenarios where jamming is present. One can make two interesting observations. The first being for a range of door width  $D \leq 30 \mu\text{m}$  where the value of  $\alpha$  decreases with increasing velocity, similar to the literature where the faster is slower effect is reported. Hence, one can conclude that in the range of velocities studied for value of  $D$  less or equal to  $30 \mu\text{m}$  the system experiences jamming. A second intriguing observation can be made for values of  $D \geq 50 \mu\text{m}$ . We already know that for  $D = 67 \mu\text{m}$  the evacuation is uninterrupted, hence its absence from the graph, however, for  $D = 50 \mu\text{m}$  we notice a shift of trend, where instead of decreasing,  $\alpha$  increases with  $V$  reflecting an evacuation that gets less jammed with higher velocities, till it reaches the value of  $120 \mu\text{m/s}$  where the state of the system shifts from jamming to flowing. Note that  $q$  is proportional to  $V^{-2}$ , which is not well understood yet.

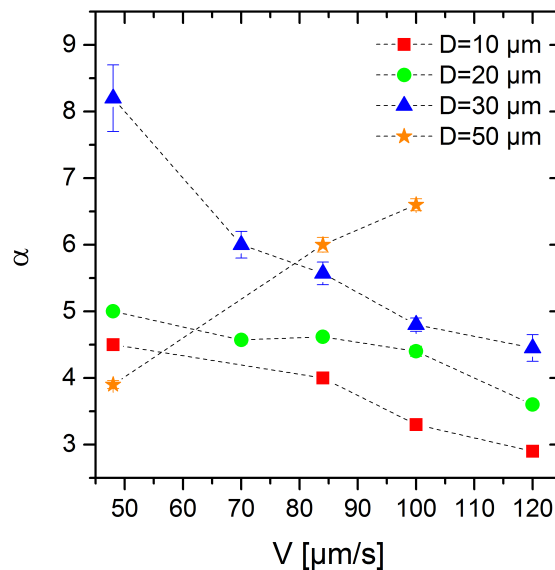


Figure 4.7: Evolution of the parameter  $\alpha$  for different configurations. Two distinct regimes are found. For  $D \leq 30 \mu\text{m}$ ,  $\alpha$  decreasing with increasing velocity depicting a system that is more prone to jam as the swimming velocity increases. A behavior reminiscent to what has been reported throughout the literature. The second regime is for  $D \geq 50 \mu\text{m}$ , where the opposite trend is reported, describing a system that is less susceptible to jamming as the velocity increases.

### 4.3 D-V phase diagram

When we looked at the evacuation from the time-lapse perspective, we looked at regime changes with velocity and door width variation. The evolution of the parameter  $\alpha$ , or the lack of it in an exponential case, gave us an insight on the pairing between velocity and door width that leads to a shift in the evacuation of our system from jamming to flowing. This shift is of great interest since it begs the question of the possible existence of a transition frontier dictated by critical values of door width. Hence our goal is to investigate the possibility of a critical door width  $D_c(V)$  above which the evacuation is continuous in order to build a  $D - V$  diagram. Phase diagrams as a mean to describe the transition in the system evacuation behavior is very common. In a recent study, (Caitano et al., 2021) reported the effect of orifice size and vibration intensity on the evacuation in granular systems. The authors characterize the vibration intensity with a dimensionless parameter  $S$ .  $S$  being the square root of the ratio between kinetic and potential energy:  $S = \frac{A\omega}{\sqrt{gl}}$  where  $l$  is the characteristic length and  $\omega = 2\pi f$  (Wassgren et al., 2002) (Eshuis et al., 2007).  $S_c$  is the critical value of  $S$  needed to break arch formation and therefore free the clogged system.  $S_c$  is highly dependent on the orifice diameter, the smaller the opening the higher the value of  $S_c$ , the data points delimit the boundary between the clogged and unclogged state in the  $S - D$  diagram in Figure 4.8a: above the boundary the system would be unclogged, whereas, below it, the system would be clogged, given the concave shape to the boundary. More recently, observing the behavior of pedestrians participating in the San Fermin Festival (Running of the Bulls) (Parisi et al., 2021) resulted in a state diagram describing the relationship between density and pedestrian velocity where three different regimes can be distinguished, see Figure 4.8b. The importance of phase diagrams in describing system's state during an evacuating crowd pushes us to attempt such study on our active suspensions.

#### 4.3.1 Avalanche size & Critical Diameter $D_c$

Every phase diagram needs a boundary or transition zone, therefore the first parameter to extract from our data is the critical diameter  $D_c$  for every velocity.  $D_c$  represents the value of a door opening big enough so that the system would never be jammed, and the evacuation process is uninterrupted. One way to determine this value is by looking at the avalanche size  $s$  ( $\langle s \rangle$  is the avalanche size averaged over the experiments). We have explained in details in Chapter 3, section 3.4 the definition of an avalanche size and the methodology to follow to determine its value. A relationship exists between the value of  $s$  and the opening size  $D$ , indeed if one meditates the question, one will come to the conclusion that for a big enough door size, for which the system is in a flowing regime,  $s$  corresponds to the final total number of particles that escaped during the experiment. To test the validity of this thought process for our case, we look at how the average number of avalanches evolve with  $D$  for different swimming velocity in Figure 4.9a. We can report several observations, first, for small values of  $D$  we notice that  $\langle s \rangle$  is small, meaning that few CR are able to escape before a new jamming event, hence more frequent jamming-flowing events. As  $D$  increases, the time window of CR escaping increases,

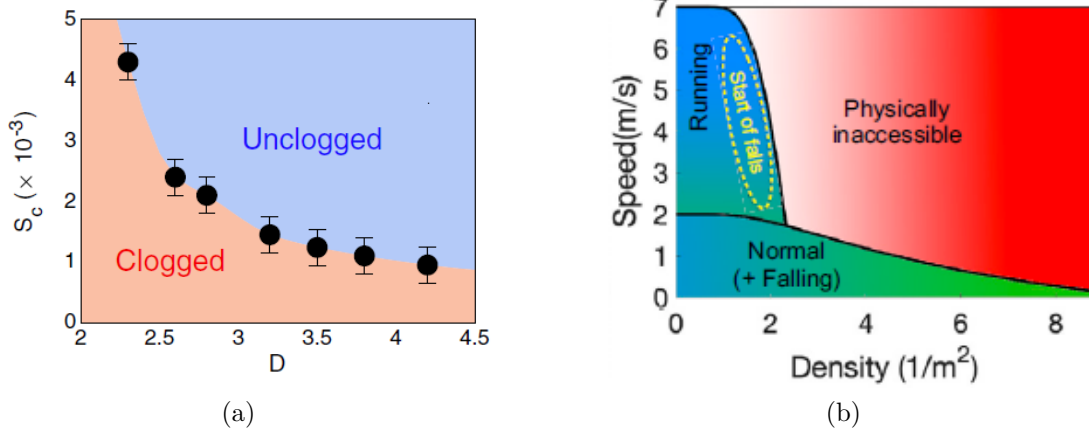


Figure 4.8: a. Granular clogging/unclogging:  $S_c$  for different opening sizes, delimiting the boundary between clogged and unclogged state in the  $S - D$  plane (Caitano et al., 2021). b. Pedestrians: Speed-Density state diagram with three distinguishable regions: 1) At low densities, a fleeing region in which pedestrians are able to change their velocities. 2) An inaccessible region for high density high velocities and 3) A normal region for pedestrians at low speed where the speed reduces with increasing density (Parisi et al., 2021).

leading to a gradual increase in  $\langle s \rangle$ .

When reading the graph in Figure 4.9a vertically; *i.e* fixing  $D$  and changing  $V$ , we can see the behavior reported previously and described in Figure 4.7. For values of  $D \leq 30 \mu\text{m}$ ,  $\langle s \rangle$  increases with decreasing velocity, meaning that the time intervals during which the system is flowing, increase. However, for  $D = 50 \mu\text{m}$ , the behavior is inverse. This interpretation comes to support the conclusion made when looking at the evacuation process from the waiting time point of view.

We focus on the  $V = 120 \mu\text{m/s}$  since for this value the system undergoes a transition from jamming to flowing regime with increasing  $D$ . Looking at the evolution of  $\langle s \rangle$  for this value of velocity with  $D$  allows us to extract an empirical relationship between the two parameters.  $\langle s \rangle$  increases as  $D$  increases till it reaches  $D = 50 \mu\text{m}$  where it diverges given the flowing state of the system. As a result, we can fit our curves with a power law divergence:

$$\langle s \rangle = \frac{C}{(D_c - D)^\beta} \quad (4.2)$$

where  $C$ ,  $D_c$  and  $\beta$  are fitting parameters.  $D_c$  is the critical diameter above which the evacuation becomes uninterrupted and the system is in the flowing state. Equation 4.2 describes well the behavior of the avalanche size: as  $D$  increases,  $\langle s \rangle$  increases, until we reach the critical value of  $D$ ,  $D_c$  where the system is flowing and  $\langle s \rangle$  diverges. Interestingly enough, this power law divergence have been seen in 3D granular hoppers (Zuriguel et al., 2005).

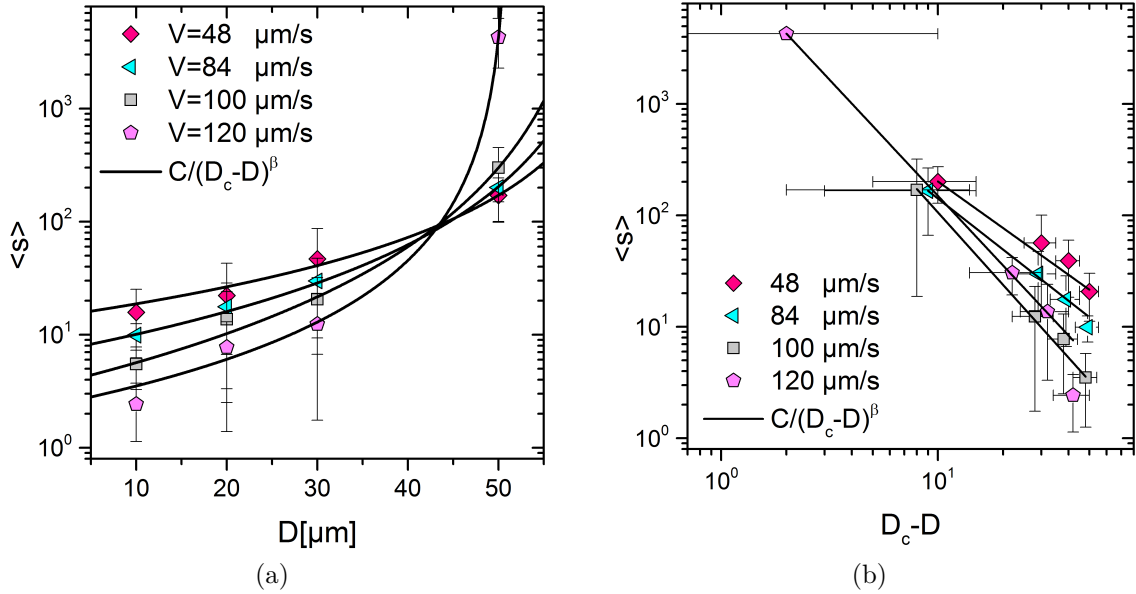


Figure 4.9: a. Avalanche size averaged over the experiments vs door size for different swimming velocity in the semi-logarithmic scale. Solid lines represent the fit done by Equation 4.2. b. Logarithmic scale plot showing showing the linearity of  $\langle s \rangle$  with  $D_c - D$ . Values of  $\beta$  and  $D_c$  are given in Annexe F

### 4.3.2 Active Jamming probability

Time-lapses and avalanche sizes are not the only properties used to characterize the state of the system. Another physical property is the Jamming probability. Knowing the value of this parameter help us understand better the state of our system. In granular system, blocking is due to visible arch formation. In an attempt to uncover the relationship between jamming events and arch formation, a probabilistic model is proposed linking the jamming probability with the orifice size (Janda et al., 2008).

Even though we do not observe any arch formation in our experiment, we extend the reasoning to our system. Let us quantify avalanche size  $s$  with  $\gamma(s)$  which is the probability of finding an avalanche of size  $s$ . By definition, an avalanche size consists of one jamming event and  $s$  non-jamming events. Therefore, we can write  $\gamma(s) = p^s(1 - p)$ . Here,  $p$  is the probability of a CR passing the door without cooperating with its neighbors to form a cluster and jam the door,  $J = 1 - p$  is therefore the probability of a CR ability to jam the exit. We assume that  $p$  is constant for all CR since in this simplified approach, we neglect the correlated nature of the jamming structures. Thus,  $p$  is a fitting parameter extracted from experimental data fitted with the above expression of  $\gamma$ , as in Figure 4.10a.  $p$ , and subsequently  $J$  are dependent on both the door size  $D$  and swimming velocity  $V$ , this dependency is portrayed in Figure 4.10b showing the evolution of  $J$  for different swimming velocities at different  $D$ , it manifests that the blocking probability decreases significantly with increasing  $D$ . This observations comes to support what we have seen so far regarding the effect of  $D$  and  $V$  on the system's state during an evacuation.

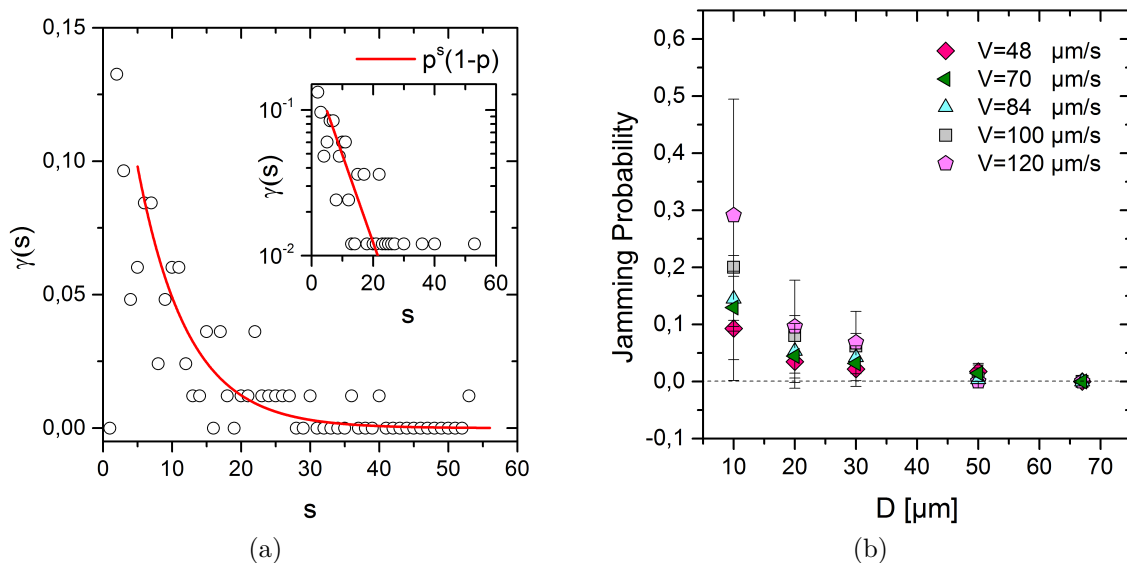


Figure 4.10: a. Histogram of  $\gamma(s)$ . Data correspond for  $D = 10 \mu\text{m}$  and  $V = 48 \mu\text{m/s}$ . Solid red line indicates the fit from which we extract the value of  $p$ . Inset: the same histogram in semi-logarithmic scale. b. Dependence of the jamming probability on  $D$  and  $V$ . We can see that for a system in a flowing state (*i.e.*  $D = 10 \mu\text{m}$ ),  $J = 0$  for all values of  $V$ .

### 4.3.3 Location of Active Jamming transition

We now have all the information needed to map out the Jamming phase diagram, that specifies whether our active suspension flows freely or is susceptible to jamming, as a function of door width and swimming velocity. Specifically, we follow section 4.3.1 in using Equation 4.2 to fit for critical diameter  $D_c$  at which the avalanche size diverges for a range of different swimming velocities. Figure 4.11 displays a field of data points where, for a given  $V, D$ , the value of the jamming probability is indicated by the color shading. A solid star indicates the extrapolated divergence at  $D_c$  found by fits to Equation 4.2. The  $D_c$  values serve as a separation of the  $V - D$  parameter space into two regions where jamming does and does not occur. Hollow circles ( $\circ$ ) represent experimental points where the system is jammed, whereas hollow triangles ( $\triangle$ ) represent the system in a flowing state. We notice as we move downward (*i.e.* decreasing  $D$ ) far from the  $D_c$  zone, the system becomes more susceptible to jamming, with  $J$  increasing with increasing  $V$ . As we get closer to  $D_c$ ,  $J$  decreases with  $V$ . Beyond the  $D_c$  belt, the system is in a fully flowing state with  $J = 0$  for all  $V$ .

Given the fact that we are dealing with active suspensions, one must keep in mind the biological constraints, as we can not get velocities less than  $48 \mu\text{m/s}$  since adding more Dextran will lead to a no-swimming effect. In addition, due to the confinement effect, velocities bigger than  $120 \mu\text{m/s}$  is physically impossible. Of course we are referring to average values of velocities. We also notice the transition decreases steeply, since the value of  $D_c$  is almost constant for small velocities, whereas it decreases rapidly for bigger values and, intuitively diverges. We can summarize the  $D - V$  diagram into three main regions:



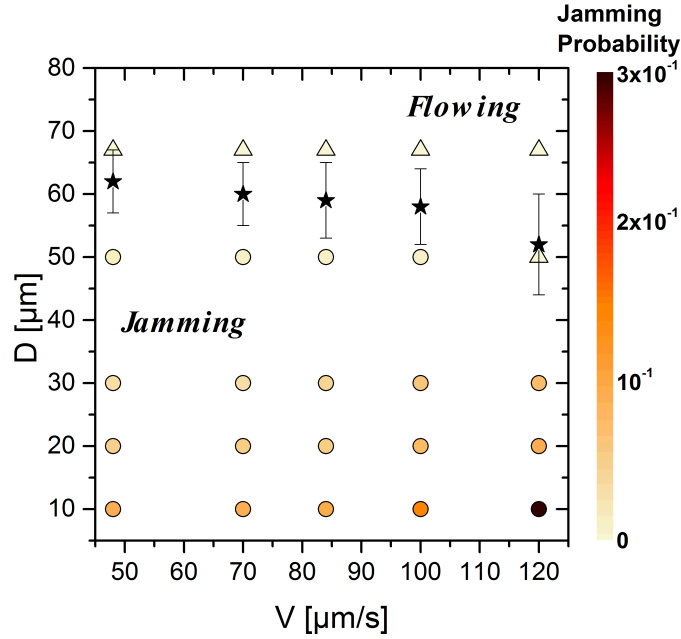


Figure 4.11: Active jamming phase  $D - V$ . For  $D < D_c$ , a power law behavior of the survival functions indicates jamming ( $\circ$ ). For  $D \geq D_c$ , a flowing regime is found ( $\triangle$ ) and well described by exponential survival function. Values of  $D_c$  ( $\star$ ) are given by Equation 4.2 with error bars being the fitting confidence intervals.

1. The first cluster consists of physically unattainable regions, mainly for very low and very high velocities due to biological and experimental constraints. It is indeed difficult to attain very small velocities as increasing viscosity leads to a no swim motion.
2. The second region consists of the zone below the  $D_c$  belt, where we see what resembles the faster is slower effect. Meaning the faster the CR swim the more susceptible the system is to jamming. Subsequently, this region is known as *Jamming*. The jamming probability decreases with increasing  $D$  as more particles can escape through a wider door, but increase with increasing  $V$ .
3. The third region consists of  $V, D$  values that are in the vicinity and go beyond the *criticality belt*, where the evacuation undergoes without any interruptions and the system is in its flowing state, with a jamming probability  $J = 0$ .

## 4.4 Discussion and Conclusion

We tackled the problematic of describing the evacuation process of active suspensions from two different point of views. First, we looked at time-lapses, and quantified the time that separates two consecutive evacuations. We detailed the thought process for two scenarios, for big door width  $D = 67 \mu\text{m}$  (case 1), which is almost the size of seven CR, and for small door diameter  $D = 10 \mu\text{m}$  (case 2) roughly the size of one CR, all while varying the swimming velocity. For case 1, we found that the different

CCDF follow an exponential decay trend and can be re-scaled with a parameter known as the Stokes time  $\tau$ , we found  $\tau$  to be proportional to the inverse of the flux. Case 1 describes a typical evacuation process where no jamming occurs, with an increase in  $V$  leading to an enhancement in evacuating. Case 2 is found to be the complete opposite case, where the CCDFs of time-lapses follow a power law tail, typical of jammed systems, with the system being more and more obstructed as  $V$  increases. A look at the parameter  $\alpha$  hinted to the possible presence of a transition zone for  $D = 50 \mu\text{m}$ .

We approached the study from a different angle, that of avalanche size to pin point the transition zone. Indeed, the evolution of  $\langle s \rangle$  with  $D$  for different  $V$  follows a power law that divergence for a critical value of  $D$ ,  $D_c$ . For  $D \geq D_c$  the system is in its *flowing* state. In addition, we calculated the jamming probability for each  $V - D$  pair, by applying probabilistic models used in granular systems to our case.

We were able to build a  $D - V$  diagram that shows the transition belt identified by the values of  $D_c$ . The state of system whether it is *flowing* or *jamming* is dependent on the position of experimental point relative to that *belt*.

To conclude, we are able to say that during an evacuation, when crowd is formed on the exit, active suspensions exhibit a similar behavior to what is called faster is slower in other types of crowds. Furthermore, the compatibility of probabilistic models taken from granular systems and applied to our case, hint to underlying similarities in jamming issues between the two systems. In the next Chapter we would like to investigate more the extent to which those two systems are similar.



## Effect of Geometry, an attempt to unravel the Jamming phenomenology

*L'éternel est écrit dans ce qui dure peu.*

Victor Hugo - *Je lisais. Que lisais-je?* - 1843.

### Contents

---

<b>5.1 Experimental set-up: varying the opening angle. . . . .</b>	<b>74</b>
<b>5.2 The exponential regime: <math>D = 75 \mu\text{m}</math> . . . . .</b>	<b>76</b>
<b>5.3 The reference case: <math>D = 40 \mu\text{m}</math> . . . . .</b>	<b>77</b>
5.3.1 Cumulative number of escapees . . . . .	77
5.3.2 Survival Function . . . . .	77
<b>5.4 The extreme case: <math>D = 10 \mu\text{m}</math> . . . . .</b>	<b>79</b>
5.4.1 Cumulative number of escapees . . . . .	79
5.4.2 Survival Function . . . . .	80
<b>5.5 Evolution of <math>\alpha</math> for all <math>D</math> and <math>\theta</math> values . . . . .</b>	<b>82</b>
<b>5.6 Avalanche size &amp; Critical diameter <math>D_c</math> . . . . .</b>	<b>83</b>
<b>5.7 Jamming probability . . . . .</b>	<b>84</b>
<b>5.8 <math>D - \theta</math> phase diagram . . . . .</b>	<b>85</b>
<b>5.9 Discussion . . . . .</b>	<b>87</b>

---

We have, up till this point, established a striking similarity between evacuation process in active suspensions and granular systems. Now we would like to know if the physical reasons behind this resemblance are the same. We have seen in the state of the art (Chapter 1) the causality of clogging might be due to arch formation

at the door, meaning that particles, via the friction forces, position themselves in an arch-like formation causing the clogging of the exit, it is only when this arching is broken that the system retakes the uninterrupted evacuation state. We have seen the attempts to facilitate the breaking of the arch, whether by increasing vibrations, or increasing driving velocity or just having a wider door, the later two resulted in similarities between active suspensions and granular, but this correlation does not necessarily mean causality. In order to investigate if the phenomenology behind the jamming is the same for both systems, we need to look at parameters that are directly related to arch formation, independent from physiological properties such as swimming velocity. Chapter 1, section 1.2.3 summarizes the most important work done so far regarding the opening angle in granular systems.

In this chapter we investigate the effect of one geometrical parameter closely related to arch formation, that is the opening angle  $\theta$ . We postulate, that if granular systems and active suspensions exhibit, once again, similarities in evacuation while varying this parameter, then there's a high probability that jamming in active suspensions is dictated by arch formation, even though they are invisible in our experiments. We start by introducing some modifications that we did to our experimental set-up, then proceed in the same process described in Chapter 3 to analyze our system.

## 5.1 Experimental set-up: varying the opening angle.

We are interested in looking at the effect of the opening angle variation on the evacuation process of our system, hence we proceed by keeping the velocity value fixed. We design circuits with varying angle size  $\theta$  and door width  $D$ . We keep the same definition of  $\theta$  present in literature for the sake of easy comparison, (Figure 5.1a).

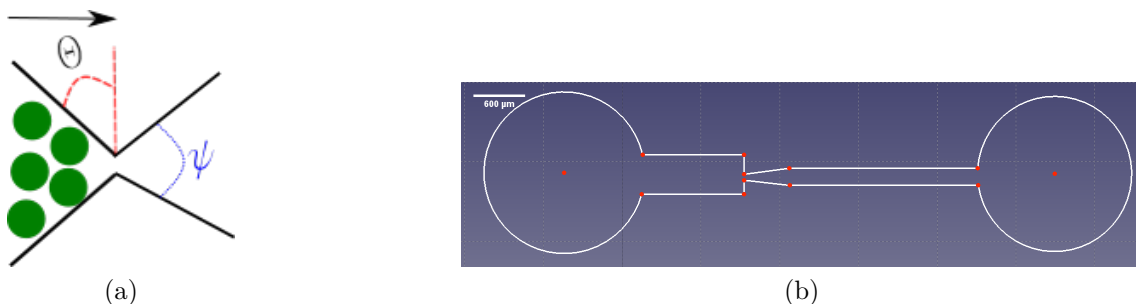


Figure 5.1: a. Schematic representing the channel and the angle  $\theta$  that the wall of the channel forms with the vertical axis.  $\psi$  is a fixed angle for all configurations. b. CAD drawing of the new design showing a more compact channel that will essentially lead to a faster concentration and a stable build up on the door.

We are directly faced with an experimental issue for the angle value  $\theta = 0^\circ$ , and with the same channel dimensions, crowd formation is not consistent, mainly due to

the fact that the CR swim in a ballistic motion into the walls. To solve this problem and get a crowd formation for this value of  $\theta$ , we aim at reducing the overall size of our channel, making crowd formation faster. Figure 5.1b shows the dimensions of our new design.

Modifying the overall size of the channel reduces the dispersion of the suspension and enhance *crowding* close to the door. We want to know how fast does it take for a crowd to form, what is the final density at which the crowd stabilizes and do those parameters change with the angle  $\theta$ . To do so, we look at the evolution of the volume fraction averaged over an area of  $40 \times 40 \mu\text{m}^2$  close to the opening throughout the experiment. Figure 5.2a shows the evolution of the volume fraction  $\phi$  for  $\theta = 0^\circ$ . We notice crowd formation takes around 1000 s to stabilize at a value of  $\sim 35\%$ . Given that our analysis starts when the crowd is stable, a 1000 s waiting time is considered long and costly. To reduce this gap, we have to increase the initial density in the channels so the crowd takes less time to form. To do so we increase the concentration of the suspension before injecting. After centrifugation and the removal of supernatant we use the inherent tendency of the CR to sediment to further remove the excessive layer of TAP after sedimentation. This allows us to obtain a highly concentrated suspension. Figure 5.2b shows the build up after concentration.

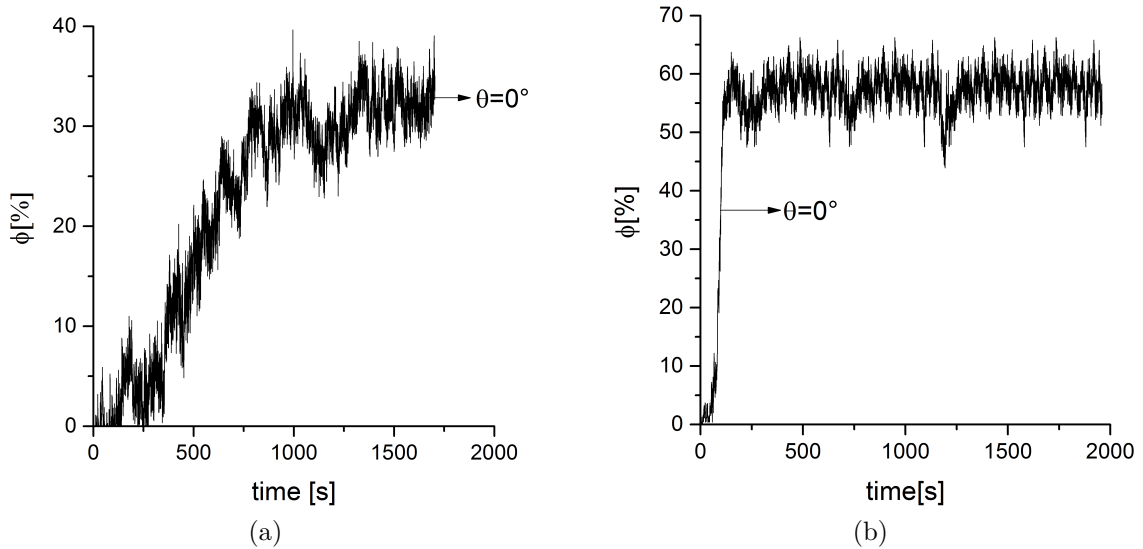


Figure 5.2: For  $D = 10 \mu\text{m}$  and  $\theta = 0^\circ$ : a. Volume fraction evolution for a non-concentrated suspension, we can see that crowd formation takes longer to be formed, and have a lower value of maximum value. b. The evolution of the volume fraction of the crowd as it forms throughout the experiment after increasing the initial concentration of the suspension. The difference in maximum value and time formation between the two scenarios is seen.

## 5.2 The exponential regime: $D = 75 \mu\text{m}$

In Chapter 4 we have seen that the evacuation through a wide door follows the "faster-is-faster" trend for all values of velocity. We would like to see the effect of the opening angle for such door configuration. We choose a wide door size of  $D = 75 \mu\text{m} \sim 7.5 \times a$ . As per protocol, we wait for a stable build up of the crowd on the door to start our investigation. No Dextran is added and the swimming velocity is  $V = 120 \mu\text{m/s}$  for all values of  $\theta$ .

We look at the cumulative number of escapees throughout the experiment. Figure 5.3a shows a collapse of the curves following a linear trend. This observation is reminiscent of Chapter 4, section 4.1.2. We have seen a collapse when the time is re-scaled by the Stokes time  $\tau = \frac{a}{V}$ . This behavior is proper for an exponential regime where the characteristic time is absent.

Looking at the CCDF of the time-lapses in Figure 5.3b, we see a collapse following an exponential trend  $P(t > \Delta t) \sim e^{-\Delta t}$  (the CSN method favors an exponential fit over a power law). This behavior, seen in Chapter 4 section 4.1.3, describes a system in a flowing state.

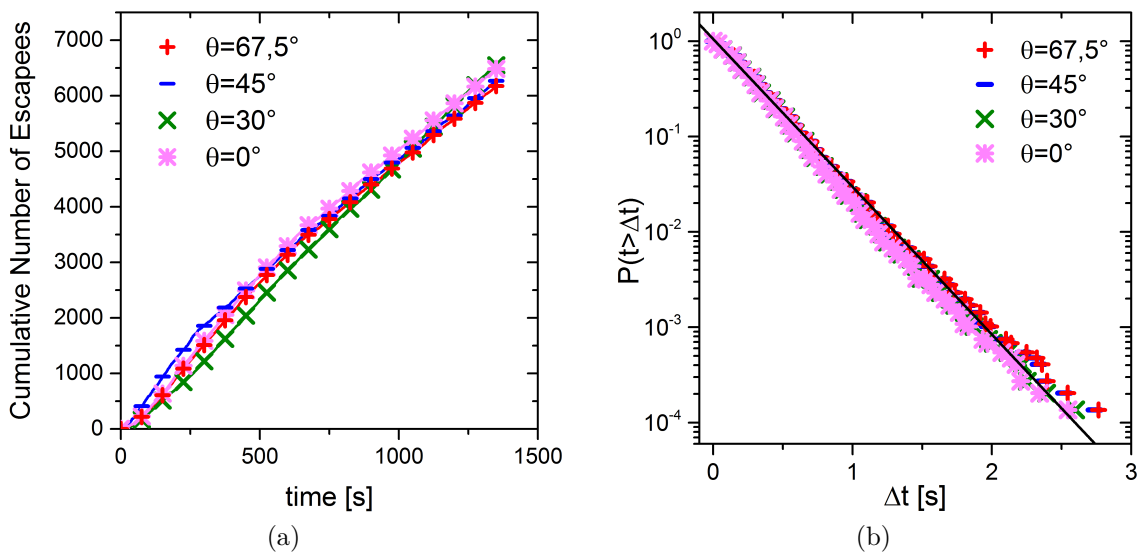


Figure 5.3: For  $D = 75 \mu\text{m}$  a. Cumulative number of escapees graph showing a collapse following a linear trend. b. The survival function showing the collapse. The graph is fitted by an exponential (black solid line) using the CSN method. Both observations point to an uninterpreted evacuation.

### 5.3 The reference case: $D = 40 \mu\text{m}$

For an adequate comparison with the literature, we study the case close to that reported in Yu et al. (2021), with a door width  $D = 40 \mu\text{m} \sim 4 \times a$ , where  $a$  is the diameter of one CR.

We look at the evolution of the volume fraction at the door in order to identify when a stable crowd is formed. Figure 5.4 shows the evolution of the volume fraction  $\phi$  for two angles. For a narrow configuration the build up stabilizes quicker than a flat-bottom channel.

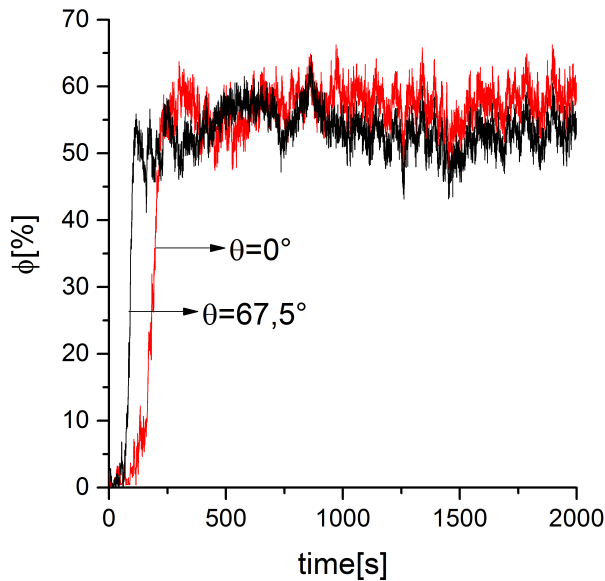


Figure 5.4: Evolution of the volume fraction for two different angles. For a narrow configuration (black) the build up and stabilization time is shorter than the flat-bottom configuration (red). However, in both geometries the crowd's volume fraction maximizes at  $\sim 55\%$

#### 5.3.1 Cumulative number of escapees

As per protocol described in Chapter 3, we first look at the cumulative number of escapees, the average swimming velocity is indeed checked and fixed at  $V = 120 \mu\text{m/s}$  shown in Figure 5.5. We observe that total number of CR that escaped throughout the experiment is higher for a flat-bottom channel than for a narrow one.

#### 5.3.2 Survival Function

Having looked at the cumulative number of escapees, we now focus our attention on the distribution of the time-lapses  $\Delta t$ . We plot the survival function of  $\Delta t$  for different angle values. A logarithmic plot on Figure 5.6a shows once again the dominant power law regime. We use the CSN method to best fit our curves and



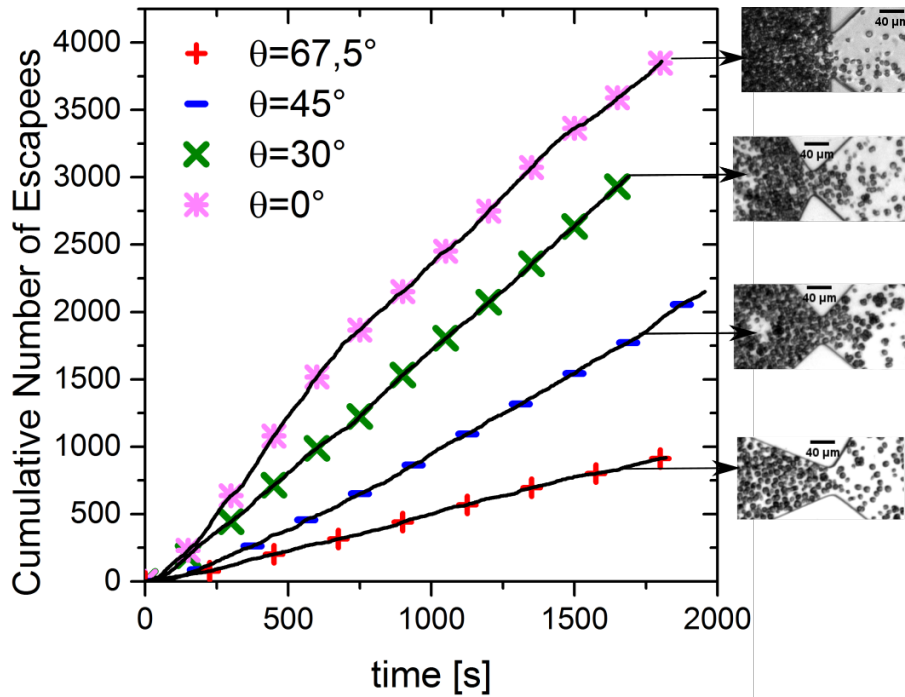


Figure 5.5:  $D = 40 \mu\text{m}$ : Cumulative number of escapes for different values of angle  $\theta$ . The total number of CR escaped for a flat bottom-channel is the highest, meaning that the evacuation is the easiest when the value of  $\theta$  is null and the geometry consists of a vertical wall. Whereas for a tighter geometry where  $\theta$  is the biggest, the evacuation appears to be jammed leading to a much more lower total number of CR escaping.

extract the values of the parameter  $\alpha$ . As we have established by now, a steeper tail defines a bigger value of  $\alpha$ , as we see for the flat-bottom case, subsequently it points out to the low probability of having long  $\Delta t$ , and as a result a more fluid evacuation. However, and as  $\theta$  increases, the probability to find bigger waiting times increases, meaning the system is prone to jam as the channel approaches a tube-like shape. Re-scaling with the Stokes time  $\tau = \frac{a}{V}$ , (Figure 5.6b), shows no drastic changes in the curves since  $V$  and  $a$  are the same for all the cases. A semi-logarithmic graph shows the divergence of the CCDF from the exponential (solid line).

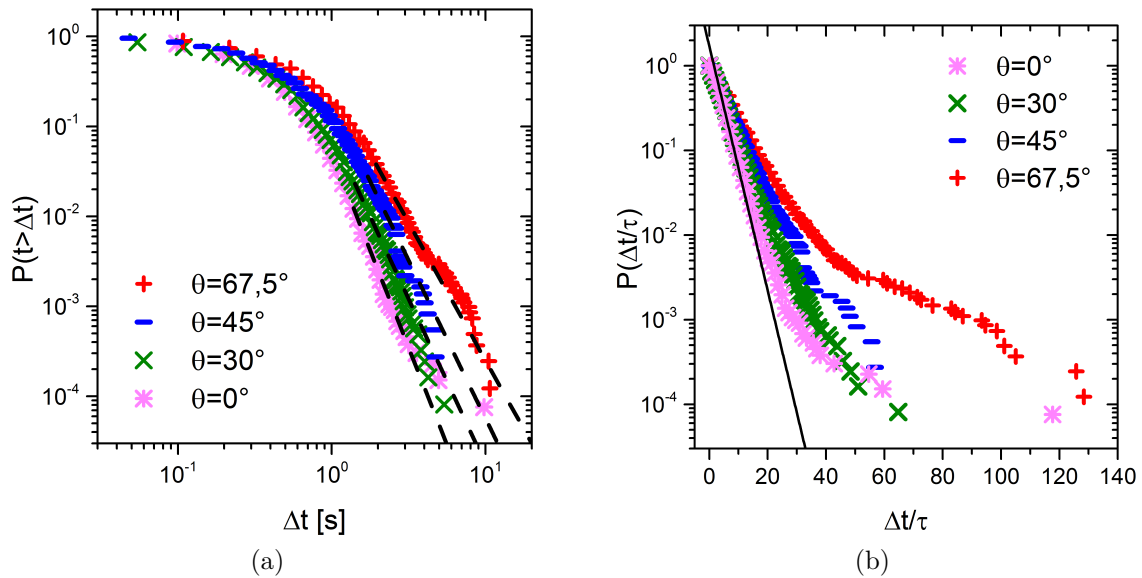


Figure 5.6: For  $D = 40 \mu\text{m}$  a. Survival function of  $\Delta t$  showing the power law tail regime where dashed lines are fits done by using the CSN method. We notice a steeper curve for a flat-bottom channel where  $\theta = 0^\circ$  describing a system less prone to jamming. In contrast, a tight angle of  $\theta = 67.5^\circ$  enhances dramatically the probability of having to experience jamming. b. Re-scaled CCDF of  $\Delta t$  with Stokes time  $\tau = \frac{a}{v}$  showing the divergence from the exponential (solid line).

## 5.4 The extreme case: $D = 10 \mu\text{m}$

### 5.4.1 Cumulative number of escapees

We adopt the same procedure described in Chapter 3 and applied in Chapter 4, we keep the same sampling window size and position. We look at the extreme case where the door width is equal to the diameter of the CR. We wait for a crowd formation to start our analysis. First we look at the cumulative number of escapees throughout the experiment. Figure 5.7 shows the evolution of this parameter with time. We notice that for a flat-bottom channel, where  $\theta = 0^\circ$ , the total number of escaped CR at the end of the experiment is the highest, while for the narrower channel, this number is the lowest for the same duration of the experiment. This indicates that more particles are escaping per second for  $\theta = 0^\circ$ . If we correlate this observation to past conclusions, we can start to see the trend of a system that is more prone to jamming as the angle becomes smaller (*i.e* as the bottom becomes flatter), however we would like to investigate more.

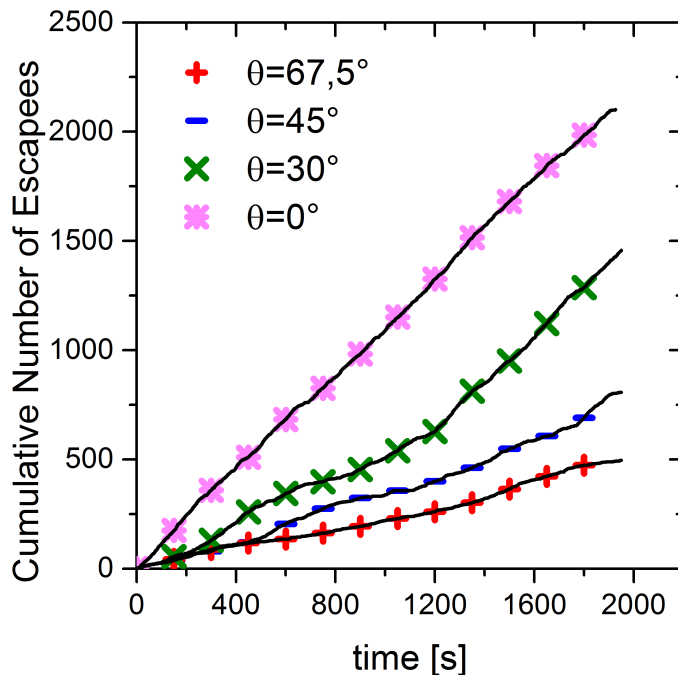


Figure 5.7: For  $D = 10 \mu\text{m}$ : Cumulative number of escaping CR through out the experiment for door width of  $D = 10 \mu\text{m}$  for different angle values  $\theta$ . For a flat-bottom channel where  $\theta = 0^\circ$ , the total number of particles that escaped is the largest compared to the narrower channel where  $\theta = 67.5^\circ$ . As the channel becomes flatter, the evacuation becomes easier.

### 5.4.2 Survival Function

Figure 5.8a shows the effect of angle variation on the time-lapse distribution, where for a flat-bottom channel, where  $\theta = 0^\circ$ , the value of  $\alpha$  is the highest resulting in a more steeper tail. Whereas for a tighter channel with  $\theta = 67.5^\circ$ , the plot presents the least steepness with the smallest parameter  $\alpha$ . This observation describes an evacuation process that is less susceptible to jamming for a flat-bottom channel compared to a narrower channel. Meaning that the narrower the channel is, the more confined the CR are leading to an acute jamming.

We also notice the collapse of the curves for small values of time-lapses ( $\Delta t$ ), these values represent the waiting times inside an avalanche. Re-scaling our time-lapses with the Stokes time described  $\tau$  in Chapter 4, Section 4.1.2 and plotting the values in a semi-logarithmic scale graph, Figure 5.8b, allow us to clearly see the distinct two timelapses regimes. The first, as mentioned before, for small  $\Delta t$  where the exponential regime is dominant. The second regime, is for what we define as long time-lapses, or long waiting times and the dominant trend is the power law tail (these values correspond to the waiting times between two consecutive avalanches). As one recalls, a power law tail defines a system in a jamming situation, more particularly in our case, the jamming is accentuated as the value of  $\theta$  increases. Indeed looking at one door size is not sufficient in order to have a conclusion on the effect of the angle. In fact, as stated by [Yu et al. \(2021\)](#), the effect witnessed in their study is for a door width to particle diameter ratio of 4.3. On the other hand, [López-Rodríguez](#)

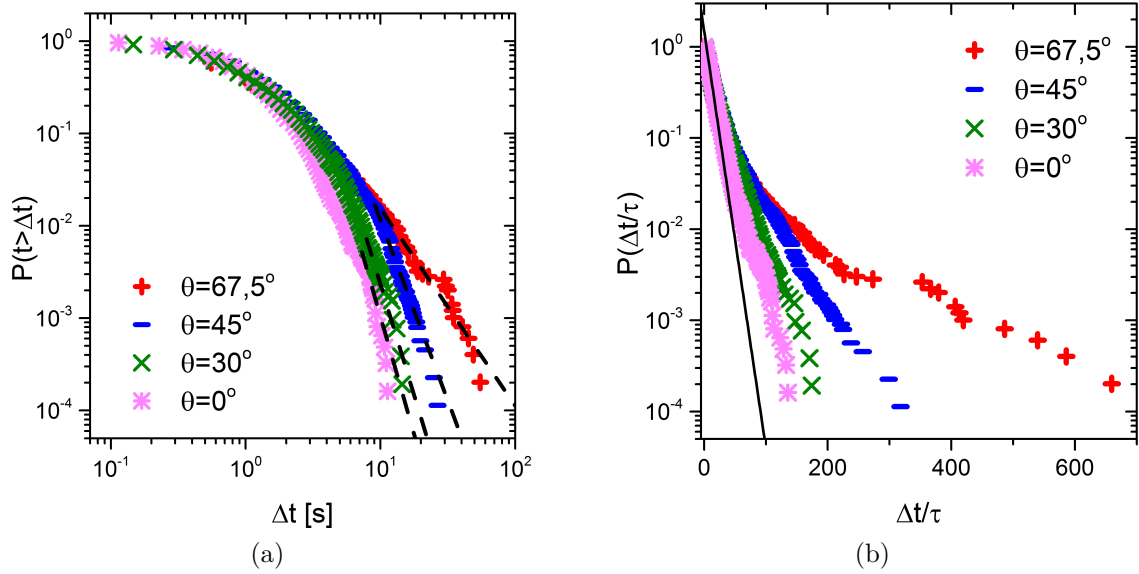


Figure 5.8: a. Survival function of time-lapses  $\Delta t$  showing the dominant power law tail regime. Dashed lines are fits done using the CSN method. As  $\theta$  increases, the parameter  $\alpha$  decreases and the probability of having longer waiting times increases. Longer waiting times signifies more jamming. b. Re-scaled values of  $\Delta t$  with Stokes time  $\tau$  showing the deviation from the exponential (Solid black line).

[et al. \(2019\)](#) found the behavior persistent for all  $D/d$  at all studied angle values, where  $D$  is the door width and  $d$  is the diameter of the particles.

## 5.5 Evolution of $\alpha$ for all $D$ and $\theta$ values

We can summarize the results of our studied cases just by looking at the relationship between the parameter  $\alpha$  with the variation of the angle  $\theta$  for different values of door width  $D$ . We plot this dependency in Figure 5.9 and observe a trend that appears for different angle values and door width. We can interpret the graph in two main ways. First we fix the door width  $D$  and vary the angle value  $\theta$ , what we observe is the same behavior that we described in the two extreme cases that we described in the paragraphs above. Mainly, as the value of  $\theta$  increases,  $\alpha$  decreases. In other words, as the channel geometry changes gradually from a flat-bottom channel towards a narrower one, the state of the system tends more and more toward jamming and the evacuation becomes more interrupted. That observation is quite the opposite of what have been reported in the literature and discussed in Chapter 1 Section 1.2.3. Another way to read the graph is by fixing the angle's value and changing the door

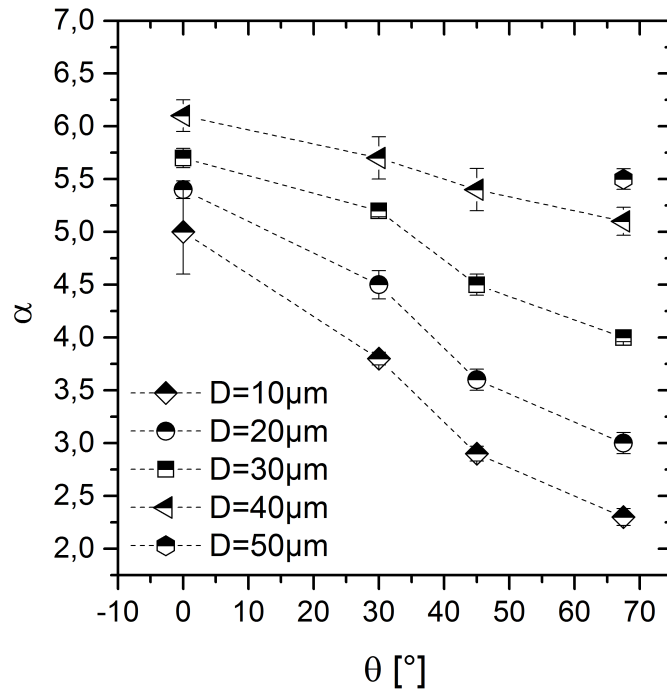


Figure 5.9: Evolution of  $\alpha$  with different values of  $\theta$ . The decrease of  $\alpha$  with the increase of  $\theta$ , a behavior common to all studied values of  $D$ , shows that the system tends to a jamming state as the channel converges to its tube-like shape.

width. This vertical method of reading shows that for a fixed value of  $\theta$ , and as we increase  $D$ ,  $\alpha$  increases, meaning that the system becomes less susceptible to jam. A behavior reminiscent of what we have observed in active suspensions of CR is Chapter 4 of this manuscript in the case of fixing average swimming velocity and changing door width.

We can notice that for  $D = 50 \mu\text{m}$  the system is jammed only for  $\theta = 67.5^\circ$  since only one value of  $\alpha$  is present, meaning that for other  $\theta$  the trend is exponential. We have already seen in Chapter 4 the faster is faster behavior appearing for  $D = 50 \mu\text{m}$  at  $V = 120 \mu\text{m/s}$  and  $\theta = 45^\circ$ . In addition, for the exponential regimes, we find

that the exponential constant is the same for  $D = 50 \mu\text{m}$  and  $D = 75 \mu\text{m}$ .

## 5.6 Avalanche size & Critical diameter $D_c$

Up to this stage, looking at the time-lapse distribution gave us an insight on the impact of the angle variation of the state of the system. We have seen that this impact is opposite to what have been registered in the literature mainly when comparing our results with the ones reported in Yu et al. (2021) where the focus of the study is to look at CCDF of  $\Delta t$ .

The observations so far are interesting, yet insufficient to cast a final and decisive conclusion. For the sake of robustness, we focus our attention on the avalanche size distribution for different values of  $\theta$  and  $D$ . A detailed definition of avalanche size  $s$  is given in Chapter 3, Section 3.4.1 and is the number of CR that escapes between two jamming events. Looking at this parameter gives us an idea of a potential critical door width value for a given angle above which the system's state becomes a continuous evacuation. We extract the minimum time-lapse  $\Delta t_c$  above which the system is considered jammed from the CSN method, since it represents the value of  $\Delta t$  where the power law tail begins. We plot the avalanche size averaged over the experiments  $\langle s \rangle$  for various values of  $D$  and  $\theta$ . Figure 5.10a reveals to us some

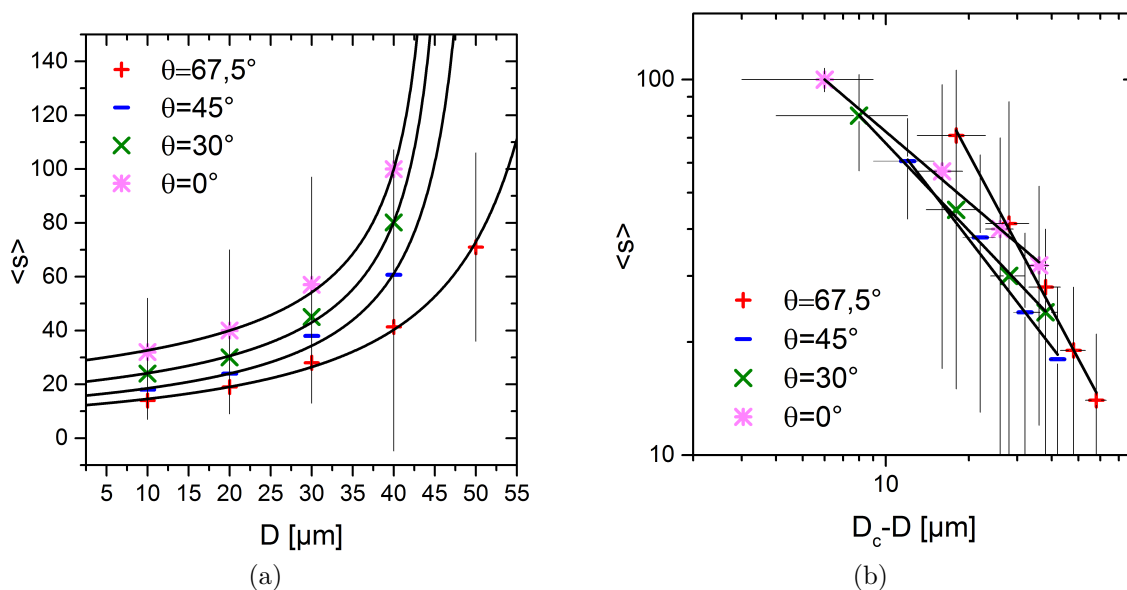


Figure 5.10: a. Evolution of avalanche size with door width for different angle values. The evolution exhibits a smooth increase behavior, in contrast to the step increase found in granular.  $\langle s \rangle$  decreases as  $\theta$  increases meaning that fewer particles escape between two jamming events describing a higher frequency of occurrence for these events. The solid lines represent the fit done by Equation 4.2 where  $D_c$ ,  $C$  and  $\beta$  are fitting parameters. b. Logarithmic scale graph showing the relationship of  $\langle s \rangle$  with  $D_c - D$ . Values of  $\beta$  and  $D_c$  are plotted in Annexe G.

interesting observations. We observe a smooth increase of  $\langle s \rangle$  with increasing

$D$  for all values of  $\theta$ . Interestingly enough, a semi-logarithmic scale graph reveals the power law divergence nature of this trend. Similar to what we have empirically deduced for the velocity and door width correlation in Chapter 4, we can express the relationship between  $\langle s \rangle$  and  $D$  in terms of Equation 4.2, where the  $\langle s \rangle$  diverges for values of  $D \geq D_c$  and the system becomes in its flowing state.

Another information that we can extract from the graph via reading it vertically, is that the average avalanche size increases with decreasing  $\theta$ . Meaning that as the channel leans toward a flat-bottomed geometry, the jamming events are reduced and more particle are able to pass. This observation adds the divergence in behavior between active suspensions and granular systems where the jamming events increase as the channel becomes flatter.

## 5.7 Jamming probability

In Chapter 4 section 4.3.2 we introduce the notion of jamming probability. We borrowed a probabilistic model developed for granular systems defining  $\gamma(s)$  as the probability of finding an avalanche of size  $s$ . We define the expression of  $\gamma(s)$  as  $\gamma(s) = p^s(1 - p)$  where  $p$  is the probability of a CR passing through the door without cooperating with its neighbors to jam the door. We extract the value of  $p$  by fitting the histogram of avalanche distributions for all angle values and door width with the expression of  $\gamma(s)$  where  $p$  is a fitting parameter. A jamming probability that is equal to zero defines a system in its flowing state where no interruptions occur during evacuation. We plot these values as a function of  $D$  for all the studied angles in Figure 5.11. The results confirm the observations made for the time lapse and that the jamming is highly probable for small doors and big angles  $\theta$ .

We are more interested in comparing the influence of geometrical change on the jamming probability. More simply, we would like to see the most effective geometric change to do in order to reduce the jamming probability. For  $D = 10 \mu\text{m}$ , decreasing the angle  $\theta$  by almost 100 %, decreases the jamming probability by almost a factor of 2.5, where as for a very tight channel with  $\theta = 67.5^\circ$ , quadrupling  $D$  leads to a decrease in the jamming probability by a factor of almost 3.46. We notice that increasing  $D$  leads to a more significant decrease in the jamming probability than varying  $\theta$ .

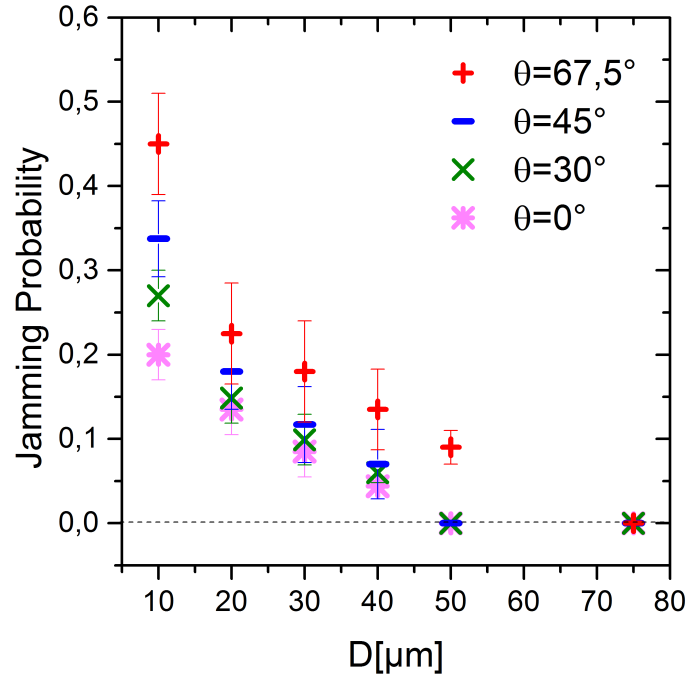


Figure 5.11: Jamming probability evolution with door width  $D$  for different  $\theta$ . The jamming probability is an important parameter that gives us an insight to the state of our system. For very small doors and high  $\theta$  the jamming probability is the highest, meaning that the evacuation experiences lots of interruptions and the system is in a state of jamming.

## 5.8 $D - \theta$ phase diagram

Having determined the critical value of the door width  $D_c$  and the jamming probability for a fixed  $\theta$  and various values of  $D$  we can now build the phase diagram proper to our system in Figure 5.12. The transition belt, depicted by stars, represent the values of  $D_c$  obtained by applying Equation 4.2 and extracting the fitting parameters. This belt consists of a transition zone between jamming and flowing regimes. Reading the phase diagram gives us important information on the behavior of our system. We can divide our observations into two main categories:

1. A first zone exists for values of  $D$  such as  $D < D_c$ . In this domain, the system is subjected to jamming. Furthermore, we notice as the door width gets smaller at the angle  $\theta$  increases, the jamming probability becomes more significant. Physically, this scenario represents a very small door with a very tight channel. Hence, for small  $D$  and large  $\theta$  our system is subjected to high probability of being jammed. As we approach the boundary, the jamming probability decreases but does not cancel out.
2. The second zone starts for  $D \geq D_c$ . In this region the values of  $D$  are relatively large and those of  $\theta$  are relatively small. For these values, the system does not experience jamming and the evacuation is uninterrupted.
3. It is also important to pinpoint the geometrical constraints of our diagram.



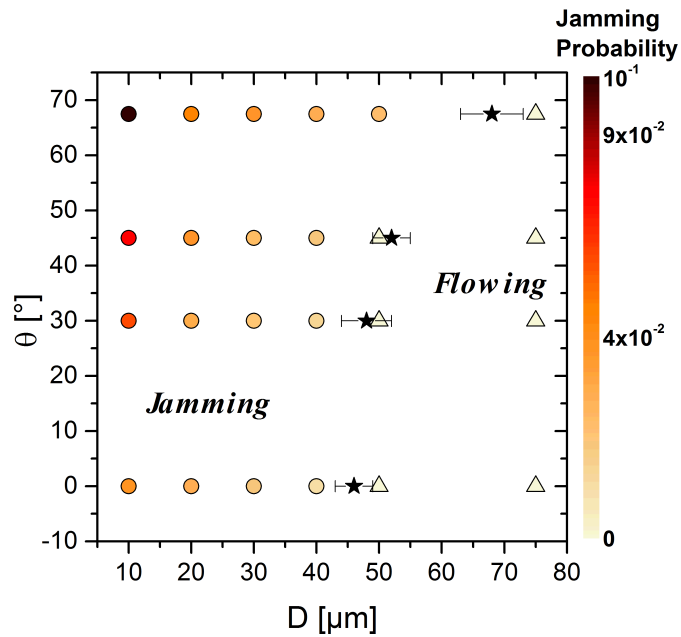


Figure 5.12: Jamming phase diagram showing the relationship between the angle  $\theta$  and  $D$  in defining the state of the system. The black stars (★) represent the values of  $D_c$  extracted from fitting Equation 4.2, these values constitutes a transition belt. For small values of  $D$  and large values of  $\theta$  the system is in the jamming regime (○). The jamming probability increases as  $\theta$  increases. For large values of  $D$  and relatively smaller values of  $\theta$  the system is in the flowing regime with a null jamming probability (△).

Mainly, the region beyond  $\theta = 67.5^\circ$  is of no interest to our investigation, since the channel is reduced to a tube and no *crowd* can be formed.

## 5.9 Discussion

We have now at our disposal enough data and observations to conclude that the phenomenology behind jamming in active suspensions, in particular in *Chlamydomonas Reinhardtii* is different to the one causing clogs in granular systems. We have found no evidence regarding the effect of channel's angle in humans or animals in literature to compare. We will discuss the main differences in both systems that, in our opinion, lead to this divergence in causality of interrupting an evacuation. We look at two main causes, the first being related to the mechanism by which the CR perceives the light and by consequence reacts to it. The second, corresponds to the interactions of the CR with its surroundings, mainly its reaction when it hits the wall.

First, let us look at the mechanism by which the suspension responds to light and swim towards the exit. We have seen in Chapter 2, section 2.5.2 a response to light is characterized by a response time of the order of 2 s, during which the CR re-orient themselves and start their ballistic swimming in the direction opposite to the light source. It is important to remember that the CR do not possess an eyesight, hence they do not *see* the exit in the same manner that humans or animals do. As a result, their *run* toward the exit is more of an escape from the light. Hence when they approach the door, they do not change their trajectories in order to pass through it, rather they maintain their ballistic nature.

This observation brings us to our second interpretation that is complementary to the first, mainly wall interaction. We turn our attention to the work done by [Kantsler et al. \(2013\)](#) where they studied the swimming behavior of the *Chlamydomonas Reinhardtii* in the vicinity of a wall. They reported that a contact happens between the CR and the wall, and that the CR pushes itself away from the wall by help of its flagella. In general, a CR swims towards the wall with a certain angle of incidence, get stuck on the wall, then due to successive beating of its flagella, the CR modifies its angle of incidence, until the initial value is completely lost and the CR swims away from the wall. This experiment puts forward the fact that CR-wall interactions are not governed solely by hydrodynamics; the beating of the flagella has a role to play.

We can now understand better the dynamics of our crowd, in a flat-bottom channel, CR swim in a linear trajectory towards the wall, after re-orientation, they built up in a space that does not interrupt the evacuation, some of them bounce back but do not interfere with those whose trajectories are directed toward the door, see Figure 5.13a. However, for a very narrow channel, the build up and bouncing back happens in a very tight space, interfering with other CR, see Figure 5.13b.

In summary, we can conclude that the behavior proper to the CR induces the difference observed compared to granular systems. For the granular systems, the grains tend to sediment when they are in contact, and when stacked on top of each other, their velocity becomes null, whereas active suspensions, CR in particular, tend to swim away from the walls, and their velocity is non zero inside the crowd.

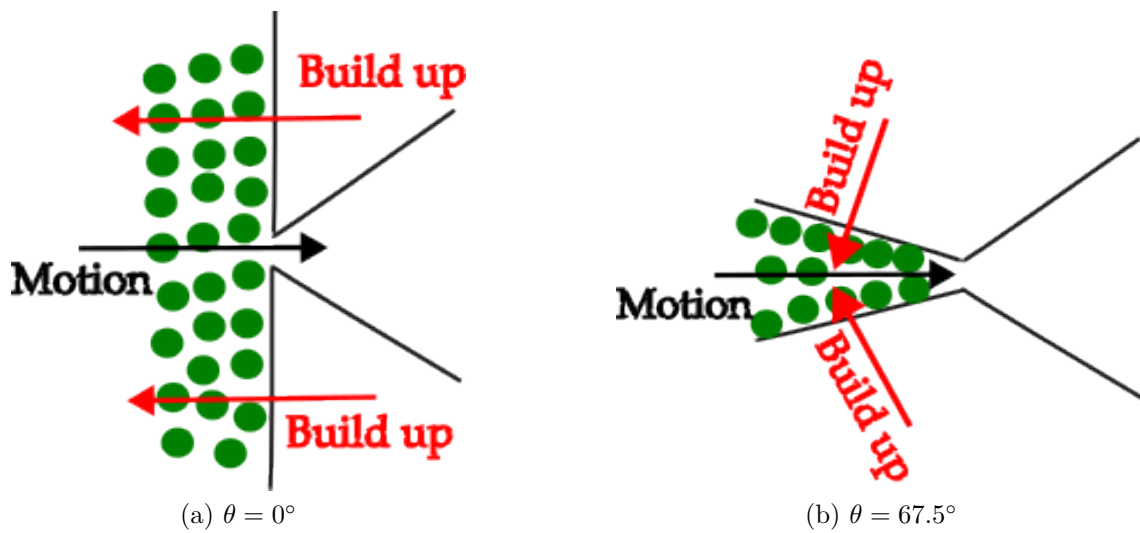


Figure 5.13: Schematic describing the motion of the CR moving toward the door. a. For a flat-bottom channel, the direction of build-up on the walls is opposite to the ballistic direction of incoming CR. b. In a narrower channel, the direction of build-up interferes with the incoming CR.

## Conclusion & Perspectives

### General Conclusion

In this manuscript, we address the experimental study of a crowd of microswimmers. We focus on crowds in evacuation, meaning when a large number of individuals attempt to escape from one exit. The literature showed us that a pattern emerges for different types of crowds, from animals to humans to grains. A paradox is often observed in these systems and can best be described by the term "Faster is slower"; the faster a crowd runs towards the door, the longer the evacuation takes. The systems studied so far are dominated by short range forces such as contact forces; grain-grain collisions or human-human interactions.

We tackle the problem of evacuation in a yet unexplored system, that of active suspensions. This type of crowds is different from what has been reported in literature so far in the sense that the hydrodynamic forces might play a role in the cell-cell interactions.

To do so, we use the algae *Chlamydomonas Reinhardtii* and we exploit its phototactic properties, mainly its tendency to run away from the light. We position the source parallel to the door so that the motion is directed towards it. The suspension swims in a prefabricated channel made of PDMS. The bottleneck shape of the channel induces a confinement effect on the crowd forcing a build up of high volume fraction at the entrance, similar to the observed behavior reported for other crowds in the literature, altering the exit mechanism. We control the average swimming velocity of the population by altering the viscosity of the medium. We quantify the evacuation efficiency by looking at the cumulative number of escaping cells, where we can discern a certain waiting time in which no cells are passing, then we plot the survival function of these waiting times. First, we look at a large door size, roughly six times the diameter of the algae. We observe an exponential trend for a wide range of swimming velocities describing an uninterrupted flow.

On the other hand, for a smaller door width, and for a range of velocities, the survival function takes a power law tail trend similar to the one described in the literature, in addition, the tail becomes steeper as the velocity is decreased, meaning that the slower the CR swim towards the exit the faster is the evacuation, a behavior reminiscent to the "faster-is-slower" in other types of crowds. As a result, we observe

a transition from jamming to flowing dependent on the values of  $D$  and  $V$ .

A  $D - V$  phase diagram built by the help of probabilistic models borrowed from granular systems, shows the transition belt of critical diameter values under which the combination of velocity and door width leads to a system in a jamming situation. However, above this transition belt, the  $(D, V)$  gives a system in a flowing state.

Furthermore, in an attempt to unravel the mechanisms behind this jamming effect, we look at purely geometrical parameters, where we fix the swimming velocity but change 1) the angle that the channel's walls form with the vertical ( $\theta$ ), 2) the door width. We modify the channel configuration and the initial quantity of the injected suspension in order to maintain a constant build on the door (the volume fraction of the crowd increases and saturates). Results show a discrepancy with what have been reported in literature. Mainly we observe a more fluid evacuation for a flat-bottom channel, contrary to what have been reported in other types of crowds. This implicates a difference in the jamming phenomenology, since, until now, it has been argued that jamming is due to arch formation. We argue that jamming in our active matter system is mostly due to the increase in interactions inside the crowd due to more cells jumping off the walls as the channel becomes narrower. We speculate that our system does not present any solid friction between the cells (at the origin of arches). Indeed, the contact is probably due, in our case, to flagella that are pushing other cells.

## Perspectives

The novel nature of this experimental work gives room to a broad range of perspectives. We have so far looked at the effect of the different parameters, the swimming velocity  $V$ , the door width  $D$  and the angle  $\theta$ . We were able also to draw a conclusion regarding the state of the system following the values of these parameters;  $(D, V)$  and  $(D, \theta)$ .

### $V - \theta$ diagram

In order to draw the full picture of the state transition of the system, it is only logical to aim at building the  $V - \theta$  diagram. The experiment is done by fixing the door width  $D$  and changing both the velocity and the angle  $\theta$ . We started looking at some configuration during the internship of Simon Braud. We found that the evacuation at lower values of  $V$  is still enhanced when  $\theta$  is null. Figure 5.14 shows the survival function for  $D = 10 \mu\text{m}$  and  $V = 100 \mu\text{m/s}$ . We can see when the channel is in a straight wall configuration ( $\theta = 0^\circ$ ) the waiting time are less.

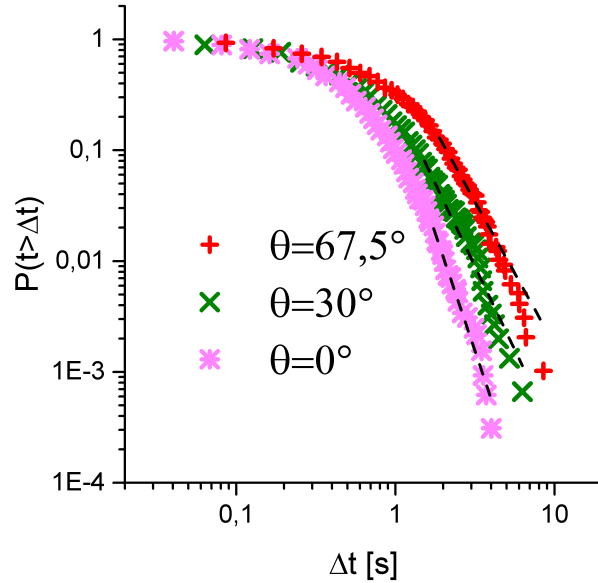


Figure 5.14: Survival function for  $D = 10 \mu\text{m}$  and  $V = 100 \mu\text{m/s}$ . We notice that for  $\theta = 0^\circ$  the waiting times are less. This indicates that the evacuation is less susceptible to jamming.

## Effect of obstacles

It is reported in the literature the effect of an obstacle present in front of the door on increasing the efficiency of the evacuation. Hence, a series of experiments on active suspensions can be previewed. A good approach would be to test different obstacle sizes as well as distances to the door and observe their effect on the evacuation.

## Deep learning & $V - \phi$ diagram

We mentioned the limits of `trackpy` when it comes to identify and track particles in a high density regime. Being able to do so will give us information about the velocity of the cells inside the crowd. Having calculated the density via the calibration method detailed in Chapter 2 we can construct the  $V - \phi$  diagram. This gives us an insight on the interplay between velocity and density.

A collaboration is undergoing with a team in the department of physics of the University of Gothenburg, Sweden to use deep learning to track particles in dense regimes. The approach is to use DeepTrack, a python based deep learning framework for microscopy. They have established that it is best to use the LodeSTAR algorithm (Low-shot deep Symmetric Tracking And Regression) for multi-particle tracking. LodeSTAR algorithm (Midtvedt et al., 2022) is a part of deeptrack able to learn to track particles. It works by focusing on the inherent symmetries of particles tracking. This enables the training using just a single image of one particle.

Figure 5.15 is a schematic that resumes the working of LodeSTAR as presented

by [Shivan Gurumurthy \(2022\)](#). First the authors start with an image of a single particle, the source of the image is the recorded experiments. Then, they create several images via translating or rotating the original one. Using a neuron network, they can predict the center of each particle in each image. A neural network is used to obtain the  $x, y$  outputs. The vectors  $(x, y)$  estimate the distance from each pixel to the center. A weight map (normalized to sum to one) is provided and it corresponds to the probability of finding the center of the particle near each pixel. The final prediction of the position of the center of the particle is obtained by an average of the estimated particle positions weighted by the weight map. Predictions are used to train the neural network by using the difference as the loss function.

Figure 5.16 shows the preliminary results of the detection. The continuity would be to link particles from one frame to another to calculate the velocity.

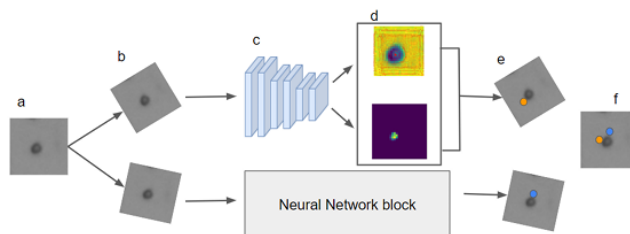


Figure 5.15: Example flowchart of the working of LodeSTAR. An image with a single particle is rotated with an arbitrary angle and is fed to a convolutional neural network. The neural network outputs two tensors (feature maps). One (top) is a map where each pixel represents the distance of the particle from the center of the image. The other tensor (bottom) is a weight map (normalized to sum to one) corresponding to the contribution of each element in the top feature map to the final prediction. These two tensors are multiplied together and summed to obtain a single prediction of the position of the particle for each transformed image. ([Shivan Gurumurthy, 2022](#))

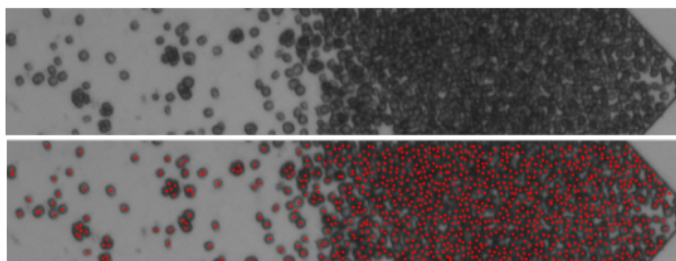


Figure 5.16: Top: screenshot of the experiment. Bottom: red dots indicating that the algorithm was able to detect a particle. ([Shivan Gurumurthy, 2022](#))

---

## **Numerical Simulations**

As one might notice, this manuscript is a purely experimental study aimed at providing enough observations in order to extract the basic mechanisms that will lead to a correct numerical analysis to replicate the observed effects. One aspect of a future work could be to use the data provided to model the behavior of active suspensions in evacuation accordingly.





---

# Annexes

Conformément aux recommandations de l'école doctorale de physique, il est nécessaire de dédier une partie du manuscrit à un résumé rédigé en langue française.

## A Introduction

Ce chapitre consiste à fournir une introduction sur les foules déjà présentes dans la littérature. On entend par le mot *foule* un grand nombre d'entités qui se rassemblent. A part le côté social et psychologique des foules, on s'intéresse à l'aspect physique de ces dernières . En effet, les physiciens se sont mis à étudier le mouvement des foules du point de vue physique, tout en essayant de le modéliser afin de pouvoir comprendre et prédire. On se rappelle notamment le fameux modèle de Vicsek ([Vicsek et al., 1995](#)) qui s'intéresse à l'émergence d'un mouvement collectif chez les oiseaux.

Autre situation qui attire l'attention des physiciens, et qui consiste le sujet principal de notre étude, concerne des foules en situation d'évacuation. En effet, un effet paradoxal est observé lors d'une course vers une sortie en cas d'urgence, notamment le fait que courir plus rapidement vers la porte cause un *bouchon* qui rend l'évacuation lente et inefficace d'où la dénomination *faster is slower* . Cette observation empirique est supportée, par des calculs numériques développés par [Helbing & Molnar \(1995\)](#) basée sur la théorie des forces sociales ou "social force model (SFM)" en anglais. Ce modèle, utilisé pour simuler le comportement des foules humaines, considère que le mouvement des humains est imposé par trois types de forces. La première, nommée *force de désire*, est le résultat du *désire* des individus d'atteindre une certaine vitesse de marche *désirée*. La seconde force est de nature sociale et se traduit par la tendance des piétons à ne pas se heurter les uns aux autres. Et finalement, une troisième force de type *granulaire* qui domine lorsque deux piétons rentrent en contact. Ce modèle montre que le temps d'attente entre deux évacuations consécutives augmente avec la vitesse de marche vers la porte.

Une observation intéressante se fait quand le modèle de [Helbing & Molnar \(1995\)](#) est appliqué pour de grandes vitesses de marche. [Sticco et al. \(2017\)](#) montrent que l'effet paradoxal "faster-is-slower" existe pour un certain intervalle de vitesses, au delà duquel le temps de blocage commence à décroître. La raison principale est qu'au delà d'une vitesse seuil, l'énergie cinétique est suffisante pour rompre les architectures responsables du blocage, plus précisément, les arches sont détruits.

Parallèlement aux études numériques existe une large littérature sur des expériences dans des environnements bien contrôlés pour observer l'évacuation des foules de piétons et des foules de moutons. Les deux systèmes présentent une similitude dans leur comportement, à savoir plus la vitesse (et par conséquent le niveau de compétition) augmente, plus le temps de blocage augmente. C'est ce que [Zuriguél et al. \(2014\)](#) montre dans leurs études. Ce phénomène est aussi observable chez les systèmes de type granulaire.

Nous venons d'observer un phénomène qui est assez commun chez différents types de foules. Notre but est d'introduire un nouveau type de système, celui des micro-nageurs, et d'étudier expérimentalement l'influence de certains paramètres, physiologiques et géométriques, sur l'évacuation. En d'autres termes, voir si ce comportement assez paradoxal persiste dans un système très différent que sont les

suspensions de micro-nageurs.

## B Matériels et Méthodes

Pour répondre à la problématique qu'on s'est posé en introduction, il nous faut un protocole expérimental robuste et pertinent. Ce chapitre résume les étapes que nous suivons dans le but de réaliser nos expériences.

### B.1 Micro-fabrication Standard

Afin de fabriquer les canaux dans lesquels notre suspension nage, nous avons recours aux méthodes classiques de micro-fabrication qui nous permettent de contrôler la hauteur de nos canaux. Cette méthode assez standard est facile à mettre en œuvre à condition d'avoir une salle dédiée où la température et l'humidité sont contrôlées. La fabrication débute par l'étape de moulage, où nous utilisons la méthode de *soft lithography* pour graver des motifs imprimés sur des masques. Après avoir fabriqué le moule, on verse une solution visqueuse de mélange de silicone et réticulant, "le Polydimethylsiloxane (PDMS)", sur le moule qui repose dans une boîte de pétri. Le tout est mis au four à une température de 65 °C pour 2 h. Une fois la cuisson terminée, le canal est fixé à une lame de verre par le biais d'un processus plasmé-oxygène. Des trous sont ouverts à l'entrée et la sortie pour injecter la suspension.

### B.2 Suivi des particules

Il est aussi important, pour notre étude, de savoir la position de nos particules à tout moment tout au long de l'expérience. C'est pour cette raison que nous avons recours à la méthode de suivi des particules. Le suivi est réalisé à partir de la librairie *trackpy* en langage *python*. Cette librairie nous permet d'analyser des vidéos et d'en tirer des informations pertinentes sur les trajectoires des particules. Cela nous permet de calculer la vitesse instantanée de chacune des particules afin d'obtenir la vitesse moyenne de la population.

### B.3 Calculs de densité et Calibration

Un paramètre important à surveiller dans des expériences de foules est la densité. En effet, suivre l'évolution de la densité à la sortie nous donne une information sur la formation du front tout au long de l'expérience. Cette mesure s'avère nécessaire pour déterminer le moment où la densité de la foule atteint sa valeur maximum et ainsi commencer notre traitement. Cette quantité est mesurée à partir des niveaux de gris suivant la loi de Beer-Lambert, qui relie l'absorbance à la fraction volumique. Cependant, la linéarité de cette loi n'est pertinente que pour des régimes de fraction volumique inférieurs à 2.5 %. À savoir que notre système atteint des valeurs beaucoup plus importantes au niveau de la porte. Nous avons recours à la dilution logarithmique afin de calibrer la mesure de la fraction volumique pour des zones où

la linéarité de la loi Beer-Lambert perd de pertinence. Ainsi on aura une relation qui nous semble mieux décrite par un polynôme du quatrième degré.

## B.4 *Chlamydomonas Reinhardtii* Cultures et Propriétés

Nous dédions cette section à la présentation de micro-nageur modèle que nous utilisons, une micro-algue connue sous le nom de *Chlamydomonas Reinhardtii* (CR). Le protocole de culture de CR est bien connu au sein de notre équipe. Les CR sont cultivées en premier temps sous leur forme solide (plutôt pâte) sur du gel Agar avant d'être diluées dans du TAP pour avoir une suspension. Leur croissance atteint son maximum après trois jours dans des conditions de culture bien contrôlées. Cette micro-algue est assez intéressante grâce à sa forme sphérique qui rend sa modélisation facile, ainsi qu'à sa propriété photo-tactique. En effet, la souche CC124 que nous utilisons a la tendance de fuir la lumière (photo-tactisme négatif). Ainsi, nous pouvons diriger notre suspension vers la porte (une constriction) à l'aide de la lumière.

De même, augmenter la viscosité par le biais d'ajout de Dextran, entraîne une diminution dans la vitesse moyenne de nage de notre suspension sans effet secondaire sur la physiologie de nos algues. Cette méthode est importante car nous désirons justement voir l'effet de la vitesse de nage sur l'efficacité de l'évacuation. En plus, nous notons une baisse de vitesse de nage en fonction du confinement du canal, un phénomène connu sous le nom de l'effet *Helen-Shaw*.

## B.5 Une expérience typique

Les échantillons de suspensions sont concentrés par centrifugation et laissés au repos pour une heure sous lumière rouge. Une expérience typique se déroule en injectant du BSA dans le circuit pour réduire la probabilité d'adhésion aux parois. Ensuite, nous introduisons la suspension de CR dans le circuit que nous fermons hermétiquement. Le circuit est déposé dans une boîte noire avec des fenêtres en filtre rouge pour observer sans laisser passer de la lumière blanche extérieure. L'enregistrement démarre avec l'allumage de la lampe LED qui déclenche la nage des CR vers la porte. Une perte de photo-tactisme détermine la fin de l'expérience.

# C Outils statistiques pour l'analyse des foules de micro-nageurs

## C.1 Temps d'attente

Une information importante qui nous permet d'évaluer l'efficacité de l'évacuation est le temps d'attente. Nous procédons à analyser le nombre cumulé des particules qui sortent en aval tout au long de l'expérience, le graphique présente des plateaux marquant un temps d'attente où aucune particule ne s'échappe. Ainsi, plus ce plateau est long plus le blocage est grand.

Nous avons recours aussi à tracer la fonction de survie (CCFD en anglais) des temps d'attente qui présente une loi de puissance qui décroît en  $\frac{1}{\Delta t^{\alpha-1}}$ . Pour bien trouver le point où la loi de puissance commence, nous utilisons la librairie *powerlaw* en langage *python*.

## D Transition de blocage, le diagramme $D - V$

Nous avons abordé la problématique de la description du processus d'évacuation des suspensions actives de deux points de vue différents. Tout d'abord, nous nous sommes intéressés aux laps de temps, et avons quantifié le temps qui sépare deux évacuations consécutives. Nous avons détaillé le processus de réflexion pour deux scénarios, pour une grande largeur de porte  $D = 67 \mu\text{m}$  (cas 1), qui est environ la taille de sept CR, et pour un petit diamètre de porte  $D = 10 \mu\text{m}$  (cas 2) à peu près la taille d'un CR, tout en faisant varier la vitesse de nage. Pour le cas 1, nous avons constaté que la CCDF suit une tendance de décroissance exponentielle et peut être remise à l'échelle avec un paramètre connu sous le nom de temps de Stokes  $\tau$ . Nous avons constaté que  $\tau$  est proportionnel à l'inverse du flux. Le cas 1 décrit un processus d'évacuation typique où aucune obstruction ne se produit, une augmentation de  $V$  entraîne une amélioration de l'évacuation. Le cas 2 est tout à fait opposé, où les CCDF des intervalles de temps suivent une queue de loi de puissance, typique des systèmes bloqués, le système étant de plus en plus obstrué lorsque  $V$  augmente. Un regard sur le paramètre  $\alpha$  laissait entrevoir la présence possible d'une zone de transition.

Nous avons abordé l'étude sous un angle différent, celui de la taille de l'avalanche pour localiser la zone de transition. En effet, l'évolution de  $\langle s \rangle$  avec  $D$  pour différents  $V$  suit une loi de puissance qui diverge pour une valeur critique de  $D$ ,  $D_c$ . Pour  $D \geq D_c$  le système est dans son état *flowing*. De plus, nous avons calculé la probabilité de blocage pour chaque paire  $V - D$ , en appliquant à notre cas les modèles probabilistes utilisés dans les systèmes granulaires.

Nous avons pu construire un diagramme  $D - V$  qui montre la bande de transition identifiée par les valeurs de  $D_c$ . L'état du système, soit *flowing* ou *jamming*, dépend de la position du point expérimental par rapport à cette *frontière*.

En conclusion, nous sommes en mesure d'affirmer que lors d'une évacuation, et lorsque la foule se forme à la sortie, les suspensions actives présentent un comportement similaire à celui qu'on appelle "faster-is-slower" dans d'autres types de foule. De plus, la compatibilité des modèles probabilistes issus des systèmes granulaires et appliqué à notre cas, laisse entrevoir des similitudes sous-jacentes dans les problèmes de blocage entre les deux systèmes.

## E Transition de blocage, le diagramme $D - \theta$

Dans ce chapitre on s'intéresse à savoir si les lois qui gouvernent l'évacuation des systèmes granulaires sont les mêmes pour les suspensions actives. La littérature nous montre que les causes du blocage dans les systèmes granulaires est la formations d'arcs sur la porte. La stabilité et la probabilité de formation de cet arc sont liées

à une contrainte géométrique; l'angle  $\theta$ .  $\theta$  n'est que l'angle que forme les murs du canal avec la verticale. Les observations enregistrées dans la littérature montrent que plus  $\theta$  tend vers un angle droit (le canal devient un tube), plus l'évacuation est fluide. Au contraire, plus l'angle tend vers  $0^\circ$ , l'évacuation devient plus difficile dû à la formation et la persistance des arcs.

En fixant la vitesse de nage, on varie la dimension de la porte et l'angle. On observe qu'en augmentant  $\theta$  l'évacuation devient plus difficile et vice versa. Ceci est contradictoire aux observations dans la littérature.

En suivant la même procédure décrite dans le section précédente, on est capable de dresser le diagramme de phase  $D - \theta$ . On observe deux régimes définis par une frontière de transition définis par les valeurs critique de  $D$ ,  $D_c$ . On observe un régime de colmatage pour des grandes valeurs de  $\theta$  et  $D < D_c$  avec une grande probabilité de blocage. Tandis que pour des valeur de  $D$  supérieurs à  $D_c$  le système ne subit aucun blocage.

On argumente que ceci est dû aux différents mécanismes avec lesquelles les particules s'orientent vers la porte ainsi qu'aux interactions particules-mur. En effet, nos suspensions gardent leurs trajectoires rectilignes et se heurtent aux murs du canal. Les interactions cellules-murs engendrent un effet de repoussement où les CR nagent dans le sens inverse. Dans une géométrie assez étroite, la cellule rebondit rejoint la foule en heurtant d'autres cellules ce qui engendre plus de blocage.

## F Additional data for Chapter 4

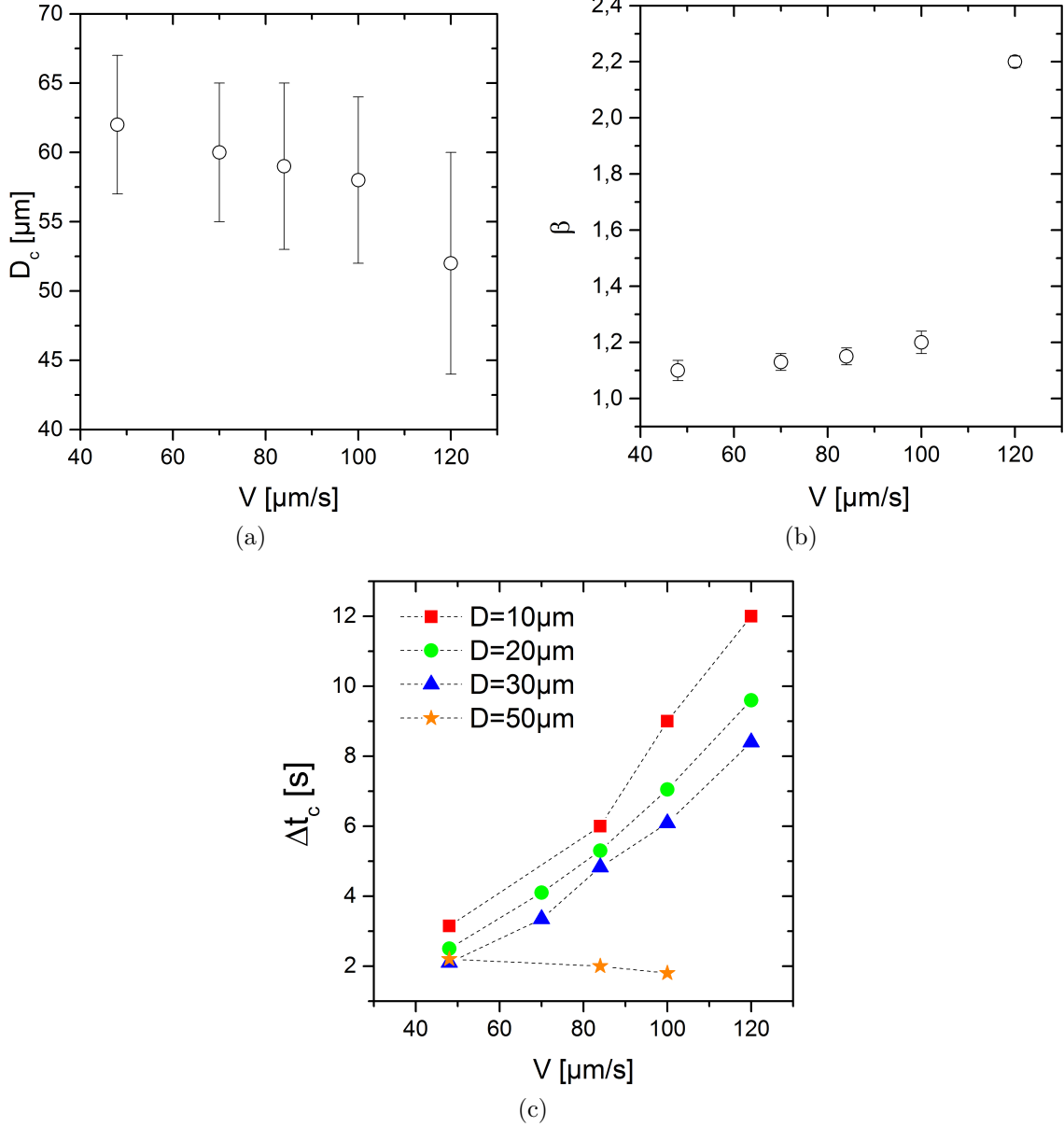


Figure 17: a. Critical values of  $D$  as function of the swimming velocity  $V$ , these values are used to build the  $D - V$  diagram in Chapter 4, section 4.3.3 b. Values of the exponent  $\beta$  as function of  $V$ .  $\beta$  is a fitting parameter of Equation 4.2. c. Values of the critical waiting times  $\Delta t_c$  for all the values of  $D$  and  $V$  given by the CSN method.



## G Additional data for Chapter 5

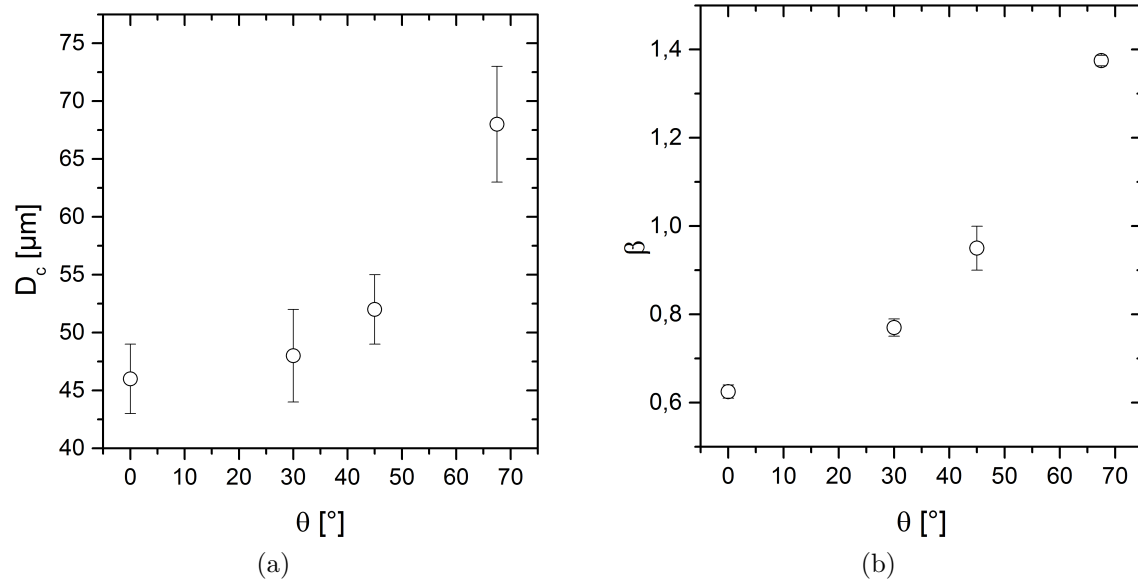







Figure 18: a. Values of  $D_c$  obtained from fitting and used for building the  $D - \theta$  diagram. b. Values of the exponent  $\beta$  as a function of  $\theta$ .

## H Article & Supplementary materials

**Active jamming of microswimmers at a bottleneck constriction**Edouardo Al Alam <sup>1</sup>, Marvin Brun-Cosme-Bruny <sup>1</sup>, Vincent Borne,<sup>1</sup> Sylvain Faure <sup>2</sup>,  
Bertrand Maury,<sup>3,2</sup> Philippe Peyla <sup>1</sup> and Salima Rafai <sup>1,\*</sup><sup>1</sup>Université Grenoble Alpes, CNRS, LIPhy, F-38000 Grenoble, France<sup>2</sup>Laboratoire de Mathématiques d'Orsay, Université Paris-Saclay, 91405 Orsay Cedex, France<sup>3</sup>Département de Mathématiques Appliquées, Ecole Normale Supérieure, Université PSL, Paris, France

(Received 10 May 2022; accepted 14 September 2022; published 26 September 2022)

When attracted by a stimulus (light), microswimmers can build up very densely at a constriction and thus cause jamming. The microalga *Chlamydomonas Reinhardtii* is used here as a model system to study this phenomenon. Its negative phototaxis makes the algae swim away from a light source and go through a microfabricated bottleneck-shaped constriction. Successive jamming events interspersed with bursts of algae are observed. A power-law decrease describes well the distribution of time lapses of blockages. Moreover, the evacuation time is found to increase when increasing the swimming velocity. These results are reminiscent of crowd dynamics and, in particular, what has been called the faster is slower effect in the dedicated literature. It also raises the question of the presence of tangential solid friction between motile cells densely packed. Furthermore, we demonstrate the existence of a transition from a jammed phase described by a power-law decrease to an uninterrupted phase described by an exponential decay, we characterize such a transition as a function of door size and swimming velocity. Interestingly, the exponential flowing regime shows what might be referred to as “a faster is faster” regime.

DOI: [10.1103/PhysRevFluids.7.L092301](https://doi.org/10.1103/PhysRevFluids.7.L092301)

In biotechnologies, harvesting micro-organisms, such as bacteria [1] or microalgae [2] is now a tremendous challenge to extract new drugs and chemicals [3,4]. Several microfluidic devices have recently emerged to achieve such a task [5–7]. A jamming phase can often occur when concentrated cells are transported by a fluid [8–10]. At the microscale, jamming results from the accumulation of cells at a constriction, leading to the buildup of fouling layers. Jamming can severely disrupt the performance of microfluidic devices [11]. Initially, it reduces the permeability of channels or pores and eventually leads to a complete obstruction of the flow [12,13]. Jamming is, thus, one of the leading causes of efficiency loss in high-throughput technologies processes [14]. To remedy fouling and jamming, it is usually necessary to completely stop the process and use cleaning strategies that consume energy and time before restarting the process [15]. Motile cells (bacteria or microalgae) can self-accumulate without an external flow and can go to nest in a particular place of the circuit (pores, porous regions, constrictions), thus, forming an active jamming that is essential to characterize. Beyond jamming, this type of accumulation can be a precursor to formation of biofilms. More generally, jamming problems occur in extremely varied situations that are nowadays very much studied in the context of crowd dynamics. Crowd motion modeling has become a very active field of research, and serious debates on how to model certain behaviors, such as panic movements are still ongoing in the community [16]. In this particular case, the faster is slower (FiS) effect plays a central role: It essentially indicates that, in certain situations where the crowd is very dense, the

\*salima.rafai@univ-grenoble-alpes.fr

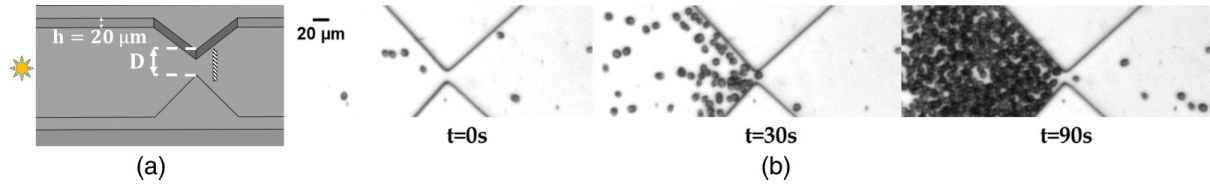


FIG. 1. (a) Schematic of bottleneck-shaped microchannel of thickness  $20\text{-}\mu\text{m} \sim 2 \times$  diameter of CR. The dashed rectangle represents the zone over which time lapses are measured. A light source is placed on the left, triggering a left to right swimming motion. (b) Snapshots of the jamming process through a  $D = 10\text{-}\mu\text{m}$  constriction at different times.

willingness of individuals is to increase their speed when making an effort to evacuate, which has the effect of blocking the entire evacuation process. In addition, it has been established that these paradoxical effects observed in crowd dynamics persist in a very wide variety of systems: In a granular silo [17], in a suspension [18] as well as in a flock of sheep or in a crowd of pedestrians [19]. A physicist's approach is us to look for a common physical mechanism behind these observable measured values. At a minimum, it would be desirable to succeed in defining universality classes in this family of problems. In particular, a class of systems could be that of active suspensions. In this Letter, we introduce active suspensions as a class of crowds and focus our study on jamming events occurring at a constriction due to cell buildup of microalgae. Understanding behavior of highly concentrated motile micro-organisms and especially their short-range interactions through adhesion or friction remains a challenge. In our experiments, we use a negative phototactic strain of green algae *Chlamydomonas reinhardtii* (CR) swimming away from light and moving toward a constriction [Fig. 1(b)]. We identify jamming events and analyze the dynamics of evacuation. The greater the velocity of the algae, the greater the active jamming. This phenomenon is very similar to the FiS effect mentioned above.

*Experimental details.* CR is a biflagellate photosynthetic cell [20] with diameter  $a = 10 \mu\text{m}$ . Cells are grown under a 14-h/10-h light/dark cycle at  $22^\circ\text{C}$  in *tris*acetate phosphate medium and are harvested in the middle of the exponential growth phase. CR's front flagella beat in a breaststroke manner and propel the cell in the fluid. The swimming is characterized by a persistent random walk in absence of bias [21,22]. However, in the presence of a light stimulus (green wavelength, i.e., around  $510 \text{ nm}$ ), the strain used in this Letter (CC-124) tends to swim away from the light source and perform a ballistic motion [23], this is known as negative phototaxis. CR suspension is concentrated by centrifuging  $40 \text{ mL}$  at  $1000 \text{ rpm}$  for  $15 \text{ min}$  and removing the supernatant, the solution is then placed under a red light for  $2 \text{ h}$ . Velocity is controlled by increasing the medium's viscosity via Dextran addition [24,25]. Cells are finally introduced within a microfluidic device composed of two reservoir chambers of height  $20 \mu\text{m}$  (twice the cell diameter) linked by a bottleneck constriction of varying width  $D = 10, 20, 30, \text{ and } 50 \mu\text{m}$  [Fig. 1(a)]. Microfabrication is made of transparent polydimethylsiloxane by means of soft lithography processes [26], Bovine serum albumin is used to passivate the device and avoid cells' adhesion.

We observe the cells under a bright field inverted microscope (Olympus IX71, magnification  $\times 4$ ) coupled to a 14-bit CCD camera (Prosilica GX) used at a frame rate of  $20 \text{ fps}$ . The sample is enclosed in a black box with two red filtered windows for visualization in order to prevent the microscope light from triggering phototaxis.

The algae are initially distributed homogeneously in the chamber. A white LED light is switched on the left side of the sample. Negative phototaxis makes the microswimmers swim toward walls and at the constriction. Particle tracking is performed using the library TRACKPY [27,28]. The volume fraction of cells when very dense regimes are reached is deduced from gray level intensity measurements that were calibrated beforehand. Figure 1(b) illustrates one typical geometry of the experiments. The sequence shows a series of microscopy images at different timescales following the light stimulus. The microswimmers swim away from the light and toward the constriction (from

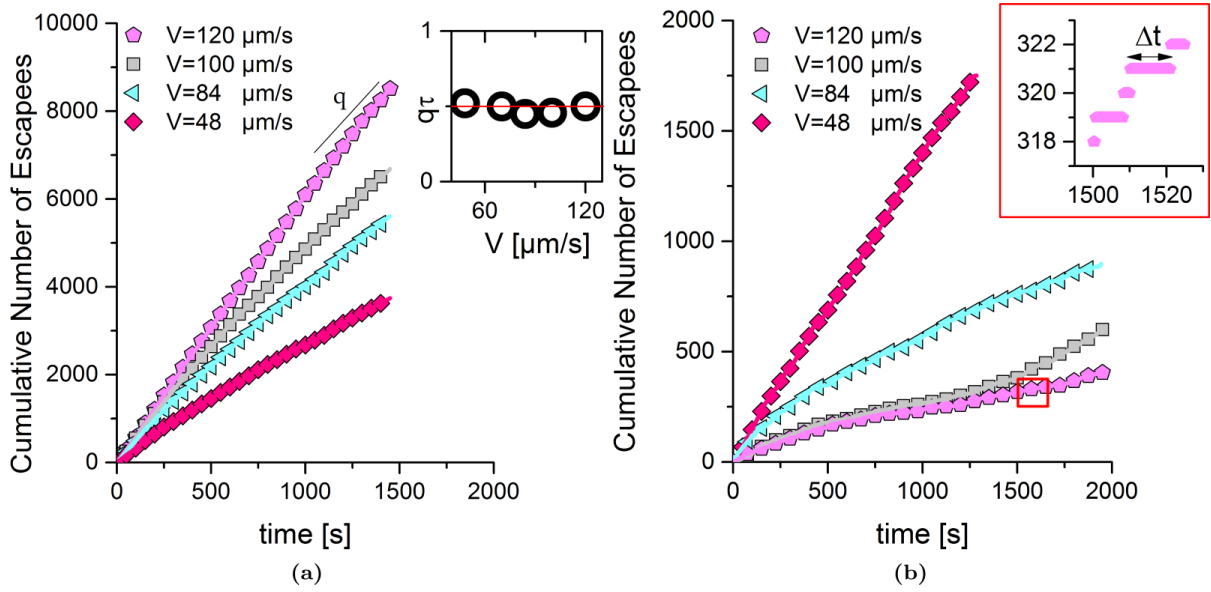


FIG. 2. Cumulative number of CR crossing the constriction as a function of time ( $t$ ) for different swimming velocities. (a) Large door size:  $D = 67 \mu\text{m}$  ( $\sim 7a$ ) the flux of particles increases when velocity is increased, the inset shows an equivalence between the flux  $q$  and the  $\tau = \frac{a}{V}$  (Stokes time). (b) Small door size  $D = 10 \mu\text{m}$  ( $\sim a$ ) the flux is now decreasing when velocity is increased. The inset: Zoom showing the existence of plateaus, i.e., longer waiting times  $\Delta t$ .

left to right). The sampling window is located on the right-hand side (downstream) at  $40 \mu\text{m}$  from the constriction with a width of  $1.375 \mu\text{m}$  (1 px) and a height chosen as 1.5 times the diameter  $D$  [Fig. 1(a)]. Analyses are performed after a stable buildup is formed at the door with a volume fraction  $\phi \approx 55\%$  to avoid any effect of density variation. Critical clogging (i.e., permanently clogged door) was never observed during our experiments. A stationary state characterized by a constant volume fraction at the constriction and cells exiting the constriction is observed along the whole duration of an experiment. However, experiments cannot be carried out on a duration exceeding 40 min as cells are observed to lose their sensitivity to light beyond this typical timescale.

*Results. Effect of swimming velocity.* This section focuses on the effect of swimming velocity on the evacuation process. With the velocity controlled and the data obtained as explained in the previous section, plotting the cumulative number of the escaping cells is straightforward. Our Letter focuses first on a wide door geometry with  $D = 67 \mu\text{m} \sim 7a$ . The cumulative number of cells escaping throughout the experiment plotted in Fig. 2(a) shows a linear trend where a more efficient evacuation occurs with higher swimming velocities. We define the flux  $q$  as the number of cells escaping per second. Graphically, it is the slope of linear fits. Figure 2(a) shows that the flux increases with increasing velocity, meaning the faster the cells swim the more they evacuate. Multiplying  $q$  by the Stokes time  $\tau = \frac{a}{V}$  (the time that a cell takes to travel a distance equal to its own diameter) gives a value that is independent of velocity, hence, the equivalence between  $\tau$  and  $q^{-1}$ . In the same method, when we analyze smaller door size  $D = a = 10 \mu\text{m}$ , results in Fig. 2(b) show a loss in linearity as  $V$  increases with the evacuation being more efficient for slower velocities and  $q$  increases with decreasing  $V$ .

In order to quantify jamming events, we study statistical distributions of time-lapses  $\Delta t$  [Fig. 3(b)] between two consecutive escaping CRs, known as the survival function,

$$P(t > \Delta t) = \int_{\Delta t}^{\infty} \rho(\Delta t') d\Delta t'.$$

where  $\rho(\Delta t')$  is the distribution function of time lapses. F3 It has been argued [19] that a survival function following a power-law decay with an exponent equal to  $1 - \alpha$  since  $\rho(\Delta t) \sim \Delta t^{-\alpha}$

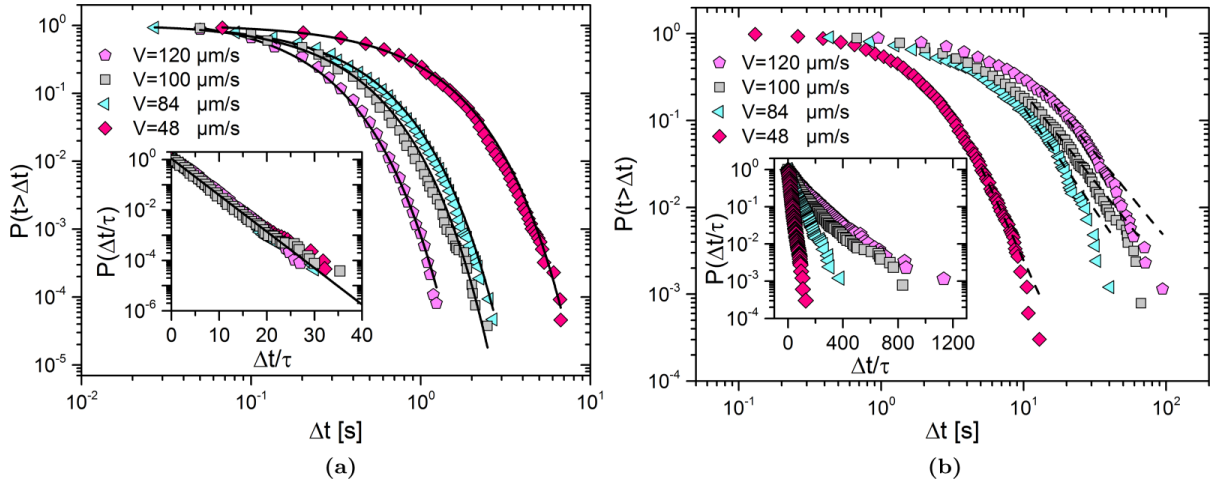


FIG. 3. Distribution of time lapses between two consecutive escaping CRs (survival function) for different swimming velocities. (a)  $D = 67 \mu\text{m}$ . Survival functions are well fitted by an exponential behavior (solid lines). The inset: log-lin representation shows a collapse when rescaling timescales by  $\tau$ . (b)  $D = 10 \mu\text{m}$  ( $\sim a$ ). Survival functions show a power-law behavior (dashed lines). The inset: log-lin representation shows a deviation from exponential behavior and no collapse when timescales are rescaled by  $\tau$ .

signifies that the system is susceptible to jam. On the other hand, an uninterrupted flow (i.e., flowing state) is represented by a survival function following an exponential decay (i.e., an average characteristic time lapse can then be defined).

Visually establishing a linear trend in a logarithmic-scaled histogram is not enough, therefore, the method described in Ref. [29], known as the Clauset-Shalizi-Newman method (CSN), and its corresponding open source code described in Ref. [30] are used to fit tails and extract values of  $\alpha$ , the minimum time lapse above which the trend becomes power law ( $\Delta t_{\min}$ ) and parameters determining the goodness of fit.

Figure 3(a) shows the survival function for different swimming velocities for  $D = 67 \mu\text{m}$ . For all velocities the dominating trend is that of an exponential decay  $P(t > \Delta t) \sim \exp(-\frac{\Delta t}{T})$  describing a continuous, uninterrupted evacuation,  $T$  being the exponential time. Normalizing time lapses with  $\tau$  in inset of Fig. 3(a), leads to a collapse of all velocities following an exponential decay (solid fit). Figure 3(b) shows the survival function for different swimming velocities for  $D = 10 \mu\text{m}$ . We note as the evacuation velocity increases, the probability to get longer time during which the flux is interrupted increases. In addition, when normalized by  $\tau$  in the inset of Fig. 3(b), two distinct regimes can be seen. The first, for  $\Delta t \leq \tau$ , follows an exponential decay, describing a system that is more prone to a flowing state. The second, for  $\Delta t > \tau$ , the power-law trend prevails with a deviation from the exponential trend with no collapse when time is rescaled by  $\tau$  and the system becomes more susceptible to jamming. Figure 4 shows that the coefficient  $\alpha$  decreases with increasing  $V$  for  $D < 50 \mu\text{m}$ , this behavior is found in many systems and is compatible to what might be described asFiS.

On the other hand, the opposite behavior is observed for  $D = 50 \mu\text{m}$ . Figure 4 shows an increasing value of  $\alpha$  with an increasing  $V$ , thereby the system is more prone to flow without jamming.

*Effect of door width.* In this section we are interested in the effect of door width on the evacuation process. The analysis is performed by fixing the swimming velocity whereas varying  $D$ . In the same procedure detailed in the previous section, we calculate the survival function and extract the coefficient  $\alpha$ . Figure 4 shows that at constant  $V$  with increasing  $D$ ,  $\alpha$  increases as well. It means that the evacuation process is less susceptible to jamming, it is also well defined with the previous case of  $D = 67 \mu\text{m}$ . This observation gives a clue to the presence of a transition zone for  $50 \mu\text{m} \leq D \leq 67 \mu\text{m}$ . We would like to investigate the possibility of empirically calculating the value of a critical

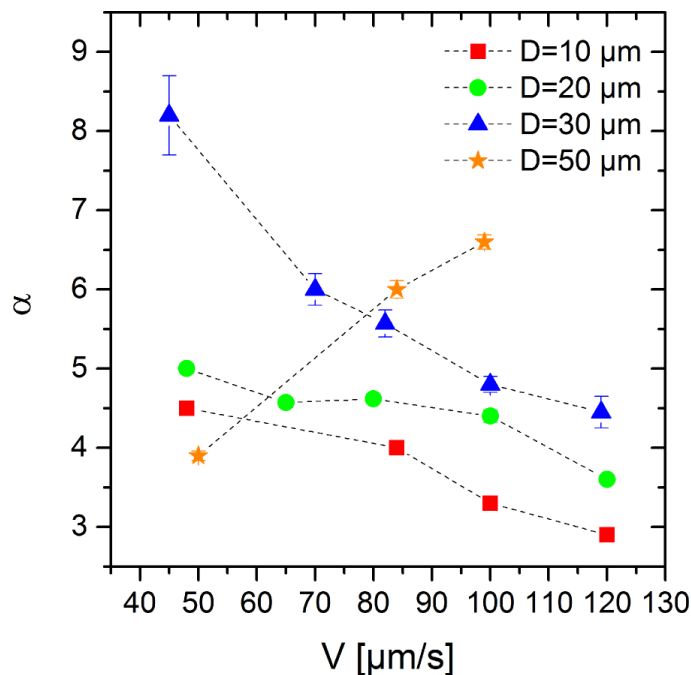


FIG. 4. Power-law exponent  $\alpha$  of survival functions as function of swimming velocities and different door sizes. For small values of  $D$  ( $<50 \mu\text{m}$ ),  $\alpha$  decreases with  $V$ , whereas for  $D = 50 \mu\text{m}$ ,  $\alpha$  is found to increase with  $V$ . Error bars, when not visible, are smaller than symbols.

diameter  $D_c$  for which we obtain a transition from jamming to flowing state for a given velocity. A similar attempt was recently made for vibrated granular media in Ref. [31] where transition is dependent on the vibrating intensity and door size and in tilted hoppers [32] where the effect of the tilt angle is reported. But first, we need to tackle the problem of finding a  $\Delta t$  above which the system is considered jammed, noted as  $\Delta t_c$ . Such attempts have been performed in systems of sheep [33] and horizontal hoppers [34]. In our case we define  $\Delta t_c = \Delta t_{\min}$  given by the CSN fitting method. For a door size  $D = 10 \mu\text{m}$  and  $V$  varying from 48 to 120  $\mu\text{m/s}$ ,  $\Delta t_c$  varies from 3.15 to 12 s. We define the avalanche size  $s$  as the number of CRs that pass through the door between two jamming events, consequently,  $\langle s \rangle$  is  $s$  averaged over the experiments for a waiting time  $\Delta t$ , we have a jamming if  $\Delta t \geq \Delta t_c$ . Having determined the way by which we obtain the avalanche size, we can now investigate the transition from flowing to jamming. Our results, the Supplemental Material [35], show that  $\langle s \rangle$  grows with  $D$ , and the behavior can be described empirically by a power-law divergence, where  $\langle s \rangle$  increases as  $D$  approaches its critical value  $D_c$  for which  $\langle s \rangle$  diverges:  $\langle s \rangle = \frac{C}{(D_c - D)^\beta}$  with  $D_c$ ,  $C$ , and  $\beta$  being fitting parameters. Interestingly, work performed with three-dimensional silo [17] and tilted hoppers with different types of grains [32] shows a similar trend.

Another physical quantity that characterizes the state of the system is the jamming probability. In Ref. [36], the authors proposed a probabilistic model describing the behavior of avalanche size  $s$  of grains for gravity driven hoppers where jamming is due to arching. Even though we do not observe any arch formation in our experiments, we extend the reasoning to our system. Let us quantify avalanche size  $s$  with  $\gamma(s)$  which is the probability of finding an avalanche of size  $s$ . By definition, an avalanche size consists of one jamming event and  $s$  nonjamming events. Therefore, we can write  $\gamma(s) = p^s(1 - p)$ . Here,  $p$  is the probability of a CR passing the door without cooperating with its neighbors to form a cluster and jam the door,  $J = 1 - p$  is, therefore, the probability of a CR ability to jam the exit. We assume that  $p$  is constant for all CR given the uncorrelated nature of jamming structures. Thus,  $p$  is a fitting parameter extracted from experimental data fitted with the above expression of  $\gamma(s)$ , Supplemental Material [35].  $p$  (and, subsequently,  $J$ ) is dependent on both the door size  $D$  and the swimming velocity  $V$ .

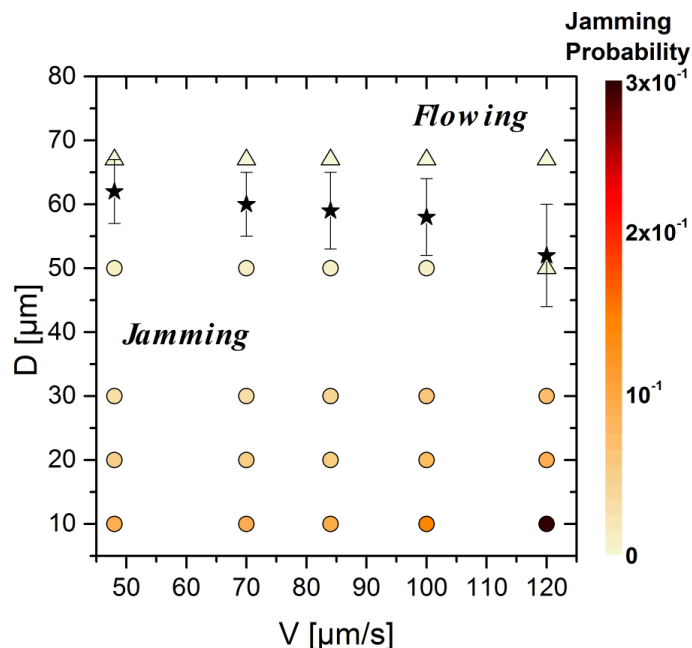


FIG. 5. Active jamming phase  $D - V$ . For  $D < D_c$ , a power-law behavior of the survival functions indicates jamming ( $\circ$ ). For  $D \geq D_c$ , a flowing regime is found ( $\triangle$ ) and well described by exponential survival function. Values of  $D_c$  ( $\star$ ) are given by  $\langle s \rangle = \frac{C}{(D_c - D)^\beta}$  with error bars being the fitting confidence intervals. Jamming probability follows the color scale.

The phase diagram in Fig. 5 shows that the predicted values of  $D_c$ , extracted from the power-law divergence, are in agreement with our experimental results and fall well in the transition zone. In addition, it pin points the location of phase transition from a dominant power-law tail regime for  $D < D_c$  where the system is prone to jam, to a domain dominated by an exponential decay for  $D \geq D_c$  where the evacuation happens without observable interruption. The color indexing according to  $J$  gives an insight to the behavior of our system. Fixing  $D$  and increasing  $V$  shows an increase in jamming probability, whereas  $J$  decreases when fixing  $V$  and increasing  $D$  until reaching  $D_c$  above which  $J = 0$ .

*Conclusion.* To conclude, we have developed an experimental approach to study the active jamming of microswimmers at a constriction. We studied the effect of changing the swimming velocity and the opening size and looked at the results through two different points of view, the first being time-lapse distribution, the other being the avalanche size. We have found that the evacuation process for a given velocity is disturbed for a range of  $D < D_c$ , whereas for values of  $D \geq D_c$  the system does not experience jamming. The approach used in studying granular systems describes well the effect of door size and swimming velocity on the jamming probability, suggesting underlying similarities in jamming issues between both granular and active suspensions. To gain further understanding of the mechanisms at hand in flowing to jamming transition in active suspensions, a thorough investigation of the cell-cell interactions, in particular, in the dense jammed suspensions would be fruitful.

*Acknowledgments.* We thank R. Mari and A. Nicolas for insightful discussions. We thank the CNRS 80Prime Program for financing this work. We thank the French-German University Program “Living Fluids” (Grant No. CFDA-Q1-14) (M.B., P.P., and S.R.)

- [1] E. Matsumura, A. Nakagawa, Y. Tomabechei, S. Ikushiro, T. Sakaki, T. Katayama, K. Yamamoto, H. Kumagai, F. Sato, and H. Minami, Microbial production of novel sulphated alkaloids for drug discovery, *Sci. Rep.* **8**, 7980 (2018).

- [2] J. J. Milledge and S. Heaven, A review of the harvesting of micro-algae for biofuel production, *Rev. Environ. Sci. Bio/Technol.* **12**, 165 (2013).
- [3] A. Nakagawa, E. Matsumura, T. Koyanagi, T. Katayama, N. Kawano, K. Yoshimatsu, K. Yamamoto, H. Kumagai, F. Sato, and H. Minami, Total biosynthesis of opiates by stepwise fermentation using engineered escherichia coli, *Nat. Commun.* **7**, 10390 (2016).
- [4] W. C. DeLoache, Z. N. Russ, L. Narcross, A. M. Gonzales, V. J. Martin, and J. E. Dueber, An enzyme-coupled biosensor enables (s)-reticuline production in yeast from glucose, *Nat. Chem. Biol.* **11**, 465 (2015).
- [5] B. K. Hønsvall, D. Altin, and L. J. Robertson, Continuous harvesting of microalgae by new microfluidic technology for particle separation, *Bioresour. Technol.* **200**, 360 (2016).
- [6] A. Karimi, D. Karig, A. Kumar, and A. Ardekani, Interplay of physical mechanisms and biofilm processes: Review of microfluidic methods, *Lab Chip* **15**, 23 (2015).
- [7] C. R. Cabrera and P. Yager, Continuous concentration of bacteria in a microfluidic flow cell using electrokinetic techniques, *Electrophoresis* **22**, 355 (2001).
- [8] E. Dressaire and A. Sauret, Clogging of microfluidic systems, *Soft Matter* **13**, 37 (2017).
- [9] M. Hassanpourfard, R. Ghosh, T. Thundat, and A. Kumar, Dynamics of bacterial streamers induced clogging in microfluidic devices, *Lab Chip* **16**, 4091 (2016).
- [10] H. M. Wyss, D. L. Blair, J. F. Morris, H. A. Stone, and D. A. Weitz, Mechanism for clogging of microchannels, *Phys. Rev. E* **74**, 061402 (2006).
- [11] R. Mukhopadhyay, When microfluidic devices go bad, *Anal. Chem.* **77**, 429 A (2005).
- [12] I. Griffiths, A. Kumar, and P. Stewart, A combined network model for membrane fouling, *J. Colloid Interface Sci.* **432**, 10 (2014).
- [13] A. Marty, C. Roques, C. Causserand, and P. Bacchin, Formation of bacterial streamers during filtration in microfluidic systems, *Biofouling* **28**, 551 (2012).
- [14] A. Wolff, I. R. Perch-Nielsen, U. Larsen, P. Friis, G. Goranovic, C. R. Poulsen, J. P. Kutter, and P. Telleman, Integrating advanced functionality in a microfabricated high-throughput fluorescent-activated cell sorter, *Lab Chip* **3**, 22 (2003).
- [15] A. Lim and R. Bai, Membrane fouling and cleaning in microfiltration of activated sludge wastewater, *J. Membr. Sci.* **216**, 279 (2003).
- [16] D. Helbing, I. Farkas, and T. Vicsek, Simulating dynamical features of escape panic, *Nature (London)* **407**, 487 (2000).
- [17] I. Zuriguel, A. Garcimartín, D. Maza, L. A. Pugnaloni, and J. M. Pastor, Jamming during the discharge of granular matter from a silo, *Phys. Rev. E* **71**, 051303 (2005).
- [18] M. Souzy, I. Zuriguel, and A. Marin, Transition from clogging to continuous flow in constricted particle suspensions, *Phys. Rev. E* **101**, 060901(R) (2020).
- [19] I. Zuriguel, D. R. Parisi, R. C. Hidalgo, C. Lozano, A. Janda, P. A. Gago, J. P. Peralta, L. M. Ferrer, L. A. Pugnaloni, E. Clément *et al.*, Clogging transition of many-particle systems flowing through bottlenecks, *Sci. Rep.* **4**, 7324 (2014).
- [20] E. H. Harris, *The Chlamydomonas Sourcebook: Introduction to Chlamydomonas and Its Laboratory Use* (Academic Press, Oxford, 2009), Vol. 1.
- [21] M. Polin, I. Tuval, K. Drescher, J. P. Gollub, and R. E. Goldstein, Chlamydomonas swims with two “gears” in a eukaryotic version of run-and-tumble locomotion, *Science* **325**, 487 (2009).
- [22] M. Garcia, S. Berti, P. Peyla, and S. Rafai, Random walk of a swimmer in a low-reynolds-number medium, *Phys. Rev. E* **83**, 035301(R) (2011).
- [23] X. Garcia, S. Rafai, and P. Peyla, Light Control of the Flow of Phototactic Microswimmer Suspensions, *Phys. Rev. Lett.* **110**, 138106 (2013).
- [24] S. Rafai, L. Jibuti, and P. Peyla, Effective Viscosity of Microswimmer Suspensions, *Phys. Rev. Lett.* **104**, 098102 (2010).
- [25] The effect of dextran addition on the cell-cell properties of adhesion and lubrication have, however, not yet been explored.
- [26] D. Qin, Y. Xia, and G. M. Whitesides, Soft lithography for micro-and nanoscale patterning, *Nat. Protoc.* **5**, 491 (2010).



- [27] D. B. Allan, T. Caswell, N. C. Keim, and C. M. van der Wel, trackpy Trackpy v0.4.1 (Zenodo, 2018), <https://doi.org/10.5281/zenodo.1226458>.
- [28] J. C. Crocker and D. G. Grier, Methods of digital video microscopy for colloidal studies, *J. Colloid Interface Sci.* **179**, 298 (1996).
- [29] A. Clauset, C. R. Shalizi, and M. E. J. Newman, Power-law distributions in empirical data, *SIAM Rev.* **51**, 661 (2009).
- [30] J. Alstott, E. Bullmore, and D. Plenz, powerlaw: A python package for analysis of heavy-tailed distributions, *PLoS ONE* **9**, e85777 (2014).
- [31] R. Caitano, B. V. Guerrero, R. E. R. González, I. Zuriguel, and A. Garcimartín, Characterization of the Clogging Transition in Vibrated Granular Media, *Phys. Rev. Lett.* **127**, 148002 (2021).
- [32] C. C. Thomas and D. J. Durian, Geometry dependence of the clogging transition in tilted hoppers, *Phys. Rev. E* **87**, 052201 (2013).
- [33] A. Garcimartín, J. M. Pastor, L. M. Ferrer, J. J. Ramos, C. Martín-Gómez, and I. Zuriguel, Flow and clogging of a sheep herd passing through a bottleneck, *Phys. Rev. E* **91**, 022808 (2015).
- [34] Q.-C. Yu, N. Zheng, and Q.-F. Shi, Clogging of granular materials in a horizontal hopper: Effect of outlet size, hopper angle, and driving velocity, *Phys. Rev. E* **103**, 052902 (2021).
- [35] See Supplemental Material at <http://link.aps.org/supplemental/10.1103/PhysRevFluids.7.L092301> show that  $\langle s \rangle$  grows with  $D$ , and the behavior can be described empirically by a power-law divergence.
- [36] A. Janda, I. Zuriguel, A. Garcimartín, L. Pugnali, and D. Maza, Jamming and critical outlet size in the discharge of a two-dimensional silo, *Europhys. Lett.* **84**, 44002 (2008).

# Active jamming of microswimmers at a bottleneck constriction

Edouardo Al Alam, Marvin Brun-Cosme-Bruny, Vincent Borne, Philippe Peyla,\* and Salima Rafai†  
Univ. Grenoble Alpes, CNRS, LIPhy, F-38000 Grenoble, France

Sylvain Faure

Laboratoire de Mathématiques d'Orsay, Université Paris-Saclay, 91405 Orsay Cedex, France

Bertrand Maury

Département de Mathématiques Appliquées, Ecole Normale Supérieure, Université PSL, Paris, France and  
Laboratoire de Mathématiques d'Orsay, Université Paris-Saclay, 91405 Orsay Cedex, France

(Dated: September 16, 2022)

## Velocity

The geometry of the channel confines the motion in the plane, however, when exposed to light stimulus, the *Chlamydomonas Reinhardtii* adopt a ballistic behavior to swim away from the source, making their motion dominant following the  $x$ -axis. Velocity is calculated over a step of  $\frac{1}{20}$  seconds on the right hand side far from the constriction and in a diluted regime to avoid noise from cell-cell interactions. The velocity distribution is fitted with a Gaussian trend from which we extract the value and the corresponding error margin as shown in Fig. 1a.

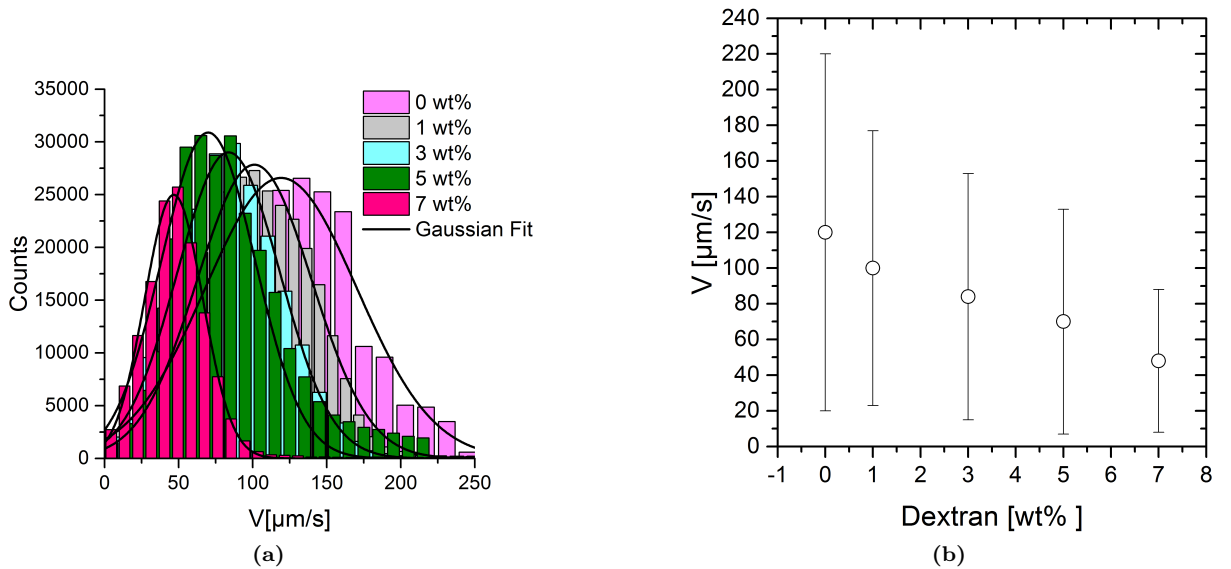


**FIG. 1:** a) Histogram of velocity distributions with different Dextran concentration. Solid lines correspond to the Gaussian fit. b) Effect of Dextran's weight percentage on the swimming velocity, error bars corresponds to fluctuations inside a given suspension as well as between different cultures.

Controlling the velocity is done via increasing medium's viscosity by adding adequate percentages of Dextran 9000-11000 Mwt. It has been shown that the higher the medium's viscosity the slower is the swimming velocity. In Fig.1b we plot the experimental swimming velocities that we obtain for each Dextran percentage.

### Density calibration and measurements

Crowd formation is identified by a phenomenon of clustering causing an increase in the local density, in those regimes particles become so closely packed that it becomes quasi-impossible to count them, therefore the traditional technique used in diluted regimes to calculate  $\phi$  based on counting, fails. To solve this issue we opt to measure the grey level and link it to the absorbance. Following Beer-Lambert law, it exists a relationship between the volume fraction  $\phi$  (or density) and the absorbance  $A$  via the equation:

$$\epsilon\phi l A = -\log \frac{\langle I \rangle}{\langle I_0 \rangle} \quad (1)$$

where  $\langle I \rangle$  is the intensity averaged over all the pixels in the image,  $\langle I_0 \rangle$  the average intensity of the background where no particle are present,  $l$  the length of the optic trajectory and  $\epsilon$  is the molar attenuation coefficient. It is important to us to investigate the validity of the Beer-Lambert at high concentration and see if the linearity between  $\phi$  and  $A$  still stands for those regimes.

To do so, we opt first for measuring volume fractions in diluted regimes by simple counting of particles, where the number  $N$  is related to  $\phi$  via:  $\phi = N \times \frac{V_{cell}}{V_T}$ , where  $V_{cell}$  is the volume of one CR, and  $V_T$  is the volume of the geometry with a depth of 20  $\mu\text{m}$ . Due to their spherical shape, we consider the volume of CR to be that of sphere. Cells are neutralized by adding alcohol to the medium, then injected in wells of volume 0.4 mL (type *Thermo Scientific*), where they sediment, counting in diluted regimes is done using the *trackpy* routine. On the other hand, measurements of absorbance are done by observing each well and using a *python* routine to calculate  $I$  for each pixel and average it over the whole image.

Indeed, with jamming formation we expect to have much larger concentrations as our cells aggregate in front of the opening. Hence, we have to extend the calibration to high density regimes. Immediately we are confronted to an issue, the *trackpy* routine loses its ability of detection at high  $\phi$ . To counter this obstacle, we resort to a technique know as *Log Dilution*. Using a centrifuge we obtain a concentration 50 $\times$  higher than the initial one. Letting the cell sediment, we remove the excess liquid leaving a highly concentrated cells' suspension. By diluting 10 $\times$  we can easily count and calculate the volume fraction  $\phi_{dilute}$ . If one supposes that the number of cells present in a solution diluted 10 $\times$  ( $N_{diluted}$ ) and in the initial one  $N_{concentrated}$  are proportional to one another, one can write  $N_{concentrated} = 10 \times N_{diluted}$  and consequently  $\phi_{concentrated} = 10 \times \phi_{diluted}$ . Figure 2a represents the calibration to obtain the relationship between volume fraction and absorbance extended to high density regimes. We use a forth degree polynomial to characterize the relationship:  $\phi = aA^4 + bA^3 + cA^2 + dA + e$ .

We can identify when the crowd is formed and stable (Fig.2b) to avoid any effect of density fluctuation.

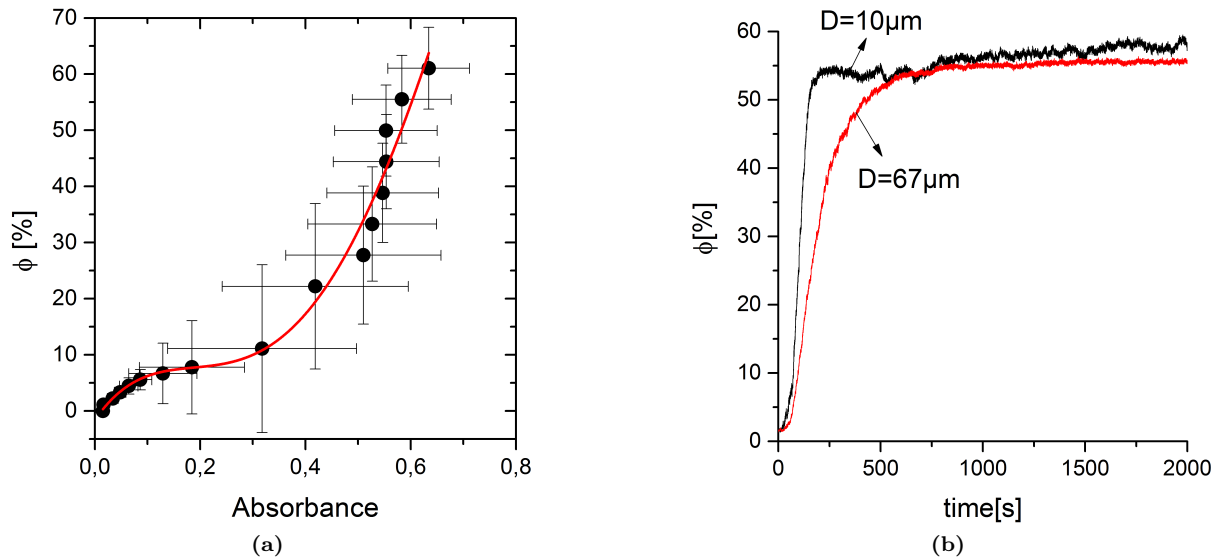


**FIG. 2:** a) Calibration extended to the high concentration regimes, where the relationship can be characterized by a fourth polynomial  $\phi = aA^4 + bA^3 + cA^2 + dA + e$ . b) Evolution of volume fraction at the door.

### Extracting $\Delta t$

$\Delta t$  is the time that separates two consecutive evacuations, also known as time-lapse. We extract it by focusing on the downstream part of our channel, i.e. after the constriction. Using the library *trackpy*, we get the position  $(x,y)$  of the center of each particle at a given time  $t$ . We choose a sampling window that is narrow (width of  $1.375 \mu\text{m}$ ) so only one cell can be captured, and strategically located so we avoid counting cells that rebound from the walls. We register the  $\Delta t$  between each cell passing consecutively in this zone. We also filter out any recurring cell number to avoid redundancy. Intrinsically, counting the number of cells allow us to plot the cumulative number of escapees.

### Fitting the survival function & Defining $\Delta t_c$

An important aspect of this work is the ability to know with certainty whether the survival function follows an exponential trend or a power law tail. To do so objectively we use the *powerlaw* library embedded in *python*. The algorithm [1] is developed based on the Clauset, Shalizi and Newman (CSN) method [2]. In their approach, CSN implemented the maximum likely-hood estimation (MLE) they use the Kolmogorov-Smirnov statistics to measure the distance between a power law tail, an exponential and the data. Two parameters are used to judge if the hypothesis of a powerlaw is accepted, the first being the  $p$ -value generated by a goodness of fit test and the other is the logarithmic ratio  $R$  of the two likelihood, that of a powerlaw and an exponential. A scenario where the powerlaw hypothesis is accepted consists of having a value of  $p > 0.1$  and  $R > 0$ . CSN also gives the value of the parameter  $\alpha$  and  $\Delta t_c$ , see Fig.4. For  $D = 10 \mu\text{m}$ , we notice in Fig.3a that visually the exponential and the power law tail are difficult to discriminate. However, Fig.3b shows the difference between the exponential fit (solid lines) and the power law (dashed lines). The exponential fit is found to deviated from the data earlier than the power law fit. In addition, when rescaling the time-lapses with the Stokes time  $\tau$  in the inset, the fact that no collapse is observed pleads in favor the power law trend (a process with no characteristic time). Using the CSN method, for  $V = 48 \mu\text{m}$ , the values of the coefficients ( $R$  and  $p$ ) favor a power law fitting ( $R = 1.902$  and  $p = 0.65$ ).

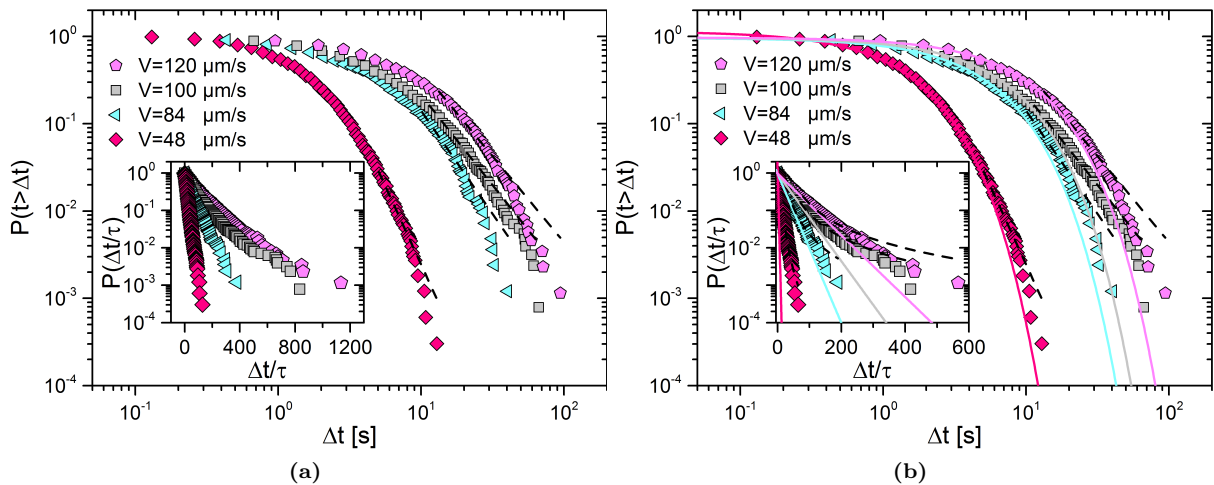


**FIG. 3:**  $D = 10 \mu\text{m}$  a. Logarithmic plot of the CCDF of time-lapses  $\Delta t$ . Dashed lines represent the power-law fit done using the CSN method. Inset: Log-lin plot of the CCDF of the re-scaled time-lapses, no collapse occurs. This plot is present in the main letter. b. Solid lines represent the exponential fit, we notice a divergence at the tail where the power law begins.

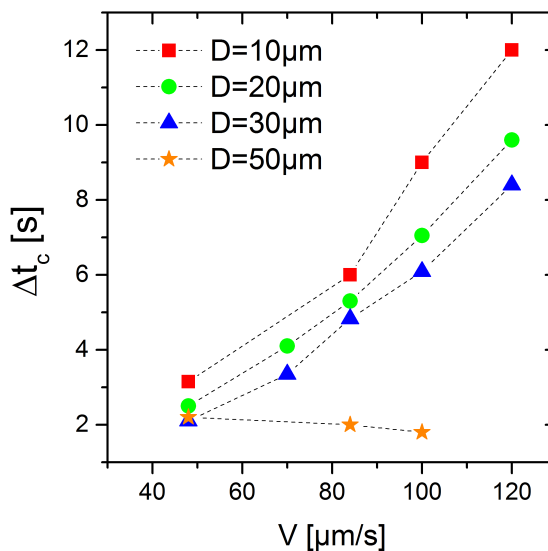


**FIG. 4:** Evolution of  $\Delta t_c$  with  $V$  and  $D$ . We can notice that the smaller the value of  $D$  the bigger the value of  $\Delta t_c$ .

#### Avalanche size

Avalanche size is the number of particles that escapes between two clogging events. Using the CSN method, we are able to extract  $\Delta t_c$  with a high degree of certainty. FIG.5a shows a typical avalanche size distribution for  $D = 10 \mu\text{m}$  and  $V = 48 \mu\text{m/s}$ , the expression  $\gamma(s) = p^s(1 - p)$  fits well, with  $p = 0.09295 \pm 0.0911$  being a fit parameter. Fig5b shows the relationship between  $\langle s \rangle$  and  $D$  described by a powerlaw divergence.

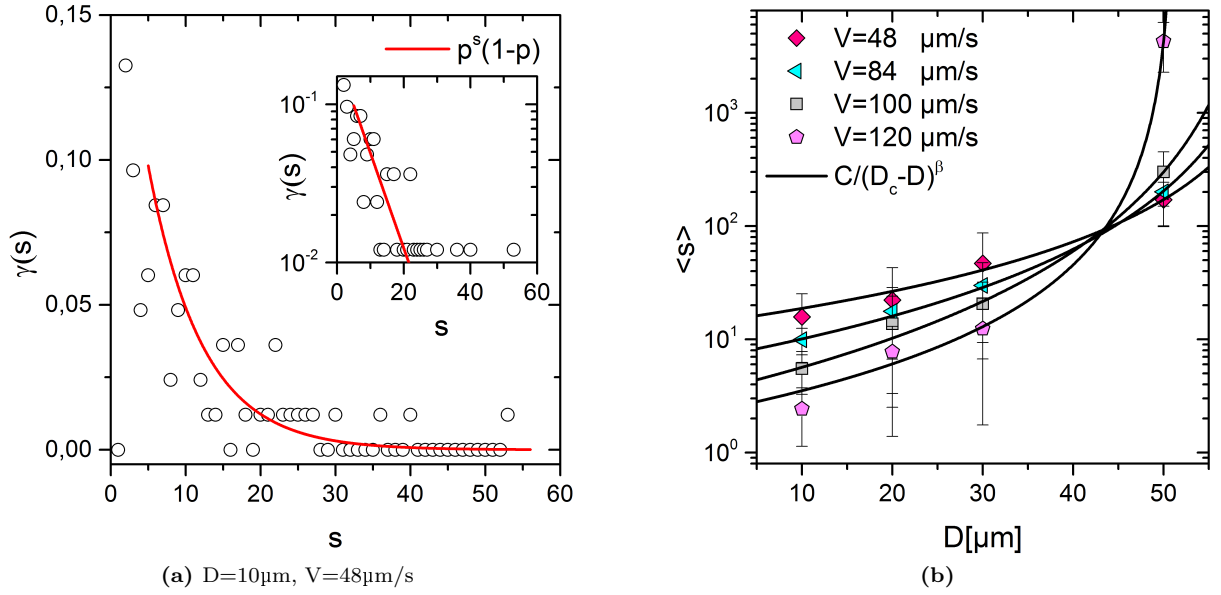


**FIG. 5:** a) Histogram of the number of cells  $s$  in an avalanche. Data corresponds to  $D = 10 \mu\text{m}$ , the solid represents the model proposed to describe the exponential decay of  $\gamma(s)$ . b) Experimental results of the mean avalanche size vs  $D_c - D$ . Solid lines are fits with the power law divergence showing the goodness of fit.

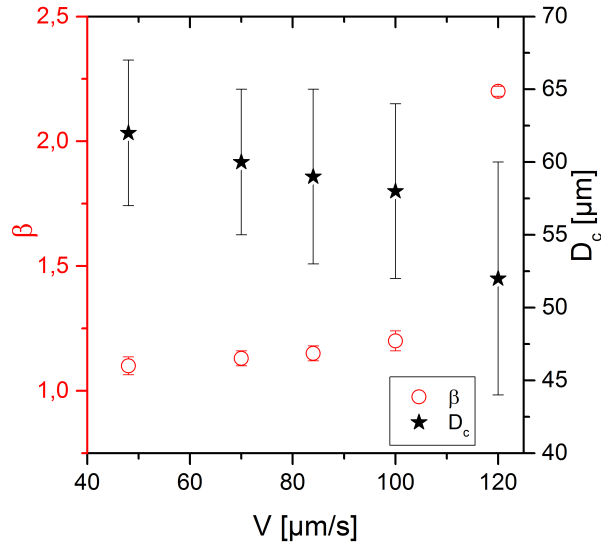


**FIG. 6:** Values of the fitting parameters  $\beta$  (o) and  $D_c$  (\*).  $D_c$  values are used in building the  $D - V$  diagram.

\* philippe.peyla@univ-grenoble-alpes.fr

† salima.rafaei@univ-grenoble-alpes.fr

[1] J. Alstott, E. Bullmore, and D. Plenz, powerlaw: A python package for analysis of heavy-tailed distributions, PLoS ONE **9**, e85777 (2014).

[2] A. Clauset, C. R. Shalizi, and M. E. J. Newman, Power-law distributions in empirical data, SIAM Review **51**, 661–703 (2009)



## Bibliography

- Allan, D. B., Caswell, T., Keim, N. C., van der Wel, C. M., and Verweij, R. W. (2021). soft-matter/trackpy: Trackpy v0.5.0.
- Alstott, J., Bullmore, E., and Plenz, D. (2014). powerlaw: A python package for analysis of heavy-tailed distributions. *PLoS ONE*, 9(1):e85777.
- Batyrova & Hallenbeck (2017). Hydrogen production by a chlamydomonas reinhardtii strain with inducible expression of photosystem ii. *International journal of molecular sciences*, 18(3):647.
- Berg, H. C. (2003). The rotary motor of bacterial flagella. *Annual review of biochemistry*, 72(1):19–54.
- Berg, H. C. (2004). *E. coli in motion*. Springer.
- Bielinski, C., Aouane, O., Harting, J., and Kaoui, B. (2021). Squeezing multiple soft particles into a constriction: Transition to clogging. *Phys. Rev. E*, 104:065101.
- Bonnemain, T., Butano, M., Bonnet, T., Echeverría-Huarte, I., Seguin, A., Nicolas, A., Appert-Rolland, C., and Ullmo, D. (2022). Pedestrians in static crowds are not grains, but game players. working paper or preprint.
- Brun-Cosme-Bruny, M. (2019). *Nage de suspensions actives en milieu complexe*. Theses, Université Grenoble Alpes.
- Caitano, R., Guerrero, B. V., González, R. E. R., Zuriguel, I., and Garcimartín, A. (2021). Characterization of the clogging transition in vibrated granular media. *Phys. Rev. Lett.*, 127:148002.
- Chardac, A. (2021). *Matière active polaire : ordre, désordre et défauts topologiques*. Theses, Université de Lyon.
- Chaté, H., Ginelli, F., Grégoire, G., Peruani, F., and Raynaud, F. (2008). Modeling collective motion: variations on the vicsek model. *The European Physical Journal B*, 64(3-4):451–456.



## BIBLIOGRAPHY

---

- Clauset, A., Shalizi, C. R., and Newman, M. E. J. (2009). Power-law distributions in empirical data. *SIAM Review*, 51(4):661–703.
- Cohen, I., Mason, T. G., and Weitz, D. A. (2004). Shear-induced configurations of confined colloidal suspensions. *Physical review letters*, 93(4):046001.
- Crocker & Grier (1996). Methods of digital video microscopy for colloidal studies. *Journal of colloid and interface science*, 179(1):298–310.
- Dickie, J. (1995). Major crowd catastrophes. *Safety science*, 18(4):309–320.
- Einstein, A. et al. (1905). On the motion of small particles suspended in liquids at rest required by the molecular-kinetic theory of heat. *Annalen der physik*, 17:549–560.
- Eshuis, P., van der Weele, K., van der Meer, D., Bos, R., and Lohse, D. (2007). Phase diagram of vertically shaken granular matter. *Physics of Fluids*, 19(12):123301.
- Faure & Maury (2015). Crowd motion from the granular standpoint. *Mathematical Models and Methods in Applied Sciences*, 25(03):463–493.
- Garcimartín, A., Pastor, J., Martín-Gómez, C., Parisi, D., and Zuriguel, I. (2017). Pedestrian collective motion in competitive room evacuation. *Scientific reports*, 7(1):10792.
- Garcimartín, A., Pastor, J. M., Ferrer, L. M., Ramos, J. J., Martín-Gómez, C., and Zuriguel, I. (2015). Flow and clogging of a sheep herd passing through a bottleneck. *Phys. Rev. E*, 91:022808.
- Grégoire & Chaté (2004). Onset of collective and cohesive motion. *Physical review letters*, 92(2):025702.
- Guariguata, A., Pascall, M. A., Gilmer, M. W., Sum, A. K., Sloan, E. D., Koh, C. A., and Wu, D. T. (2012). Jamming of particles in a two-dimensional fluid-driven flow. *Phys. Rev. E*, 86:061311.
- Hafez, A., Liu, Q., Finkbeiner, T., Alouhali, R. A., Moellendick, T. E., and Santamarina, J. C. (2021). The effect of particle shape on discharge and clogging. *Scientific Reports*, 11(1):3309.
- Harris, E. H., Stern, D. B., and Witman, G. B. (2009). *The chlamydomonas sourcebook*, volume 1. Elsevier San Diego, CA.
- Helbing, D. (2010). Pluralistic modeling of complex systems.
- Helbing & Molnar (1995). Social force model for pedestrian dynamics. *Physical review E*, 51(5):4282.
- Heliövaara, S., Ehtamo, H., Helbing, D., and Korhonen, T. (2013). Patient and impatient pedestrians in a spatial game for egress congestion. *Physical review. E, Statistical, nonlinear, and soft matter physics*, 87:012802.

- Henderson, L. F. (1974). On the fluid mechanics of human crowd motion. *Transportation research*, 8(6):509–515.
- Howse, J. R., Jones, R. A., Ryan, A. J., Gough, T., Vafabakhsh, R., and Golestanian, R. (2007). Self-motile colloidal particles: from directed propulsion to random walk. *Physical review letters*, 99(4):048102.
- Ide, T., Mochiji, S., Ueki, N., Yamaguchi, K., and Shigenobu, S. (2016). Identification of the *agg1* mutation responsible for negative phototaxis in a “ wild-type ” strain of *Chlamydomonas reinhardtii*. *Biochemistry and Biophysics Reports*, 7:379–385.
- Janda, A., Zuriguel, I., Garcimartín, A., Pugnali, L., and Maza, D. (2008). Jamming and critical outlet size in the discharge of a two-dimensional silo. *EPL (Europhysics Letters)*, 84:44002.
- Kantsler, V., Dunkel, J., Polin, M., and Goldstein, R. E. (2013). Ciliary contact interactions dominate surface scattering of swimming eukaryotes. *Proceedings of the National Academy of Sciences*, 110(4):1187–1192.
- Lim, J., Maes, F., Taly, V., and Baret, J.-C. (2014). The microfluidic puzzle: chip-oriented rapid prototyping. *Lab on a chip*, 14(10):1669–1672.
- Lin, P., Ma, J., and Lo, S. (2016). Discrete element crowd model for pedestrian evacuation through an exit. *Chinese Physics B*, 25(3):034501.
- López-Rodríguez, D., Gella, D., To, K., Maza, D., Garcimartín, A., and Zuriguel, I. (2019). Effect of hopper angle on granular clogging. *Phys. Rev. E*, 99:032901.
- Martin, M. (2017). *Etude des processus de concentration et de dispersion d’une suspension de micro-algues: effet des interactions hydrodynamiques sur la dynamique de la suspension*. PhD thesis, Grenoble Alpes.
- Martin, M., Barzyk, A., Bertin, E., Peyla, P., and Rafai, S. (2016). Photofocusing: Light and flow of phototactic microswimmer suspension. *Physical Review E*, 93(5):051101.
- Midtvedt, B., Pineda, J., Skärberg, F., Olsén, E., Bachimanchi, H., Wesén, E., Esbjörner, E. K., Selander, E., Höök, F., Midtvedt, D., and Volpe, G. (2022). Single-shot self-supervised particle tracking.
- Nicolas, A., Bouzat, S., and Kuperman, M. N. (2017). Pedestrian flows through a narrow doorway: Effect of individual behaviours on the global flow and microscopic dynamics. *Transportation Research Part B: Methodological*, 99:30–43.
- Nicolas, A., Garcimartín, A., and Zuriguel, I. (2018). Trap model for clogging and unclogging in granular hopper flows. *Phys. Rev. Lett.*, 120:198002.
- Palacci, J., Cottin-Bizonne, C., Ybert, C., and Bocquet, L. (2010). Sedimentation and effective temperature of active colloidal suspensions. *Physical Review Letters*, 105(8):088304.

## BIBLIOGRAPHY

---

- Parisi, D. R., Sartorio, A. G., Colonnello, J. R., Garcimartín, A., Pugnali, L. A., and Zuriguel, I. (2021). Pedestrian dynamics at the running of the bulls evidence an inaccessible region in the fundamental diagram. *Proceedings of the National Academy of Sciences*, 118(50):e2107827118.
- Parisi, D. R., Soria, S. A., and Josens, R. (2015). Faster-is-slower effect in escaping ants revisited: Ants do not behave like humans. *Safety science*, 72:274–282.
- Pastor, J. M., Garcimartín, A., Gago, P. A., Peralta, J. P., Martín-Gómez, C., Ferrer, L. M., Maza, D., Parisi, D. R., Pugnali, L. A., and Zuriguel, I. (2015). Experimental proof of faster-is-slower in systems of frictional particles flowing through constrictions. *Phys. Rev. E*, 92:062817.
- Prost, J. and Bruinsma, R. (2007a). Shape fluctuations of active membranes. *EPL (Europhysics Letters)*, 33:321.
- Prost, J. and Bruinsma, R. (2007b). Shape fluctuations of active membranes. *EPL (Europhysics Letters)*, 33:321.
- Qin, D., Xia, Y., and Whitesides, G. M. (2010). Soft lithography for micro- and nanoscale patterning. *Nature Protocols*, 5(3):491–502.
- Rafai, S., Jibuti, L., and Peyla, P. (2010). Effective viscosity of microswimmer suspensions. *Physical Review Letters*, 104(9):098102.
- Ramaswamy, S. (2010). The mechanics and statistics of active matter. *Annu. Rev. Condens. Matter Phys.*, 1(1):323–345.
- Scranton, M. A., Ostrand, J. T., Fields, F. J., and Mayfield, S. P. (2015). Chlamydomonas as a model for biofuels and bio-products production. *The Plant Journal*, 82(3):523–531.
- Sheikh, S., Gratzer, W. B., Pinder, J. C., and Nash, G. B. (1997). Actin polymerisation regulates integrin-mediated adhesion as well as rigidity of neutrophils. *Biochemical and Biophysical Research Communications*, 238(3):910–915.
- Shivan Gurumurthy, S. (2022). Particle tracking using deep learning.
- Souzy, M., Zuriguel, I., and Marin, A. (2020). Transition from clogging to continuous flow in constricted particle suspensions. *Phys. Rev. E*, 101:060901.
- Sticco, I. M., Cornes, F. E., Frank, G. A., and Dorso, C. O. (2017). Beyond the faster-is-slower effect. *Phys. Rev. E*, 96:052303.
- Thomas, C. C. and Durian, D. J. (2013). Geometry dependence of the clogging transition in tilted hoppers. *Phys. Rev. E*, 87:052201.
- To, K., Lai, P.-Y., and Pak, H. K. (2001). Jamming of granular flow in a two-dimensional hopper. *Phys. Rev. Lett.*, 86:71–74.

- Tsygankov, A. A., Kosourov, S. N., Tolstygina, I. V., Ghirardi, M. L., and Seibert, M. (2006). Hydrogen production by sulfur-deprived *chlamydomonas reinhardtii* under photoautotrophic conditions. *International Journal of Hydrogen Energy*, 31(11):1574–1584.
- Turner, L., Ryu, W. S., and Berg, H. C. (2000). Real-time imaging of fluorescent flagellar filaments. *Journal of Bacteriology*, 182(10):2793–2801.
- Vicsek, T., Czirók, A., Ben-Jacob, E., Cohen, I., and Shochet, O. (1995). Novel type of phase transition in a system of self-driven particles. *Physical review letters*, 75(6):1226.
- Wassgren, C. R., Hunt, M. L., Freese, P. J., Palamara, J., and Brennen, C. E. (2002). Effects of vertical vibration on hopper flows of granular material. *Physics of Fluids*, 14(10):3439–3448.
- Witman, G. B. (1993). *Chlamydomonas* phototaxis. *Trends in cell biology*, 3(11):403–408.
- Yu, Q.-C., Zheng, N., and Shi, Q.-F. (2021). Clogging of granular materials in a horizontal hopper: Effect of outlet size, hopper angle, and driving velocity. *Phys. Rev. E*, 103:052902.
- Zuriguel, I., Garcimartín, A., Maza, D., Pagnaloni, L. A., and Pastor, J. M. (2005). Jamming during the discharge of granular matter from a silo. *Phys. Rev. E*, 71:051303.
- Zuriguel, I., Parisi, D. R., Hidalgo, R. C., Lozano, C., Janda, A., Gago, P. A., Peralta, J. P., Ferrer, L. M., Pagnaloni, L. A., Clément, E., Maza, D., Pagonabarraga, I., and Garcimartín, A. (2014). Clogging transition of many-particle systems flowing through bottlenecks. *Scientific Reports*, 4(1):7324.





## Crowd of Microswimmers

The modeling of crowd movements has become a very active field of research, and deep debates still animate the community on how to model certain behaviors such as panic movements. In this case, the 'faster-is-slower' effect plays a central role: it essentially indicates that, in certain situations in which the crowd is very dense, the will of the individuals is to increase their mobility in their effort to evacuate, which has the effect of blocking the entire evacuation process. A similar paradoxical effect is known as loss of capacity. The capacity of an exit door is defined as the maximum flow that can pass through it. This quantity is not a static value but depends on the regime. The phenomenon of loss of capacity corresponds to a significant decrease in the actual flow upstream. It has recently been established that the paradoxical effects observed in crowd dynamics persist in a very wide variety of systems: in a granular silo, in a suspension as well as for a flock of sheep, or in a crowd of pedestrians. A physicist's approach, therefore, invites us to look for a common physical mechanism behind these measured observables. At a minimum, it would be desirable to succeed in defining classes of universality in this family of problems. In particular, a class of system could be that of the active suspensions which intrinsically involves hydrodynamic interactions between the agents. How and if microhydrodynamics will affect crowd dynamics are the questions we will address in this manuscript. The thesis work is experimental. It analyzes and quantifies the behavior of microswimmers (microalgae) put in an evacuation situation taking advantage of their negative phototaxis. The geometry of microfluidic chips is designed so a dense and stable crowd occurs on the door. The experiments involve cell culture, microfabrication, light field microscopy, image analysis and particle tracking, and finally statistical data analysis.

## Foule de micronageurs

La modélisation des mouvements de foule est devenue un domaine de recherche très actif, et de profonds débats animent encore la communauté sur la manière de modéliser certains comportements tels que les mouvements de panique. Dans ce cas, l'effet "plus vite est plus lent" joue un rôle central : il indique essentiellement que, dans certaines situations où la foule est très dense, la volonté des individus est d'augmenter leur mobilité dans leur effort d'évacuation, ce qui a pour effet de bloquer l'ensemble du processus d'évacuation. Un effet paradoxal similaire est connu sous le nom de perte de capacité. La capacité d'une porte de sortie est définie comme le flux maximal qui peut la franchir. Cette quantité n'est pas une valeur statique mais dépend du régime. Le phénomène de perte de capacité correspond à une diminution significative du débit réel en amont. Il a été récemment établi que les effets paradoxaux observés dans la dynamique des foules persistent dans une très grande variété de systèmes : dans un silo granulaire, dans une suspension aussi bien que pour un troupeau de moutons, ou dans une foule de piétons. Une approche de physicien nous invite donc à rechercher un mécanisme physique commun derrière ces observables mesurés. Au minimum, il serait souhaitable de parvenir à définir des classes d'universalité dans cette famille de problèmes. En particulier, une classe de système pourrait être celle des suspensions actives qui implique intrinsèquement des interactions hydrodynamiques entre les agents. Comment et si la microhydrodynamique va affecter la dynamique des foules sont les questions que nous aborderons dans ce manuscrit. Le travail de thèse est expérimental. Il analyse et quantifie le comportement de micro-nageurs (microalgues) mis en situation d'évacuation en tirant parti de leur phototaxie négative. La géométrie des puces microfluidiques est conçue pour qu'une foule dense et stable se produise sur la porte. Les expériences impliquent la culture de cellules, la microfabrication, la microscopie à champ lumineux, l'analyse d'images et le suivi des particules, et enfin l'analyse statistique des données.

---

---